広島大学学位請求論文

Neutral pion measurement in p-Pb collisions at $\sqrt{s_{\mathrm{NN}}} = 5.02$ TeV

（核子対あたり重心系衝突エネルギー5.02TeVの
陽子+鉛原子核衝突における中性パイ中間子の測定）

2017年

広島大学大学院理学研究科
物理科学専攻

大久保 翼

目次

1. 主論文

Neutral pion measurement in p-Pb collisions at $\sqrt{s_{\mathrm{NN}}} = 5.02$ TeV
（核子対あたり重心系衝突エネルギー 5.02 TeV の陽子+鉛原子核衝突における中性パイ中間子の測定）
　大久保　翼

2. 公表論文

(1) Neutral meson production in pp, p-Pb and Pb-Pb collisions with ALICE at the LHC
　　Tsubasa Okubo on behalf of the ALICE collaboration
… Accepted for publication in Nuclear and Particle Physics Proceedings by Elsevier (in press, reviewed)

3. 参考論文

(1) Direct photon production in Pb-Pb collisions at $\sqrt{s_{\mathrm{NN}}} = 2.76$ TeV
　　J. Adam *et al.* ALICE Collaboration
… Physics Letters B 754 (2016) 235-248

(2) Multiplicity dependence of charged pion, kaon, and (anti)proton production at large transverse momentum in p-Pb collisions at $\sqrt{s_{\mathrm{NN}}} = 5.02$ TeV
　　J. Adam *et al.* ALICE Collaboration
… Physics Letters B 760 (2016) 720-735

主論文

Neutral pion measurement in p-Pb collisions at $\sqrt{s_{\mathrm{NN}}} = 5.02$ TeV

Tsubasa Okubo

Department of Physics Science,

Graduate School of Science

Hiroshima University

February 14, 2017

Abstract

Quarks and gluons which are thought to be a elementary particle are confined in the nucleon, and it is impossible to extract only quark from the nucleon. However they are freed from confined state with a condition of extreme high temperature and high density. There was the high temperature and dense condition immediately after the big bang of the birth of the universe, and quarks and gluons could move around freely. This state is called Quark-Gluon Plasma (QGP). A high-energy heavy-ion collisions experiment can create the QGP experimentally. Particles passing through the QGP lose energy by the strong force. In the results, produced particles are modified their own yields.

Strong suppression of high-p_{T} particles has been observed in heavy-ion collisions at LHC energies, which can be interpreted by invoking various processes involving transport properties of the QCD medium and initial-state effects. Proton-nucleus (p-A) collisions are intermediate between proton-proton (pp) and nucleus-nucleus (A-A) collisions in terms of system size and number of produced particles. Comparing particle production in pp, p-A, A-A reactions has frequently been used to separate initial-state effects of colliding nuclei from final-state effects in quark matter created by the collisions. The study of neutral meson production in proton-lead (p-Pb) collisions at $\sqrt{s_{\mathrm{NN}}}$ = 5.02 TeV is of importance to confirm that the strong suppression observed in central lead-lead (Pb-Pb) collisions is a final-state effect of the produced hot and dense medium.

This paper will presents π^0 and η meson production in p-Pb collisions at $\sqrt{s_{\mathrm{NN}}}$ = 5.02 TeV and nuclear modification factor (R_{pPb}) for π^0 from the LHC-ALICE experiment for the first time. The π^0 meson is measured in p_{T} range of $0.3 - 20$ GeV/c via completely methods, using the ALICE electromagnetic calorimeters, PHOS and EMCal, and by the central tracking system, identifying photons converted into e^+e^- pairs in the material of the inner barrel detectors, TPC and ITS, called photon conversion method (PCM) In addition, PCM via γ-Dalitz decay channel is denoted as PCM-Dalitz. The η meson is measured in p_{T} range of $0.7 - 20$ GeV/c via EMCal and PCM.

The π^0 and η meson final spectra are achieved via combination of individual analyses with weight according to their uncertainties. Both π^0 and η meson invariant yields are a nice agreement by the Tsallis fit and all measurements are consistent with each other within the uncertainties. EPOS3 event generator based on hydrodynamical calculation reproduces well in the almost entire p_{T} region for π^0 and intermediate-p_{T} region for η meson.

The η/π^0 ratio increases at $p_{\mathrm{T}} < 4$ GeV/c and arrives a plateau of 0.47 ± 0.02 at $p_{\mathrm{T}} > 4$ GeV/c. It is consistent with the ALICE pp and Pb-Pb measurements and the world results. The m_{T} scaling for the η/π^0 ratio is good description at $p_{\mathrm{T}} > 4$ GeV/c, but discrepancy is observed in low-p_{T} region. The EPOS3 generator is good reproduction for data in low-p_{T} region and is closer than the m_{T} scaling prediction. But it fails to reproduce data in high-p_{T} region.

The π^0 nuclear modification factor in p-Pb collisions (R_{pPb}) increases with p_{T} in low-p_{T} region and consists with unity at $p_{\mathrm{T}} > 2$ GeV/c. It is not observed particle yield suppression as observed in Pb-Pb collisions. In addition, the π^0 nuclear modification factor in p-Pb collisions at LHC energy and in d-Au collisions at RHIC energy have no obvious difference. Theoretical model via using EPS09s NLO calculations and CGC model calculation are able to describe R_{pPb}. These results provide direction that strong suppression of high-p_{T} π^0 observed in Pb-Pb collisions comes from final-state effects due to parton energy loss in the hot QCD medium rather than initial-state effects.

Contents

List of Figures

List of Tables

Chapter 1

Introduction

Quantum Chromodynamics (QCD) predicts a phase transition at heavy-ion collisions from hadronic matter to a deconfined state of quarks and gluons called Quark-Gluon Plasma (QGP) [1]. Hadrons with high transverse momentum (p_{T}) are produced from the fragmentation of hard scattered quarks or gluons in high-energy heavy-ion collisions. Quarks and gluons interact strongly with the QGP and lose energy in the process of pass through the medium. This phenomena called "jet quenching" depletes hadron production at high-p_{T}. The study of high-p_{T} hadron production is essential to investigate the properties of the QCD medium created in heavy-ion collisions.

Neutral mesons, π^0 and η meson, are produced from parton fragmentation in the QCD vacuum in proton-proton (pp) collisions. The neutral mesons measurement is important for test of perturbative QCD (pQCD) predictions and understanding particle production. On the other hand, the measurements in lead-lead (Pb-Pb) collisions are studied for interpretation of the hadron suppression and parton energy loss in the QGP. Strong suppression of high-p_{T} π^0 has been observed in central Pb-Pb collisions at $\sqrt{s_{\mathrm{NN}}} = 2.76$ TeV [2]. This suppression observed at LHC is stronger than at RHIC or at SPS [3–5]. However the suppression mechanism can be explained by various processes involving transport properties of final-state effects like the hot QCD medium and the initial-state effects because the heavy-ion collisions include both effects of initial-state and final-state. The pp collisions characterize production process in the absence of both initial and final-state effects, and proton-lead (p-Pb) collisions characterize the process in absence of only final-state medium effects. So studies in p-Pb collisions which are intermediate between pp collisions and heavy-ion collisions in terms of system size and number of produced particles, are important to disentangle the suppression comes from initial condition of colliding nuclei of final-state effects in Pb-Pb collisions [6].

1.1   Quark Gluon Plasma (QGP)

The big bang theory says the universe was created about 137 hundred million years ago by the big bang expanded rapidly (called inflation). It had been state of high temperature and energy density in early time on the creation of the universe after the inflation. Then, quark pair, gluon, photon and lepton were generated and the universe at present was formed in this manner. In this high temperature and energy density state, quark and gluon could move about freely and the state
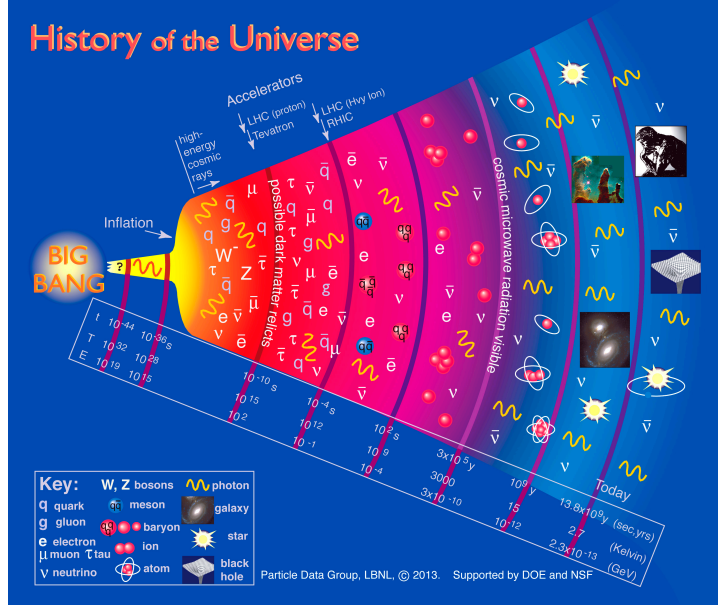
Figure 1.1: History of the universe [7]

is called Quark-Gluon Plasma (QGP). History of the universe is shown in Fig.1.1. It is important to study of the matter state on high temperature and energy density in early time on the creation of the universe in order to understand evolutional process of the universe.

It is considered quark and gluon are elementary particle, and it can't take out them independently according to the QCD. It is impossible to generate QGP in common temperature and energy density to the property of quark confinement. The way of break confinement is achieving high temperature and/or high energy density. Figure 1.2 presents the QCD phase diagram. The high-energy heavy-ion collisions experiment is only way to be able to generate QGP by artificial means.

The lattice QCD calculations predict that the phase transition to the QGP state occurs at a critical temperature, T_c, of about 200 MeV. Figure 1.3 shows the theoretical calculation of the entropy density s/T^3 as a function of temperature T [9]. The entropy density increase stepwise the deconfinement of the matter.

1.2 High-energy heavy-ion collisions

High-energy heavy-ion collisions are powerful and unique tool to study strongly interacting matter at a high temperature and densities which is predicted by QCD a phase transition from hadronic matter to a deconfined state of quarks and gluons called QGP.

The first heavy-ions acceleration at CERN which is derived from the acronym for the French "Conseil Européen pour la Recherche Nucléaire" or European Council for Nuclear Research, has been started with Super Proton Synchrotron (SPS) in 1986 to study possibility of QGP. The SPS accelerated protons and lead ions, and achieved collision energy in pp collisions at $\sqrt{s} = 450$
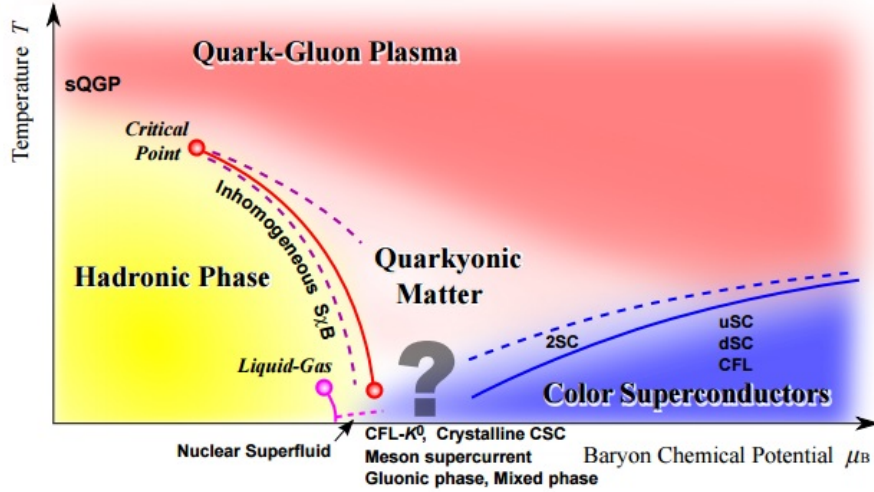
Figure 1.2: Conjectured QCD phase diagram with boundaries that define various states of QCD matter based on SχB patterns [8]
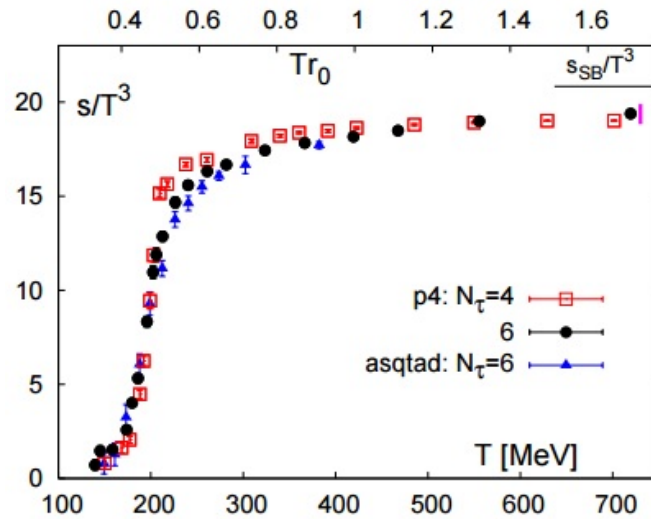
Figure 1.3: Entropy density s normalized by T^3 as a function of temperature on temporal extent $N_\tau = 4$ and 6 based on lattice QCD calculation [9]

GeV and in Pb-Pb collisions at $\sqrt{s_{\mathrm{NN}}} = 158$ GeV with fixed target experiment. J/ψ suppression measured in Pb-Pb collisions at SPS suggested production for deconfinement state of quarks and gluons. Relative Heavy Ion Collisions (RHIC) at Brookhaven National Laboratory (BNL) is the first colliding beam accelerator which accelerates protons, deuterons, copper ions and gold ions up to in pp collisions at $\sqrt{s} = 510$ GeV and in gold-gold (Au-Au) collisions at $\sqrt{s_{\mathrm{NN}}} = 200$ GeV. Many kinds of signatures such as suppression of high-p_{T} particle (jet-quenching) and azimuthal anisotropy (elliptic flow) at RHIC indicated evidence for QGP generation. However there remains many unknown puzzles. Large Hadron Collider (LHC) at CERN which has started operation from 2009, has energy region of TeV scale about 10 times higher energy than RHIC. The heavy-ion experiment at LHC enables us precise measurement and provides quantitative understanding to figure out the properties of QGP.

1.3 Time evolution of heavy-ion collisions

This section describes collisions geometry and time evolution for high-energy heavy-ion collisions (Fig.1.4). Before the collisions, the two nuclei accelerated to near the light speed are compressed into a pancake shape due to the Lorentz contraction. High-p_{T} particles and heavy quarks are produced in hard interaction by partons scattering at the instant of the collisions. After the collisions, the nuclei with extremely high energy sneak through each other. The space after sneaking through reaches a high temperature and energy density. In this state, quarks and gluons are freed from confinement of nucleon and can move freely named QGP which is formed immediately after the collisions ($\tau \sim 1$ fm/c). Subsequently the hot and dense medium starts to expand and cools down with expansion. The medium is converted to hadronic state by formation of a large amount of hadrons, when the temperature becomes lower than the phase transition value. The hadronization happens at ~ 10 fm/c. These hadrons undergo inelastic and elastic collisions during the hadronic evolution. When the inelastic collisions cease, the hadron abundances are fixed (chemical freeze-out). When the elastic collisions cease, the momentum distributions of the various hadrons is determined defined as thermal freeze-out (or kinematic freeze-out).
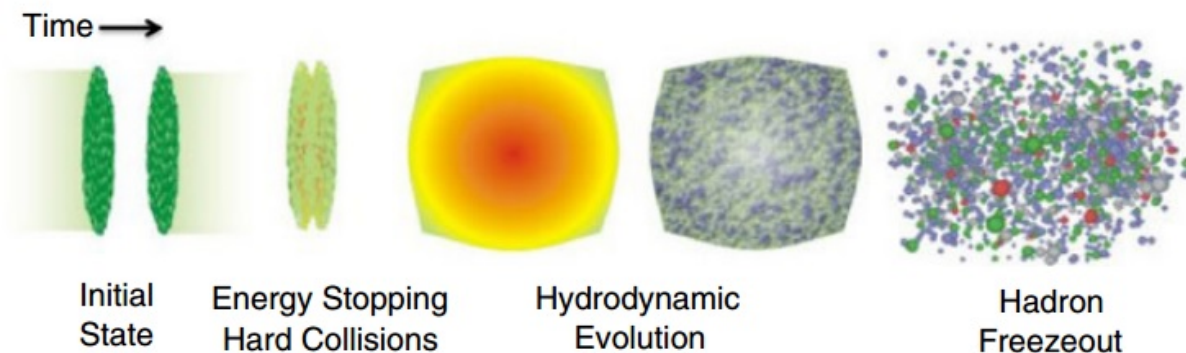
Figure 1.4: The time evolution of a high-energy heavy-ion collisions [10]

1.4 Nuclear Matter effects

Proton-nucleus collisions are effective to scrutinize cold nuclear matter (CNM) effects which modifies nuclear parton distribution functions (nPDF). The CNM effects contain cold nuclear matter energy loss, gluon saturation, gluon shadowing and so on. Measurement of hadron production with a wide p_T range in p-Pb and Pb-Pb collisions are essential to constrain gluon shadowing at region of small values of the longitudinal parton momentum fraction x.

The shadowing is an apparent depletion of the structure function in the nucleus at small x ($x \leq 10^{-2}$) as compared to the corresponding nucleonic ones. The structure function ratio of nuclei relative to deuterium, $R_{F_2}^A \equiv F_2^A/F_2^D$, is expressed in terms of nuclear parton distributions by the lowest order relation in the QCD improved parton model. The nuclear effects for each flavour in the parton distributions are defined by following formula,

$$R_i^A(x, Q^2) \equiv \frac{f_{i/A}(x, Q^2)}{f_i(x, Q^2)} \tag{1.1}$$

where f_i is parton distribution function in the free proton of the each flavour i [11]. The functions are formed to explain Bjorken scaling in deep inelastic scattering (DIS) data. As illustrated in Fig.1.5, it roughly indicates which x-regions are meant by the commonly used terms. For $F_2^A < F_2^D$ ($f_{i/A} < f_i$), the ratio is smaller than unity, $R_{F_2}^A \leq 1$ ($R_i^A \leq 1$). This depletion is known as shadowing at $x < 10^{-1}$. The ratio is larger than unity, $R_{F_2}^A \geq 1$ ($R_i^A \geq 1$), by a few percent; this enhancement is sometimes called anti-shadowing at $x \sim 10^{-1}$ [12]. This effect is usually attributed to coherence effects or to gluon saturation. The gluon saturation refers to the nonlinear dynamics of gluons at small x where due to large densities, they tend to fuse rather than split. The Color Glass Condensate (CGC) model [13, 14] is a classical description of this saturation effect.

The CGC model describes properties of the gluon saturated state which occurs at the high energy. The function of gluon is to confine quarks to the nucleon by binding with strong force. However, the gluons are generated in large amounts in the nucleon as energy increases to the LHC energy. Then the nucleon becomes saturated state of gluons with high density, called Color Glass Condensate.

The CNM effects can be studied via nuclear-modified parton distribution functions in collinearly factorized pQCD calculations. The recent version of nPDF obtained by global fits at next-to-leading order (NLO) to DIS, Drell-Yan, or π^0 RHIC data are EPS09 [15], EPS09s [16], HKN07 [17], nDS [18] and nCTEQ15 [19]. The CGC theory provides agreement in results in p-A (d-A) collisions measured by LHC (RHIC), like charged particle multiplicity density or yield suppression relative to pp collisions. It is suggested to be realized in high-energy heavy-ion collisions since $x \sim 10^{-2}$ at RHIC and $x \sim 5 \times 10^{-4}$ at LHC. Cronin effect [20], be also called p_T broadening, is an enhancement of particle yield in p-A collisions compared to the binary collisions scaled pp results at intermediate-p_T ($p_T \sim 4$ GeV/c) region due to multiple interactions which is that incoming (soft) partons, both quarks and gluons, undergo multiple scatterings with surrounding nucleons via soft gluon exchanges, in nuclear matter [21]. This effect brings about a nuclear modification factor above unity at intermediate-p_T [22].

The EPS09s is a framework of the spatial dependence of the nPDF. Both the LO and NLO cases have been considered, and with EPS09 the spatial dependence has been extracted also for all the 30 error sets. The spatial dependence is introduced in terms of powers of the nuclear thickness functions $T_A(\mathbf{s})$ which gives the total amount of nuclear matter in a colliding nucleus A in the beam
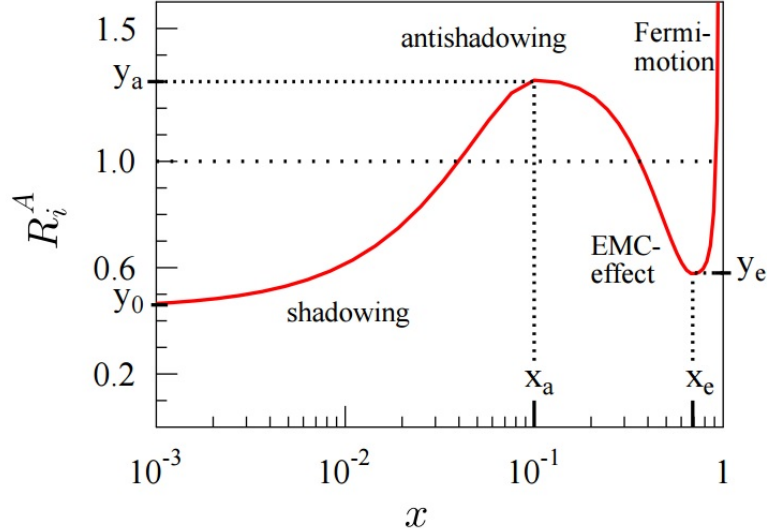
Figure 1.5: The ratio of nuclear parton distribution to nucleon as function of fraction x [15]

direction z at a transverse position $\mathbf{s}$ based on the Woods-Saxon distribution [16]. The collision geometry assumes the Glauber model [23].

Final-state effects in p-A collisions may origin from energy loss or interactions between the final-state particles in a possible collective expansion. The detail study of identified particle spectra in a broad p_T range is useful to constrain theoretical models that try to reproduce measured spectra. The EPOS3 theoretical model [24] based on a viscous hydrodynamical evolution starting from flux tube initial conditions including radial flow in p-Pb collisions describes better the identified particle p_T spectra for all multiplicity classes than models without flow. This model can be additionally tested against π^0 and η meson.

1.5 Photon and neutral meson measurement

A huge number of charged and neutral hadrons, leptons and photons are produced in high energy nucleus collisions. In various particles, photon measurement is one of the important because photons in high-p_T, called prompt photon, prevail for validation of perturbative QCD (pQCD), and photons in low-p_T, called thermal photon, become a probe to convey information of initial-state for QCD matter such as QGP. The advantages of photon measurement are directed probe to propagate purely informations of collision process because the photon does not participate strong interaction.

Prompt photon

The prompt photon is generated in early state of collisions. Generation origin is hard scattering, the quark-gluon compton scattering ($q + g \rightarrow q + \gamma$), quark-antiquark annihilation ($q + \bar{q} \rightarrow g + \gamma$)

and so on. The Feynman diagrams are shown in Fig.1.6. These generation ratios are calculated by pQCD.
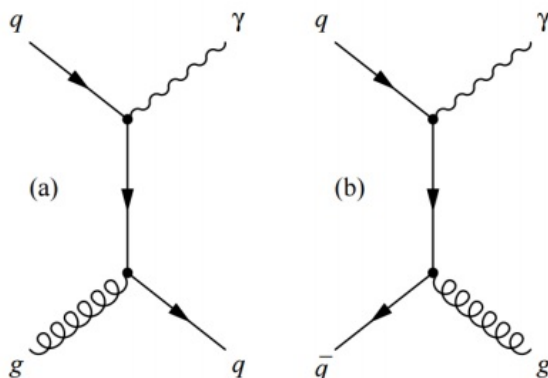
Figure 1.6: Feynman diagrams of prompt photon production by a) quark-gluon compton scattering and b) quark-antiquark annihilation [25]

Thermal photon

The thermal photon is generated in thermal radiation of QGP. This radiation ratio is shown in following:

$$E\frac{dR}{d^3p} = \frac{5}{9}\frac{\alpha\alpha_s}{a\pi^2}T^2e^{-\frac{E}{T}}\ln(\frac{2.912}{g^2}\frac{E}{T}) \tag{1.2}$$

This equipment indicates that the thermal photon exists with $e^{-\frac{E}{T}}$ in low-p_T region [26]. This distribution is important for measuring temperature of QGP. However thermal photon measurement is so difficult on enormous background.

Decay photon

The decay photon is generated by decay of hadron reasonable state. This photon constitutes about 90 % of total photons and its main origin is decay photons from π^0 and η meson. Therefore it is of importance to understand generation mechanism of decay photon and the understand is necessary for thermal photon measurement. The properties of π^0 and η meson are shown in Tab.1.1.

	π^0	η
Mass (MeV/c^2)	134.9766 ± 0.0006	547.862 ± 0.017
I^G(J^{PC})	$1^-(0^{-+})$	$0^+(0^{-+})$
Decay mode (BR)	$\gamma\gamma$ (98.823 ± 0.034) %	$\gamma\gamma$ (39.41 ± 0.20) %
	$e^+e^-\gamma$ (1.174 ± 0.035) %	

Table 1.1: Properties of neutral mesons [27]

1.6 Experimental results

1.6.1 Hadron measurement at RHIC

Experimental results indicating production of QGP was confirmed at STAR and PHENIX. STAR and PHENIX are one of the experiments with Relativistic Heavy Ion Collider (RHIC) at Brookhaven National Laboratory (BNL), and performs heavy-ion collisions, such as copper (Cu), gold (Au) and so on.

The STAR experiment has measured azimuthal particle yields in pp, d-Au and Au-Au collisions. When hot medium is created in heavy-ion collisions, nucleon and other hadrons passing through in the medium have strong interaction and their momentum are changed due to parton energy loss. Therefore measured momentum spectrum in heavy-ion collisions is modified relative to pp collisions (Fig.1.7). Schematic diagram of a hard scattering particles in pp and Pb-Pb collisions is shown
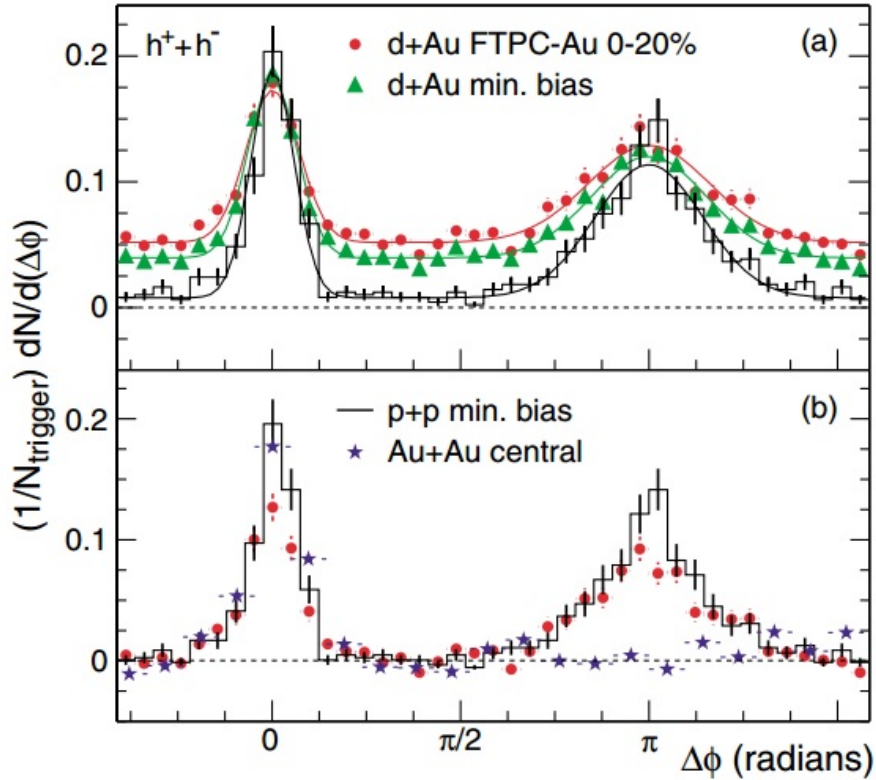
Figure 1.7: Two-particle azimuthal distributions in pp, d-Au and Au-Au collisions [28]

in Fig.1.8. In pp and d-Au collisions, the azimuthal particle yields have clear two jet-like peaks. Jets are observed both near-side and away-side because jet is generated back-to-back direction by two-body scatter and fragmentation of hard partons. On the other hand, in Au-Au collisions, the azimuthal yields of away-side are suppressed relative to pp and d-Au collisions. The away-side peak is vanished due to jet modification effects in the medium [28].

16
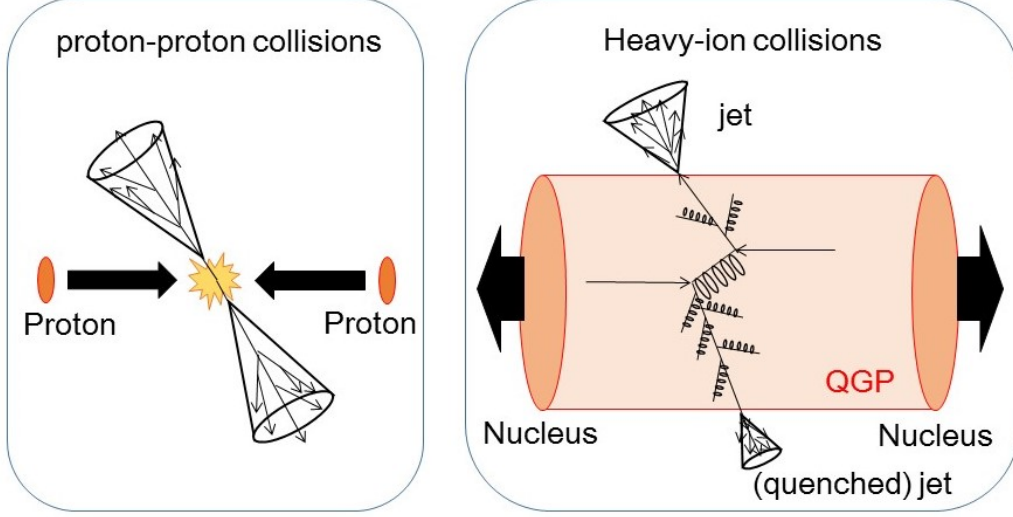
Figure 1.8: Schematic diagram of a hard scattering particle in pp collisions and Pb-Pb collisions

PHENIX has measured the π^0 yields and has observed suppression of the π^0 yields in central (Centrality $0 - 10$ %) Au-Au collisions at $\sqrt{s_{\mathrm{NN}}} = 39$ GeV, 62.4 GeV and 200 GeV as compared to measurement in pp collisions with same centre-of-mass energy [3, 4]. This suppression can be described for the same reason with jet modification as before. The modification of the spectrum is presented quantitatively using nuclear modification factor R_{AA}.

Nuclear modification factor R_{AA}

R_{AA} is given as ratio of the measured invariant yields in nucleus-nucleus collisions to binary collision scaled the invariant yields in pp collisions, defined as:

$$R_{\mathrm{AA}}(p_{\mathrm{T}}) = \frac{\mathrm{d}^2 N/\mathrm{d}p_{\mathrm{T}}\mathrm{d}y|_{\mathrm{AA}}}{\langle T_{\mathrm{AA}} \rangle \times \mathrm{d}^2\sigma/\mathrm{d}p_{\mathrm{T}}\mathrm{d}y|_{\mathrm{pp}}}, \tag{1.3}$$

where $\mathrm{d}^2 N/\mathrm{d}p_{\mathrm{T}}\mathrm{d}y|_{\mathrm{AA}}$ is the invariant yields measured in heavy-ion collisions and $\mathrm{d}^2\sigma/\mathrm{d}p_{\mathrm{T}}\mathrm{d}y|_{\mathrm{pp}}$ is the cross section measured in pp collisions [29]. The nuclear overlap function $\langle T_{\mathrm{AA}} \rangle$ is related to the average number of inelastic nucleon-nucleon collisions defined as:

$$\langle T_{\mathrm{AA}} \rangle = \langle N_{\mathrm{coll}} \rangle / \sigma^{\mathrm{pp}}, \tag{1.4}$$

where $\langle N_{\mathrm{coll}} \rangle$ is the number of binary nucleon-nucleon collisions given from Glauber Monte Carlo simulation [30, 31] and σ_{pp} is the production cross section in pp collisions. The R_{AA} measures the deviation of nucleus-nucleus data from an incoherent suppression of binary collisions. When R_{AA} is less than unity, it indicates interaction between nucleon and produced QCD matter such as QGP. When R_{AA} is consistent with unity, it indicates that the particle production yields can be explained by superposition of production yields in pp collisions and medium is not produced.

Suppression of high-p_T π^0 at RHIC energy

The nuclear modification factor in Au-Au collisions R_{AuAu} for π^0 at RHIC energy is presented in Fig.1.9 and 1.10. Figure 1.9 shows π^0 R_{AuAu} at $\sqrt{s_{NN}} = 200$ GeV with different centrality classes. The R_{AuAu} becomes small with more central collisions and reaches 0.2 in $0 - 10$ % centrality at p_T > 5 GeV/c. Figure 1.10 shows π^0 R_{AuAu} averaged for $p_T > 6$ GeV/c as a function of the number of participants with three different centre-of-mass energy. It indicates that π^0 yields at $\sqrt{s_{NN}} = 62.4$ and 200 GeV are similar suppression at high-p_T. This suppression is stronger than that at $\sqrt{s_{NN}}$ $= 39$ GeV. These results lead us one of suggestions that particles have energy loss caused by the dense QCD medium.
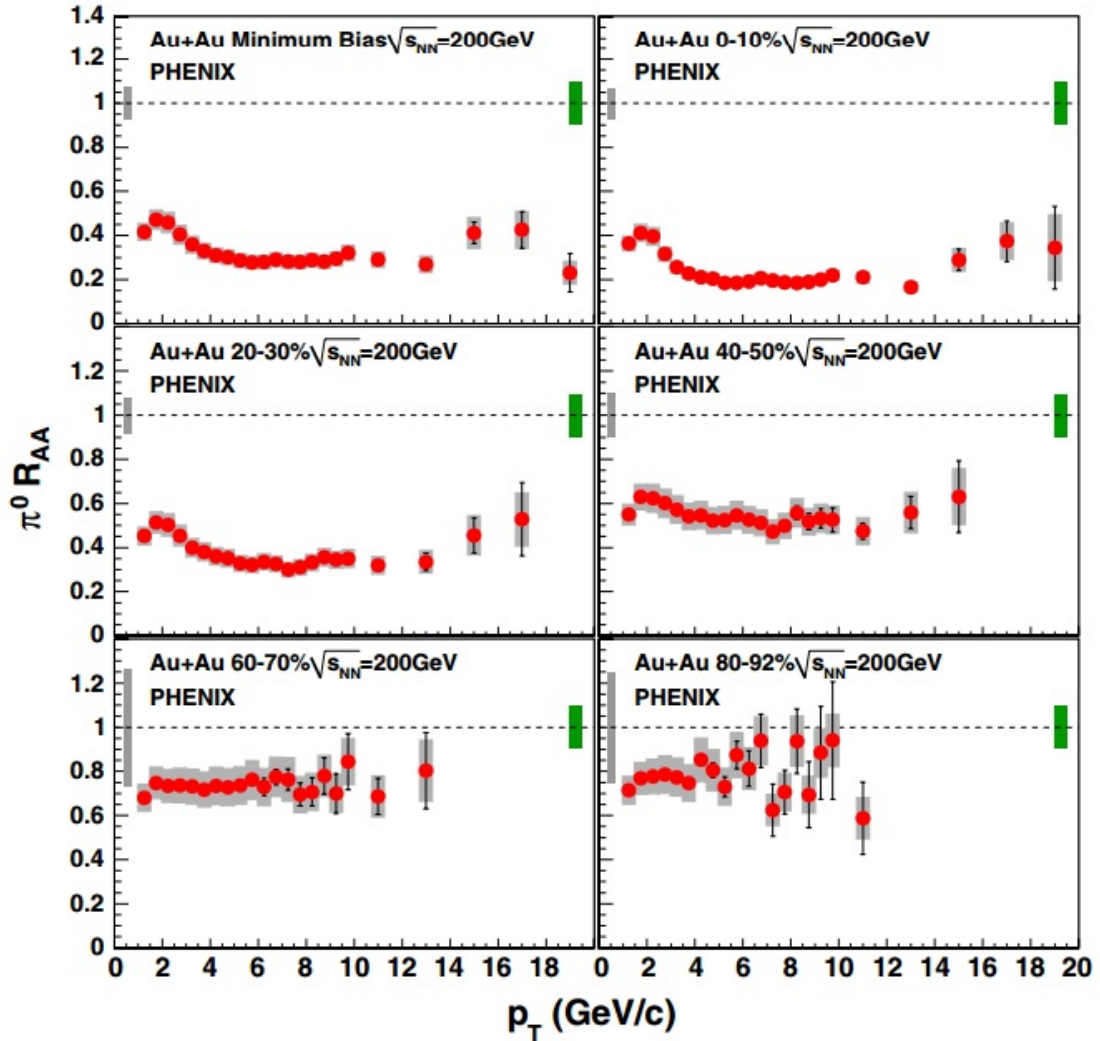
Figure 1.9: Nuclear modification factor of π^0 in Au-Au collisions at $\sqrt{s_{NN}} = 200$ GeV [3]
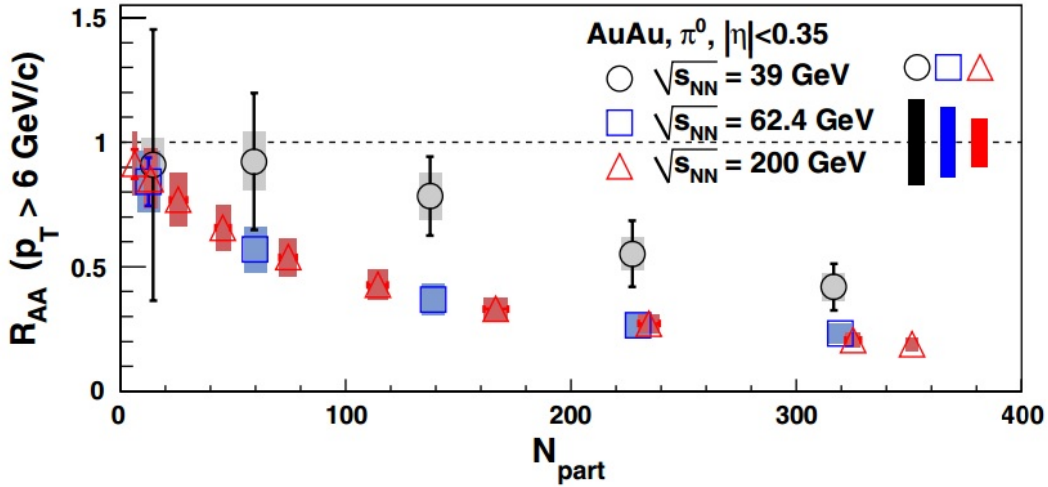
Figure 1.10: Nuclear modification factor of π^0 in Au-Au collisions with different centre-of-mass energy [4]

1.6.2 Neutral meson measurement at LHC

This section summarizes experimental results for neutral mesons measurement at LHC. The ALICE experiment measures neutral meson yields in pp and Pb-Pb collisions at TeV energy region.

Neutral meson yields in pp and Pb-Pb collisions

The ALICE experiment has measured the π^0 and η meson invariant yields in pp collisions at $\sqrt{s}$ = 0.9, 2.76, 7 and 8 TeV and $\sqrt{s}$ = 0.9, 2.76 and 7 TeV, respectively [2, 32, 34]. The invariant yields in pp collisions shown in Fig.1.11, are described by NLO pQCD predictions which is MSTW parton distribution functions (PDFs) and DSS14 fragmentation functions (FF) describing hadronization process of quark, for π^0, and CTEQ6M5 PDFs and AES FF for η meson. The ratio of data corresponding to fit is presented in the bottom panel in Fig.1.11. It is reasonable agreement between data and NLO pQCD predictions for $\sqrt{s}$ = 0.9 and 2.76 TeV. But discrepancy between data and pQCD predictions increases with increasing p_T and centre-of-mass energy. In addition to neutral mesons measurement in pp collisions, ALICE has measured π^0 and η meson yields in Pb-Pb collisions at $\sqrt{s_{NN}}$ = 2.76 TeV (Fig.1.12 and 1.13) [2, 33, 34]. Figure 1.12 shows π^0 invariant yields produced in pp collisions in 2011 LHC run and Pb-Pb collisions in 2010 LHC run with six centrality classes, $0 - 5$ %, $5 - 10$ %, $10 - 20$ %, $20 - 40$ %, $40 - 60$ % and $60 - 80$ % [2]. Clear modification of the spectrum is seen in the central Pb-Pb collisions.

Figure 1.13 shows the π^0 and η meson invariant yields in Pb-Pb collisions in 2011 LHC run [34]. The 2011 data has about 10 times as much statistics as the 2010 data and it leads us π^0 measurements with a wide p_T range up 20 GeV/c and first η meson measurement in Pb-Pb collisions at the LHC. The π^0 and η meson yields are compared to scaled NLO pQCD calculations with MSTW PDFs and different FFs, DSS14 for π^0 and DSS07 for η meson, and both measurements are suppressed respect to NLO pQCD calculations [35].
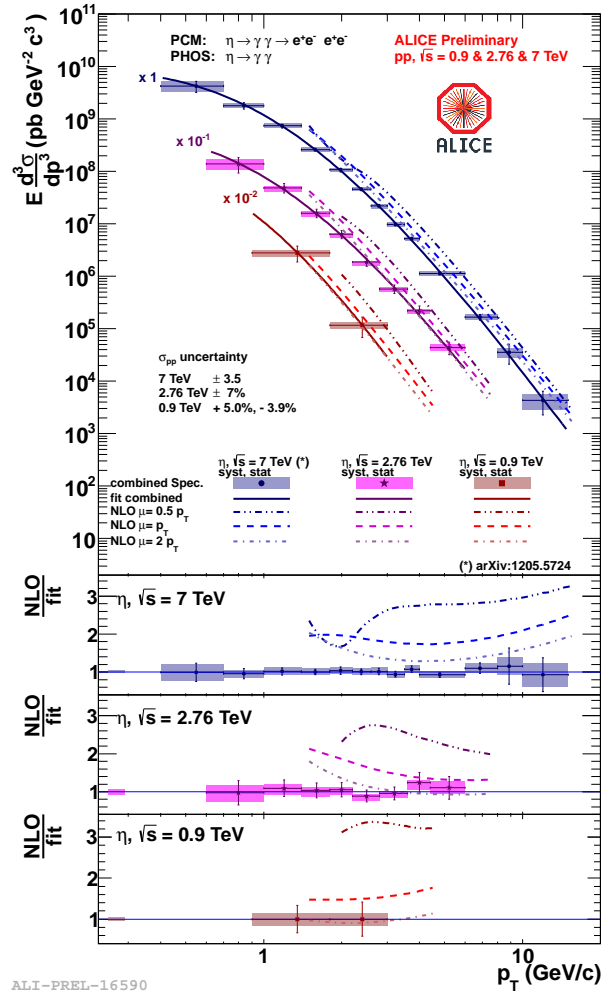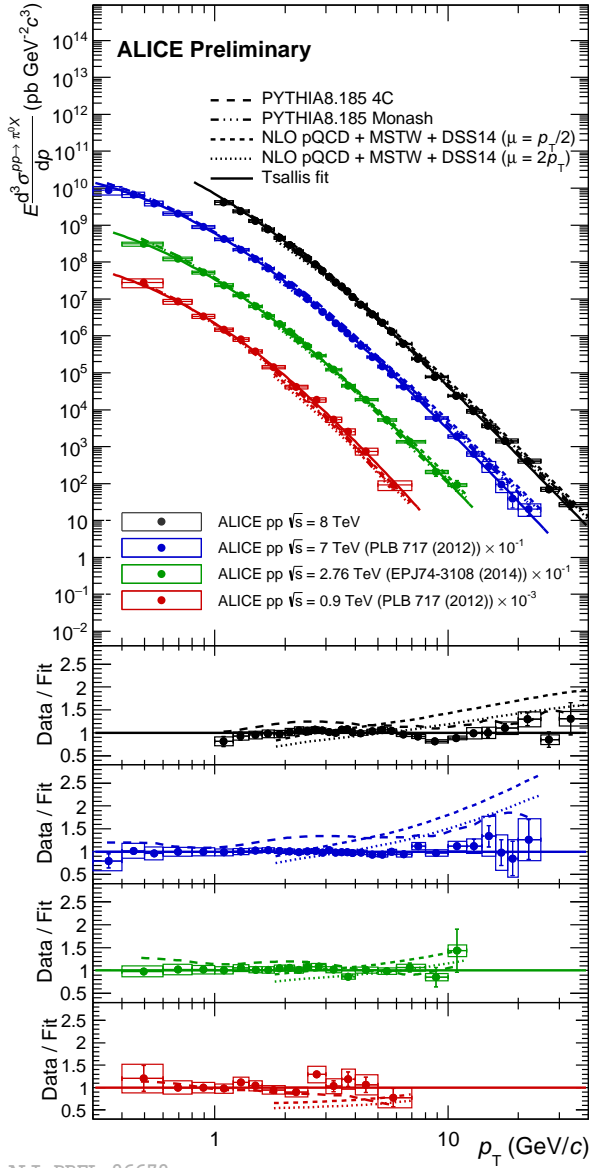
Figure 1.11: Cross section of π^0 in pp collisions with four centre-of-mass energies (left) and cross section of η meson in pp collisions with three centre-of-mass energies (right), and compared to NLO pQCD predictions
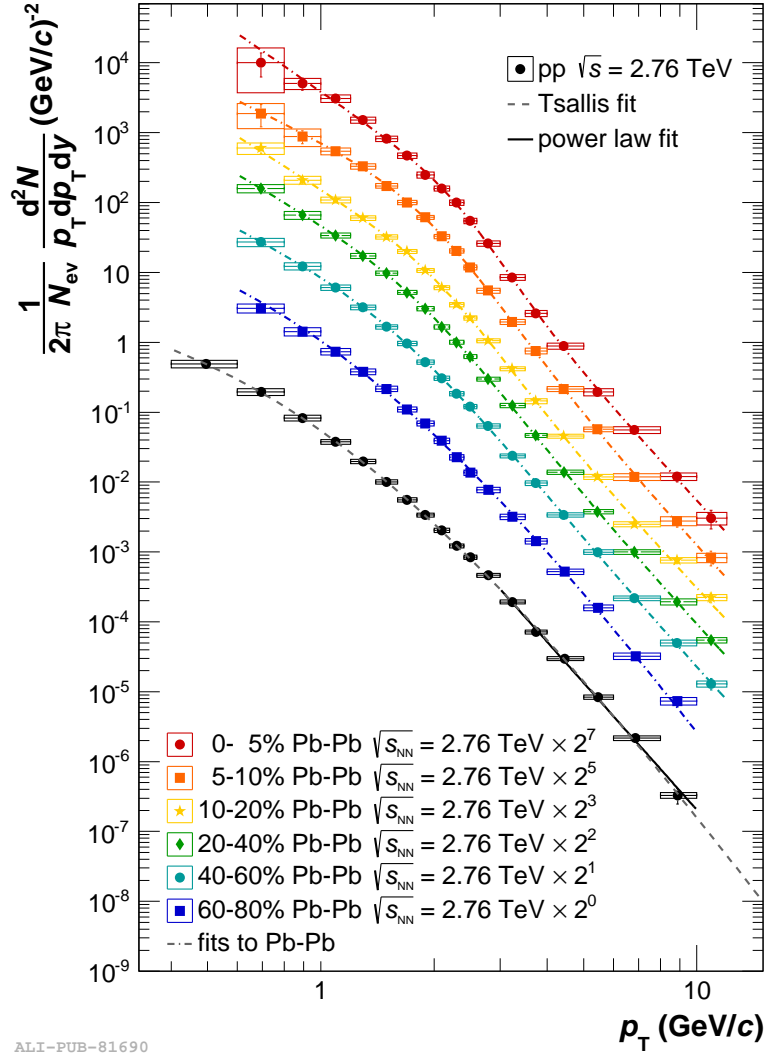
Figure 1.12: The π^0 invariant yields in pp collisions (2011 LHC run) and in Pb-Pb collisions (2010 LHC run) at $\sqrt{s_{NN}} = 2.76$ TeV with six centrality classes

The η/π^0 ratios are calculated in pp collisions at two centre-of-mass energies, $\sqrt{s} = 2.76$ and 7 TeV (Fig.1.14) and Pb-Pb collisions at $\sqrt{s_{NN}} = 2.76$ TeV (Fig.1.15). All ratios grow in low-p_T region ($p_T < 3$ GeV/c) and reach a plateau of about 0.5 above 3 GeV/c. The pQCD calculations which use CTEQ6M5 PDFs, and DSS FF for π^0 and AEF FF for η meson, describe data in pp collisions in Fig.1.14. The ratios measured at ALICE is compared to world results in pp collisions at all energies from 13.8 GeV to 200 GeV measured at RHIC or at SPS in Fig.1.16 and is consistent with others. Figure 1.15 shows the η/π^0 ratio measured in Pb-Pb collisions with two centrality classes [34]. It is compared to pp measurement [32] and $K^\pm/\pi^\pm$ ratio measurement in central Pb-Pb collisions at the same centre-of-mass energy [36]. The η/π^0 ratio in Pb-Pb collisions is comparable value and similar behavior with that in pp collisions and $K^\pm/\pi^\pm$ ratio. The pQCD
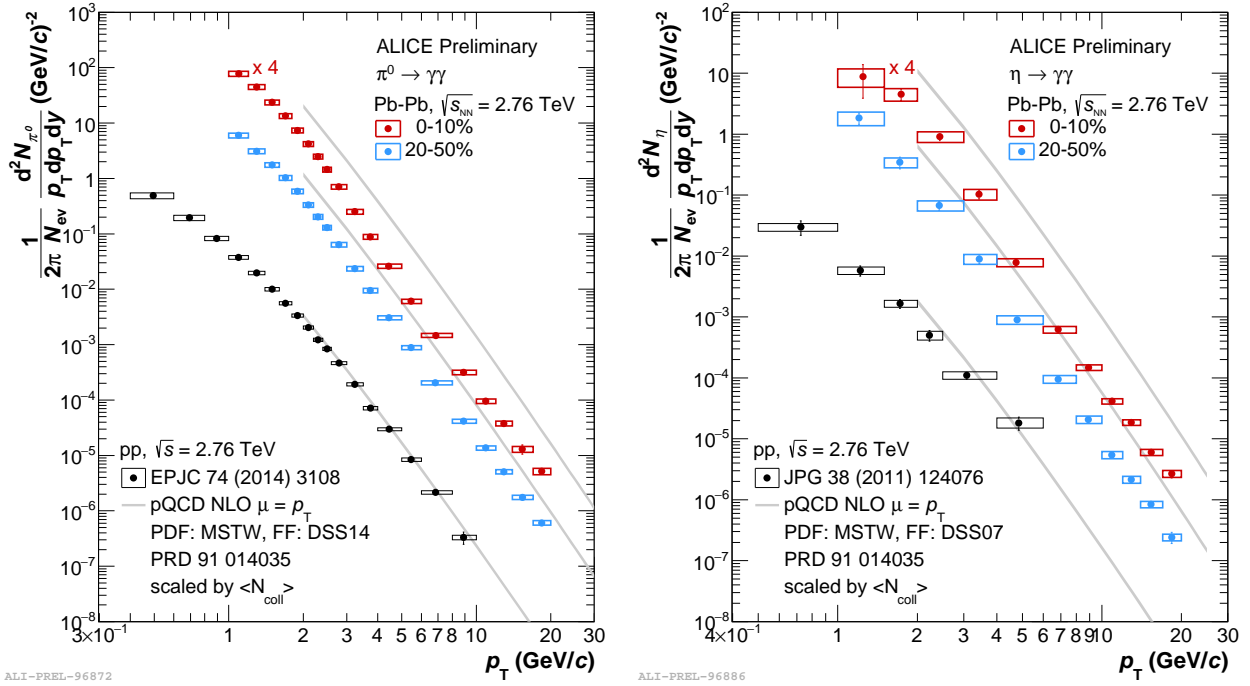
Figure 1.13: Invariant yields in Pb-Pb collisions (2011 LHC run) at $\sqrt{s_{\mathrm{NN}}} = 2.76$ TeV for π^0 (left) and for η (right)

NLO calculations at high-p_{T} with energy loss reproduce the data.

Strong suppression of high-p_{T} π^0 at LHC energy

Strong suppression of high-p_{T} π^0 is observed in Pb-Pb collisions (Fig.1.17 and 1.18). ALICE has measured π^0 nuclear modification factor defined by Eq.1.3 with six centrality classes. Figure 1.17 shows π^0 R_{AA} at three centrality classes, $0 - 5$ %, $20 - 40$ % and $60 - 80$ %. Measured R_{AA} at all centrality classes have a maximum around $1 - 2$ GeV/c, decrease with p_{T} and reach a constant value in high-p_{T} region. In peripheral collisions ($60 - 80$ %) moderate suppression ($R_{\mathrm{AA}} \sim 0.5 - 0.7$) is observed. The suppression becomes stronger with increasing p_{T} and the strongest suppression ($R_{\mathrm{AA}} \sim 0.1$) with no p_{T} dependence at $p_{\mathrm{T}} > 5$ GeV/c is observed in most central collisions ($0 - 5$ %). The difference of centre-of-mass energy in π^0 R_{AA} is shown in Fig.1.18. The R_{AA} measured at LHC (ALICE collaboration, Pb-Pb collisions at $\sqrt{s_{\mathrm{NN}}} = 2.76$ TeV) is compared to that measured at RHIC (PHENIX collaboration, Au-Au collisions at $\sqrt{s_{\mathrm{NN}}} = 39, 62.4$ and 200 GeV) and at SPS (WA98 collaboration, Pb-Pb collisions at $\sqrt{s_{\mathrm{NN}}} = 17.3$ GeV). Decreasing R_{AA} with increasing centre-of-mass energy is observed and the suppression at LHC is stronger than others.

1.6.3 Direct photon measurement

Direct photon spectra in Pb-Pb collisions at $\sqrt{s_{\mathrm{NN}}} = 2.76$ TeV for $0 - 20$ %, $20 - 40$ % and $40 - 80$ % centrality classes compared to pQCD NLO calculations is shown in Fig.1.19. An excess of direct photon at the low-p_{T} region, $p_{\mathrm{T}} < 4$ GeV/c, is observed in central and mid-central
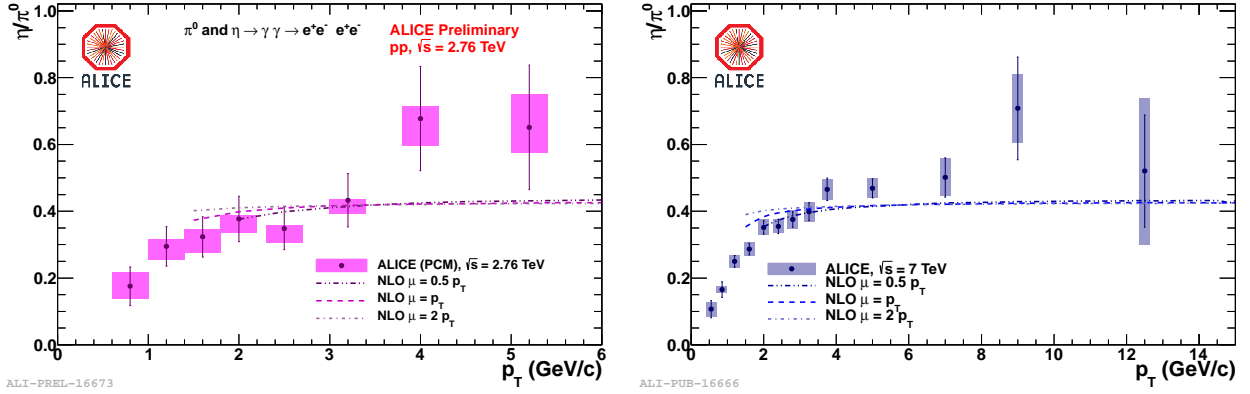
Figure 1.14: The η/π^0 ratio in pp collisions at $\sqrt{s} = 2.76$ TeV (left) and 7 TeV (right)
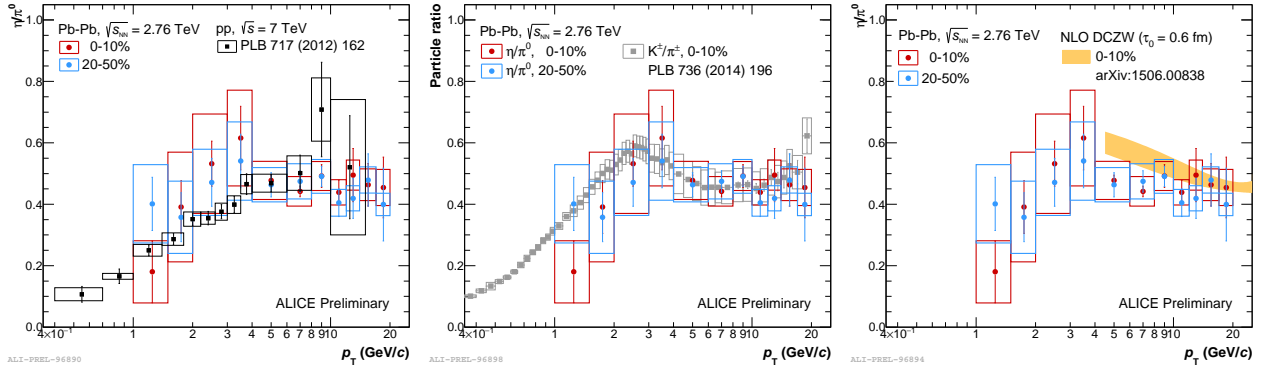
Figure 1.15: The η/π^0 ratio in Pb-Pb collisions at $\sqrt{s_{NN}} = 2.76$ TeV compared to pp measurement (left), $K^{\pm}/\pi^{\pm}$ in Pb-Pb collisions (middle) and NLO pQCD calculations (right)
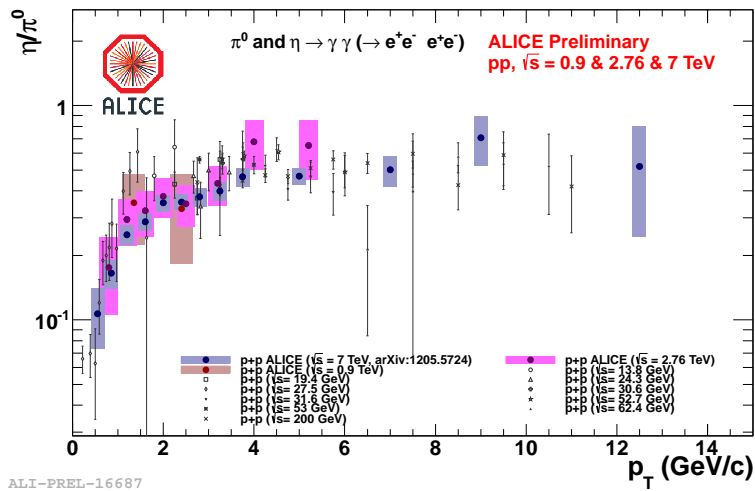
Figure 1.16: The η/π^0 ratio in pp collisions at ALICE compared to world results
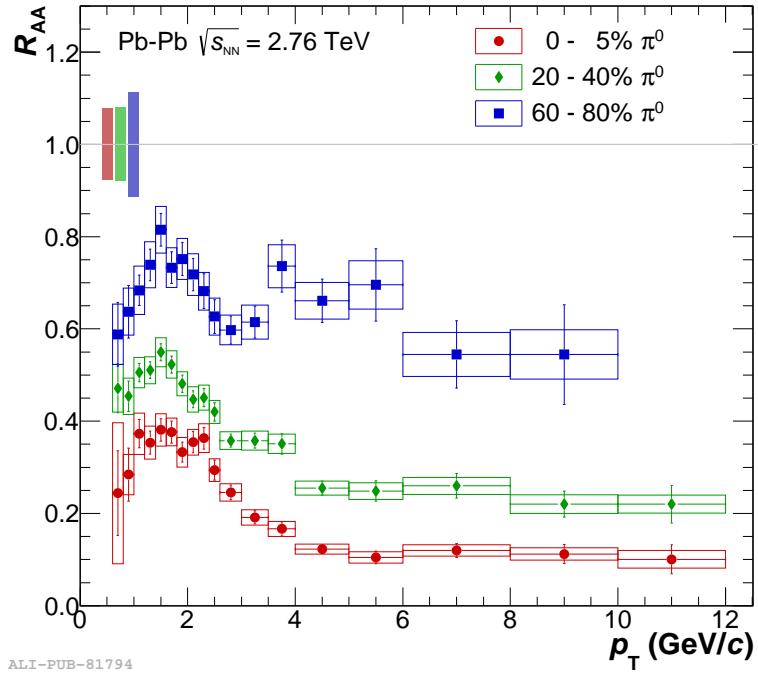
Figure 1.17: Nuclear modification factor for π^0 in Pb-Pb collisions with three centrality classes
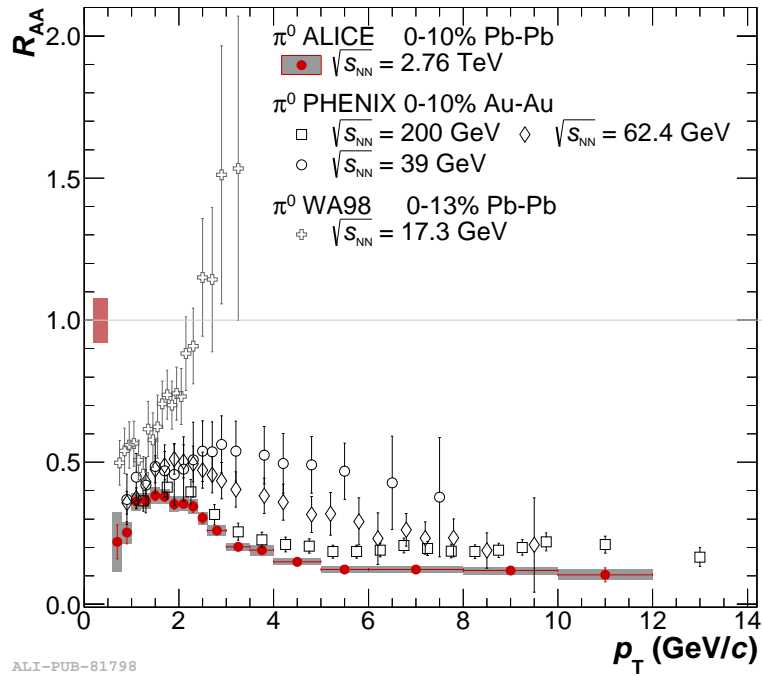
Figure 1.18: Nuclear modification factor for π^0 comparison to world results

24

collisions with respect to the pQCD predictions. The excess in central collisions is larger than that in mid-central collisions and this excess might be related to thermal photons. The inverse slope for the excess reflects effective temperature averaged over the different temperatures during the space-time evolution of the medium. The low-p_T region is selected in order to extract the slope parameter because the prompt photons contributions are small. Remaining excess yield is fit with an exponential function ($\propto \exp(\text{-}p_\mathrm{T}/T_\mathrm{eff})$) after subtraction of pQCD component. The extracted inverse slope parameter is $T_\mathrm{eff}^\mathrm{subtr} = 297 \pm 12^\mathrm{stat} \pm 41^\mathrm{syst}$ MeV in the range $0.9 < p_\mathrm{T} < 2.1$ GeV/c for the $0-20$ % centrality class. In the case of extraction without the subtraction of pQCD photons, the inverse slope parameter is $T_\mathrm{eff} = 304 \pm 11^\mathrm{stat} \pm 40^\mathrm{syst}$ MeV for the $0-20$ % centrality class (Fig.1.20) [37]. The direct photon spectra are compared with results in Au-Au collisions at $\sqrt{s_\mathrm{NN}}$ = 200 GeV at RHIC-PHENIX measurements with two centrality classes in Fig.1.20. In the central collisions, the ALICE results have larger slope parameter than the PHENIX results ($T_\mathrm{eff} = 239 \pm 25^\mathrm{stat} \pm 7^\mathrm{syst}$ MeV) [38,39]. This result means that the medium with a higher initial temperature is created at the larger centre-of-mass energy.

In addition, nuclear modification factor for direct photon is measured in Pb-Pb collisions with $0-20$ % centrality class (Fig.1.21). At the low-p_T region ($p_\mathrm{T} < 6$ GeV/c), it is clearly seen the enhancement corresponding to contributions from thermal photons. On the other hand, at the high-p_T region ($p_\mathrm{T} > 6$ GeV/c), although the π^0 is strongly suppressed (as described before), the direct photon is not suppressed and its R_AA is consistent with unity. This result provides photons pass through in the medium without interactions. Therefore these results support the hot medium created in the heavy-ion collisions has strong interaction.

1.7   Physics motivation

Neutral mesons (π^0 and η meson) are produced from parton fragmentation in the QCD vacuum in pp collisions. The neutral meson measurement is important for test of the pQCD predictions and understanding particle production mechanism. On the other hand, the measurement in Pb-Pb collisions is studied to interpret the hadron suppression and parton energy loss in the QGP. In addition, the precise π^0 and η meson measurement over a large p_T range is a essential for understanding the decay photon background for a direct photon measurement.

The ALICE experiment has measured π^0 and η meson in pp and Pb-Pb collisions. The π^0 cross sections measured in pp collisions with various collision energies, $\sqrt{s}$ = 0.9, 2.76, 7 and 8 TeV have reasonable agreement with pQCD model calculations. The π^0 measurement in Pb-Pb collisions is observed strong suppression at high-p_T relative to that in pp collisions. The π^0 suppression in the most central collisions reaches factor of $8-10$ at a maximum at intermediate-p_T region and that in Pb-Pb collisions at LHC is stronger than in Au-Au collisions at RHIC for all centralities. This phenomena suggests us creation of the hot and dense QCD matter, e.g. QGP. However, there are various processes involving transport properties of the QCD medium and initial-state effects to explain the suppression mechanism. Therefore studies in p-Pb collisions which does not create the QGP, become important because it is intermediate collisions between pp collisions and Pb-Pb collisions in terms of system size and number of produced particles.

This thesis reports the π^0 and η meson measurement in p-Pb collisions at $\sqrt{s_\mathrm{NN}} = 5.02$ TeV. The π^0 and η meson invariant yields, η/π^0 ratio and nuclear modification factor for π^0 as a function of
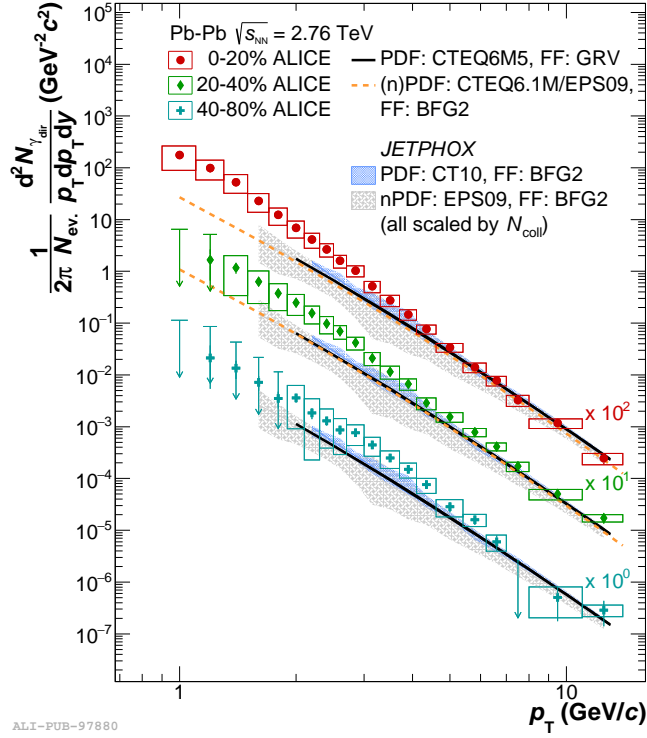
Figure 1.19: Direct photon spectra in Pb-Pb collisions at $\sqrt{s_{\mathrm{NN}}} = 2.76$ TeV with different centrality classes compared to NLO pQCD calculations [37]
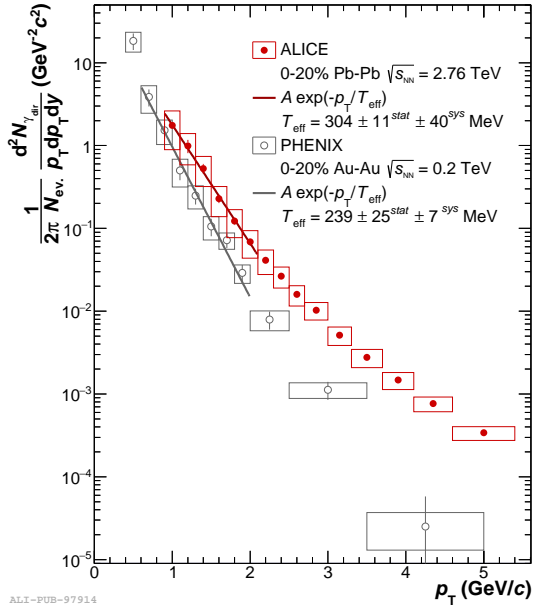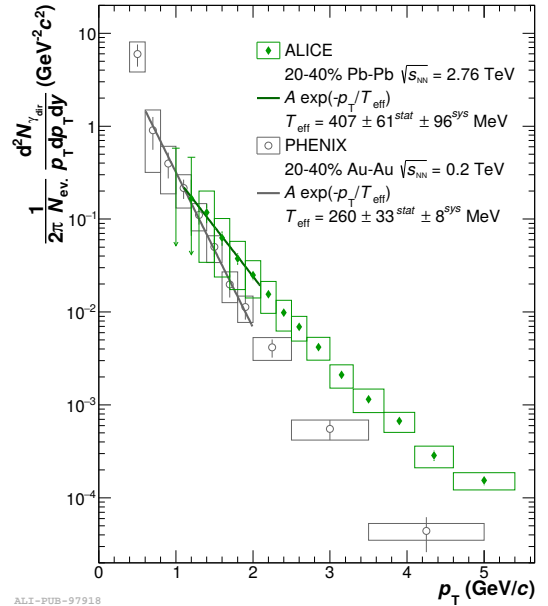
Figure 1.20: Direct photon spectra between ALICE and PHENIX for $0-20$ % centrality classes (left) and $20-40$ % centrality classes (right) [37, 39]

26
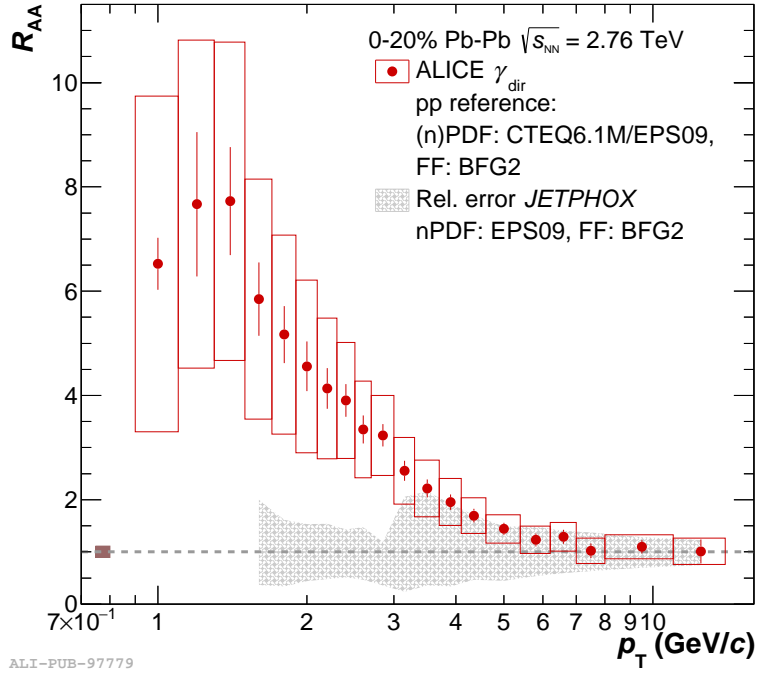
Figure 1.21: Direct photon R_{AA} in central $(0-20\ \%)$ Pb-Pb collisions at $\sqrt{s_{\mathrm{NN}}} = 2.76$ TeV

p_{T} are shown in this paper. These results could support to disentangle particle yield suppression originating from initial-state effects in the colliding nuclei or from final-state effects in the Pb-Pb collisions at LHC energies.

Chapter 2

Experimental setup

2.1 LHC accelerator

Large Hadron Collider (LHC) is a two-ring-superconducting-hadron accelerator and collider, which exists under the ground of border between France and Switzerland. It is the largest accelerator in the world installed in the 26.7 km long circular. It is designed to collide protons with a centre-of-mass energy of 14 TeV ($\sqrt{s} = 14$ TeV) and an unprecedented luminosity of $10^{34} \text{cm}^{-2}\text{s}^{-1}$. It can also collide heavy ions with an energy 2.8 TeV per nucleon ($\sqrt{s_{\text{NN}}} = 2.8$ TeV) and a peak luminosity of $10^{27} \text{cm}^{-2}\text{s}^{-1}$ [40]. The LHC had run from 2009 and ALICE took physical data of pp collisions at $\sqrt{s} = 900$ GeV. It took data of pp collisions at $\sqrt{s} = 2.76$, 7 and 8 TeV and Pb-Pb collisions at $\sqrt{s_{\text{NN}}} = 2.76$ TeV from 2010 to 2013. In addition, data of p-Pb collisions at $\sqrt{s_{\text{NN}}} = 5.02$ TeV was taken in beginning of 2013.

The protons stripped atoms of their electrons by electric field at Linear accelerator 2 (Linac 2) which is the starting point for the protons used in experiments at CERN. The protons are accelerated by the Linac 2 to the energy of 50 MeV (first acceleration in the chain), and then enter the Proton Synchrotron Booster (PSB). The beams of protons are accelerated to energy of 1.4 GeV at PSB, and injected to the Proton Synchrotron (PS) which gains to 25 GeV. After that protons are carried to the Super Proton Synchrotron (SPS) which accelerates them to 450 GeV. Finally, the protons are sent to the two ring beam pipe of the LHC. This is accelerator chain in the CERN. On the other hand, lead ions start from Linac 3 and enter the Low Energy Ion Ring (LEIR) which transforms them from long pulses into the short and dense bunches suitable for injection to the LHC. The lead ions beams are moved to PS and then they follow the same route as the protons [42].

2.2 The ALICE experiment

ALICE (A Large Ion Collider Experiment) is an experiment at the LHC. The ALICE experiment is designed to address the physics of strongly interacting matter and QGP at extreme values of energy density and temperature in nucleus-nucleus collisions. The ALICE detector is built by a collaboration including currently 1600 members from 164 institutes 41 countries [43]. The ALICE apparatus has overall dimensions are $16 \times 16 \times 26$ m^3 with a total weight of approximately 10000 t. The seventeen ALICE detector systems fall into three categories, central barrel detec-

Figure 2.1: CERN's accelerator complex [41]

tors, forward detectors and the muon spectrometer. The central barrel detectors include Inner Tracking System (ITS), Time Projection Chamber (TPC), Transition Radiation Detector (TRD), Time Of Flight (TOF), PHOton Spectrometer (PHOS), Electro-Magnetic Calorimeter (EMCal) and High Momentum Particle Identification Detector (HMPID). The forward detectors include the Photon Multiplicity Detector (PMD) and the silicon Forward Multiplicity Detector (FMD), quartz cherenkov detector (T0) and Zero Degree Calorimeter (ZDC).
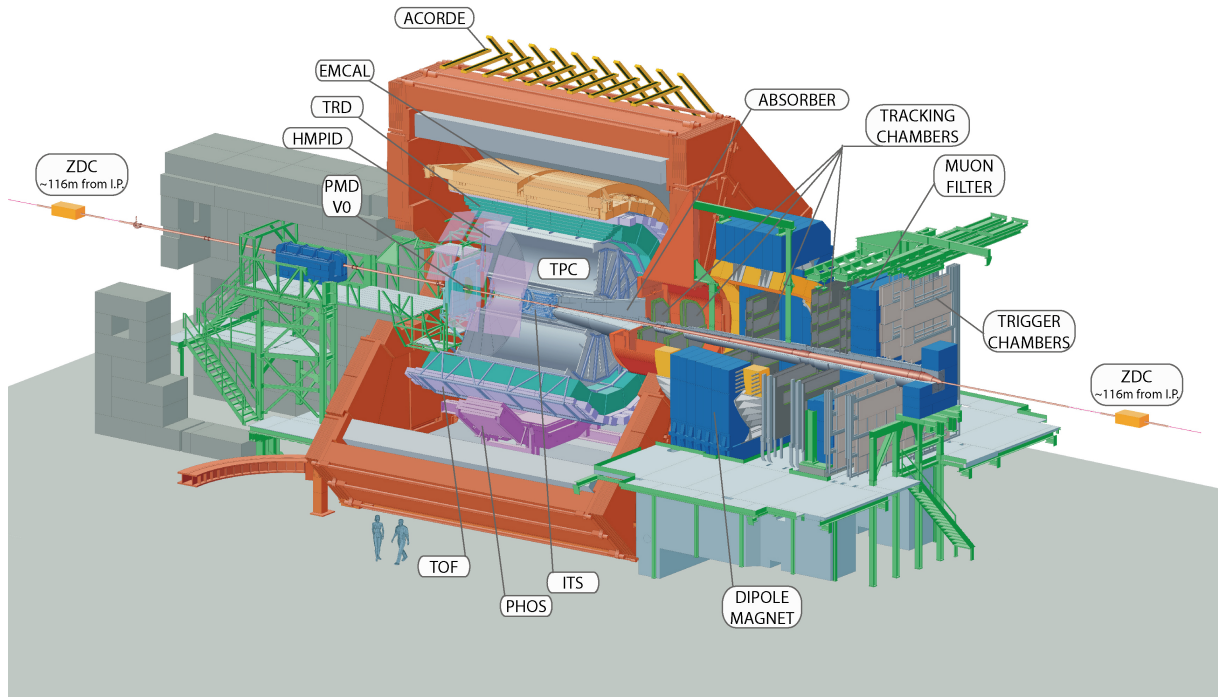
Figure 2.2: The ALICE detector

2.3 Detector Description

2.3.1 PHOS (PHOton Spectrometer)

PHOS (PHOton Spectrometer) [45,46] which is developed communally by the quark experimental laboratory at the Hiroshima University and the Russian group, is an electro-magnetic calorimeter designed to measure energy and hit coordinates of photons and electrons (Fig.2.3). During the LHC-Run1 $(2009 - 2013)$, PHOS is installed 3 modules at a distance of 4.6 m from the ALICE interaction point and covers $|\eta| < 0.13$ in pseudorapidity and the acceptance of $260° < \phi < 320°$ in azimuthal angle. Each module has 3584 detection channels in a matrix of 64×56 cells. Each detection channel consists of a $2.2 \times 2.2 \times 18$ cm^3 lead tungsten, PbWO$_4$ (PWO), crystal coupled

to an Avalanche Photo Diode (APD) and a low-noise Charged-Sensitive Preamplifier (CSP) shown in Fig.2.4. The PWO crystal size has been chosen to be almost equal to the Molière radius (2 cm). The height of the crystal (18 cm) corresponds to 20 radiation lengths.   PHOS operates
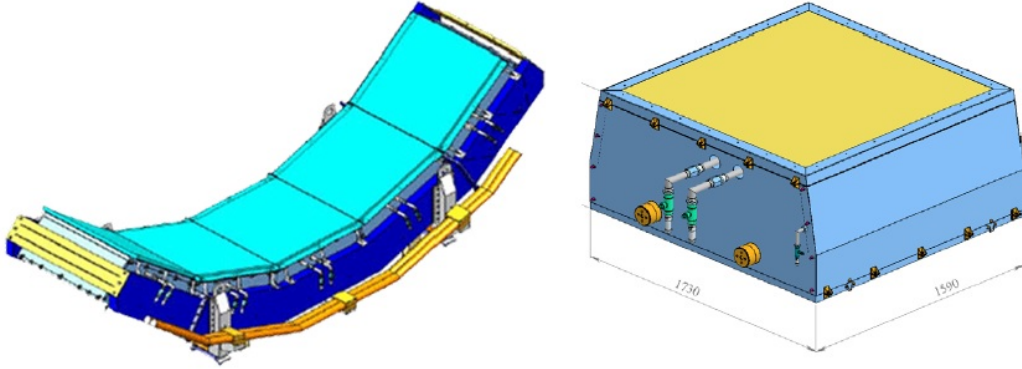
Figure 2.3: PHOS overview (left) and one PHOS module (right)
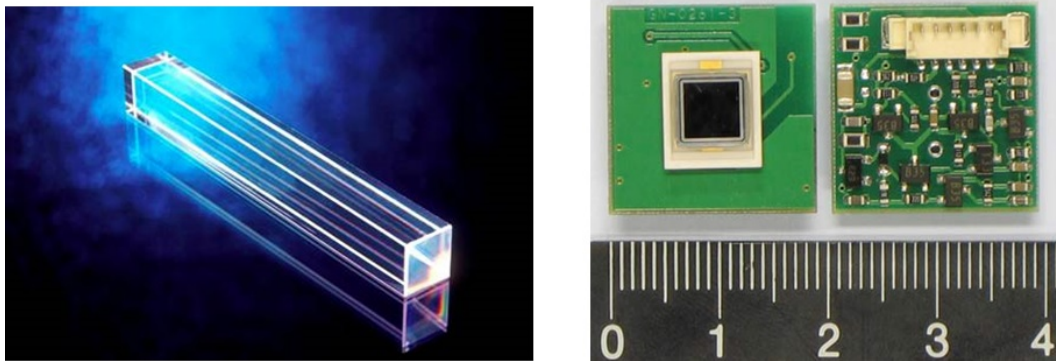
Figure 2.4: PWO crystal (left) and APD mounted on the preamplifier (right)

at a temperature of $-25°$C which the yield of PWO crystal will be increased by about a factor of 3 compared to room temperature ($20°$C) and furthermore the electronic noise of the photon detector will be reduced. The result is reported in Fig.2.5. Both effects will lead to improved energy resolution. We have chosen $-25°$C as the working temperature for the PHOS, which can be obtained easily and economically. APD has active area of 5×5 mm^2. The spectral response exhibits a maximum at around 600 nm with a quantum efficiency around 85 %. The CSP on a printed circuit board of area 19×19 mm^2 is mounted to the back side of the APD. It is supplied from $+12$ to -6 V with power consumption of 64 mW.

Energy and position of incoming particles are reconstructed from the amplitudes of signals in the cells measured by the front-end-electronics (FEE). Photon and electron measurement uses interaction between in the crystal by electron-positron pair production and bremsstrahlung. This
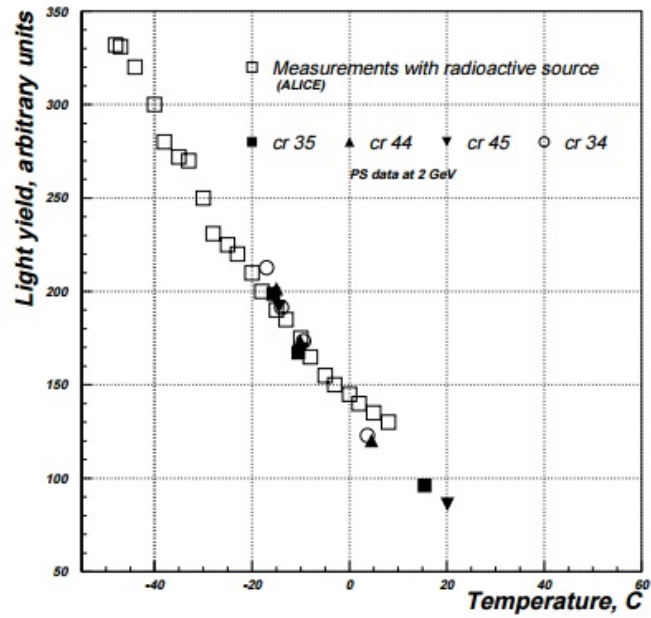
Figure 2.5: Light yield of PbWO$_4$ crystal as a function of temperature
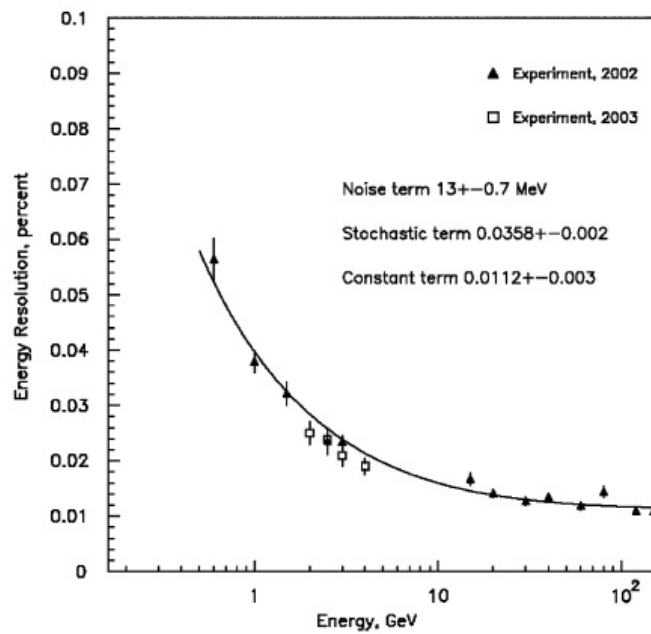
Figure 2.6: Energy resolution as a function of energy

interaction is forbidden to react in the vacuum and is permitted to react by grace of Coulomb field in the nucleus. The pair production reacts when photon energy exceeds sum of the mass of electron $2m_ec^2$. The incident high energy photon in PHOS generates electron and positron by pair production and they generate secondary photons by bremsstrahlung. The secondary photons generate electron-positron pair. This process continues so far as their energies become small less than ionization energy. This phenomenon is called electro-magnetic shower. Light yield in crystal increases via iteration of pair production and bremsstrahlung and is proportionate to incident photon. Energy of the incident photon is measurable to detect all photons generated by electro-magnetic shower.

The energy resolution can be parameterized as

$$\frac{\sigma_E}{E} = \sqrt{\left(\frac{a}{E}\right)^2 + \left(\frac{b}{\sqrt{E}}\right)^2 + c^2} \tag{2.1}$$

where energy E is in GeV, and a represents noise term dominated at the low-p_{T} region, b represents stochastic term due to characteristic of detector dominated at the high-p_{T} region, and constant term c is due to readout inhomogeneity and calibration error. These parameters are determined as follows by electron beam tests with PHOS prototype for a 3×3 detector array, $a = 0.0130 \pm 0.0007$ GeV, $b = 0.036 \pm 0.002 \sqrt{\mathrm{GeV}}$, and $c = 1.12 \pm 0.3$ % (Fig.2.6) [47].

The position resolution can be parameterized as

$$\sigma_{x,y} = \frac{A}{\sqrt{E}} + B. \tag{2.2}$$

The result of beam tests found $A = 3.26$ mm and $B = 0.44$ mm (Fig.2.7). The resulting two-photon invariant mass resolution at the π^0 peak is 3.5 %.

The dynamic range $(0.005 - 80$ GeV$)$ is achieved by selecting an appropriate detector length that minimizes shower leakage for the highest particle energies without deteriorating the energy resolution for the lowest particle energies due to light attenuation.
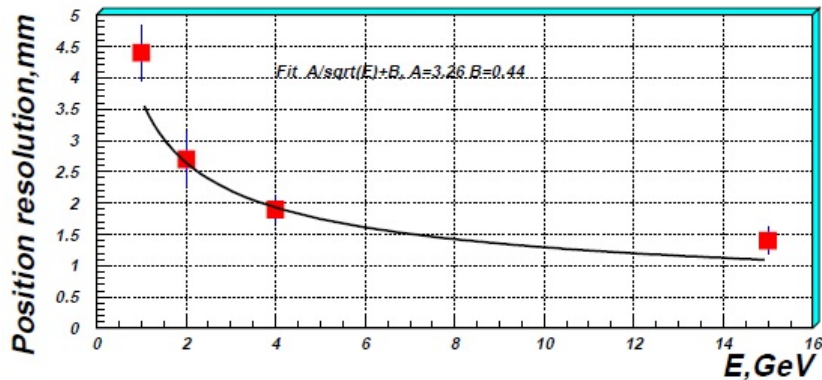
Figure 2.7: Position resolution as a function of energy

33

2.3.2 EMCal (Electro-Magnetic Calorimeter)

EMCal is a lead-scintillator sampling electro-magnetic calorimeter [48]. The EMCal covers pseudorapidity range of $|\eta| < 0.7$ and azimuthal coverage of $80° < \phi < 180°$. Super modules are installed 10 full size with size of $\Delta\eta = 0.7$ and $\Delta\phi = 20°$, and 2 one-third size with size of $\Delta\eta = 0.7$ and $\Delta\phi = 7°$. The full size super module is assembled from $12 \times 24 = 288$ modules and the one-third size super module is assembled from $4 \times 24 = 96$ modules. Each module contains $2 \times 2 = 4$ towers built up from 76 alternating layers of 1.44 mm Pb absorber and 77 layers of 1.76 mm scintillating materials which are penetrated by wavelength shifting fibers. The EMCal consists of 12288 towers (1152 towers per the full size super module and 768 towers per the one-third size super module) which are approximately projective in η and ϕ to the interaction point. The front face dimensions of the towers are 6×6 cm^2 which is chosen to be about twice as large as the Molière radius and the cell length is 20 radiation lengths. Photons and electrons hitting the surface of the EMCal produce an electromagnetic shower which spreads out in longitudinal and transversal direction, depositing energy in multiple towers. Clusterizer algorithms are used to reconstruct the total energy of the impinging particle.
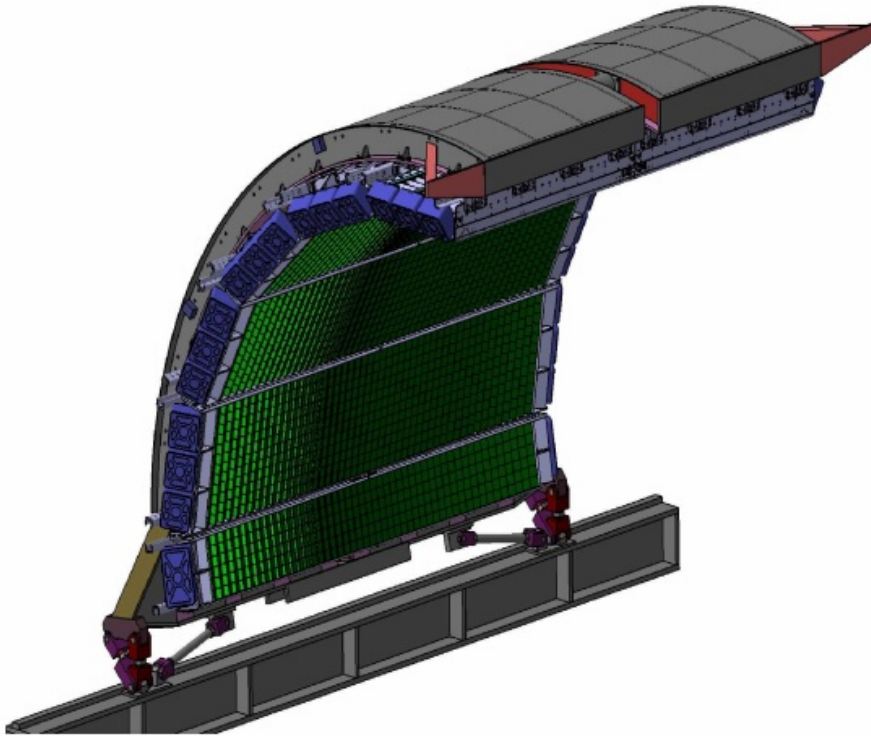
Figure 2.8: EMCal overview [48]

2.3.3 ITS (Inner Tracking System)

ITS [49] consists of six layers of silicon detectors and is located directly around the interaction point covering full azimuth. The two innermost layers are formed by the Silicon Pixel Detectors (SPD) positioned at a radial distance of 3.9 cm and 7.6 cm, followed by two layers of Silicon Drift Detectors (SDD) at 15.0 cm and 23.9 cm, and two layers of Silicon Strip Detectors (SSD) at 38.0 cm and 43.0 cm. While the two SPD layers cover a pseudorapidity range of $|\eta_{lab}| < 2$ and $|\eta_{lab}| < 1.4$, respectively, the SDD and SSD subtend $|\eta_{lab}| < 0.9$ and $|\eta_{lab}| < 1.0$, respectively. The geometrical dimensions and the technology used in the various layers of the ITS are summarized in Tab.2.1.

The ITS provides information for determination of the primary vertex and the secondary vertices for the charm and hyperon reconstruction, track reconstruction and particle identification.
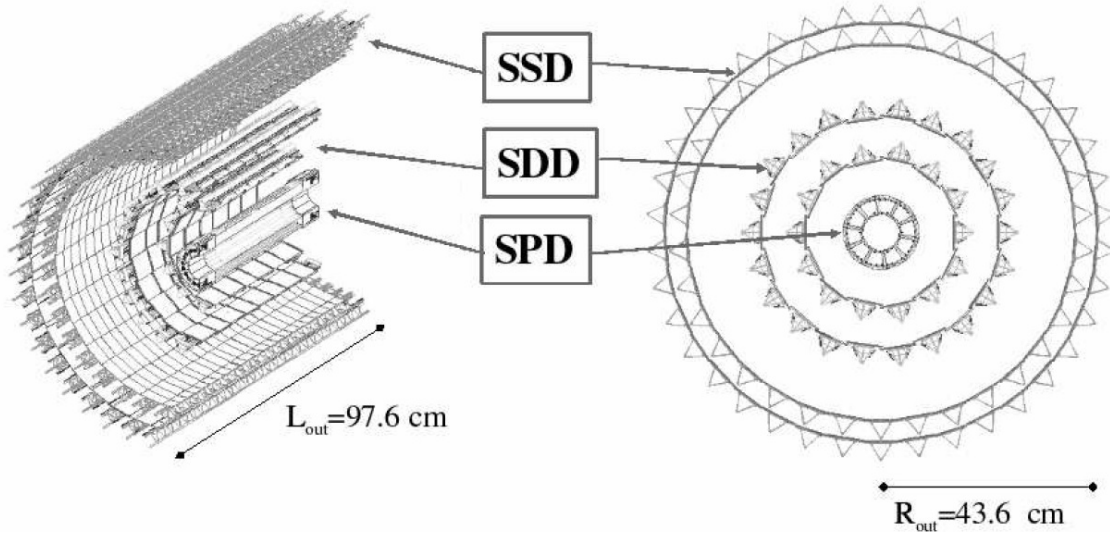
Figure 2.9: ITS overview [45]

Layer	Type	r(cm)	$\pm z$(cm)	Area(m^2)	Ladders	Total channels
1	pixel	4	16.5	0.09	80	5242880
2	pixel	7	16.5	0.18	160	10485760
3	drift	14.9	22.2	0.42	14	43008
4	drift	23.8	29.7	0.89	22	90112
5	strip	39.1	45.1	2.28	34	1201152
6	strip	43.6	50.8	1.88	38	1517568
Total area = 6.74 m^2						

Table 2.1: Dimensions of the ITS detectors (active area) [45]

2.3.4 TPC (Time Projection Chamber)

TPC is the main tracking detector in the central barrel of the ALICE experiment and is a large cylindrical drift detector filled with a Ne/CO2 (90/10%) gas mixture during the period of this data taking. It covers a pseudorapidity range of $|\eta_{\text{lab}}| < 0.9$ over the full azimuthal angle for the maximum track length of 159 reconstructed space points. With the magnetic field of $B = 0.5$ T, the TPC provides track finding with efficiency larger than 90 %, charged particle momentum measurement with resolution better than 2.5 % for electrons at $p_{\text{T}} \sim 4$ and particle identification via the measurement of the specific energy loss ($\mathrm{d}E/\mathrm{d}x$) with a resolution of 5.5 %.

The combination of the different analysis methods leads to the benefit of a direct independent crosscheck of the results. Additionally, all advantages of the different methods are combined, like the good momentum resolution of PCM at low-p_{T} or the higher p_{T} reach of calorimeters.
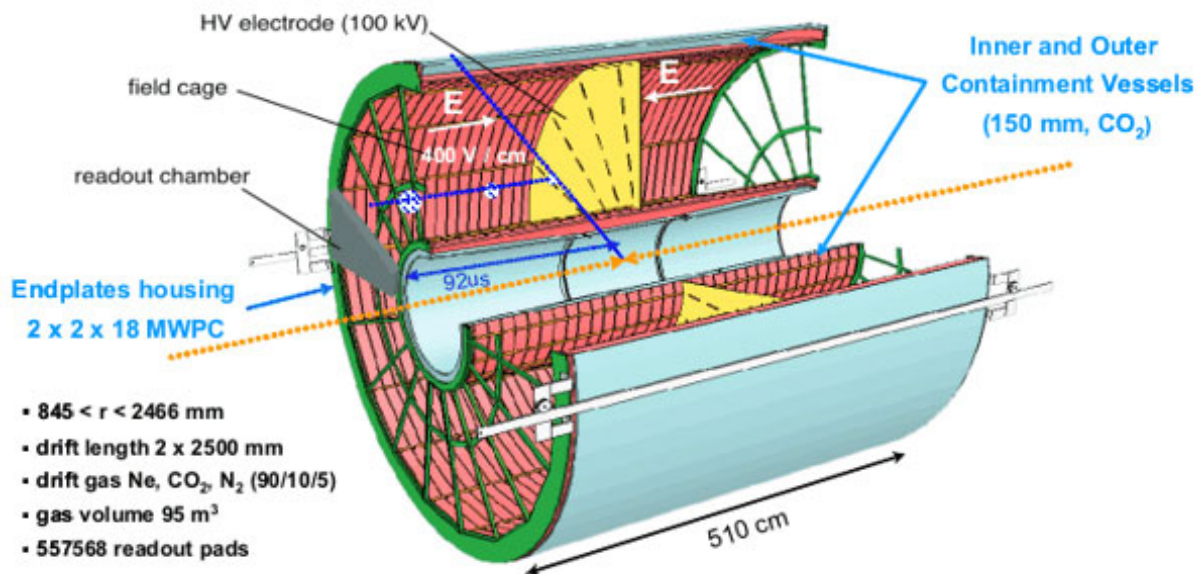
Figure 2.10: TPC overview [50]

2.3.5 V0 detector

The V0 system consists of two plastic scintillator arrays with read out via optional fibers (V0-A and V0-C) [51]. The V0-A and V0-C are located in $2.8 < \eta < 5.1$ and $-3.7 < \eta < -1.7$, respectively. Each of the V0 arrays is segmented in four rings in the radial direction, and each ring is divided in eight sections in the azimuthal direction. The main functionality of the V0 system is to provide the luminosity, particle multiplicity, centrality and event plane direction in heavy-ion collisions. An additional function is to contribute to the monitor LHC beam conditions and to the rejection of asymmetric beam-gas events, although the modest timing performance of this detector (≈ 0.6 ns) does not yield precise vertex or event timing information.
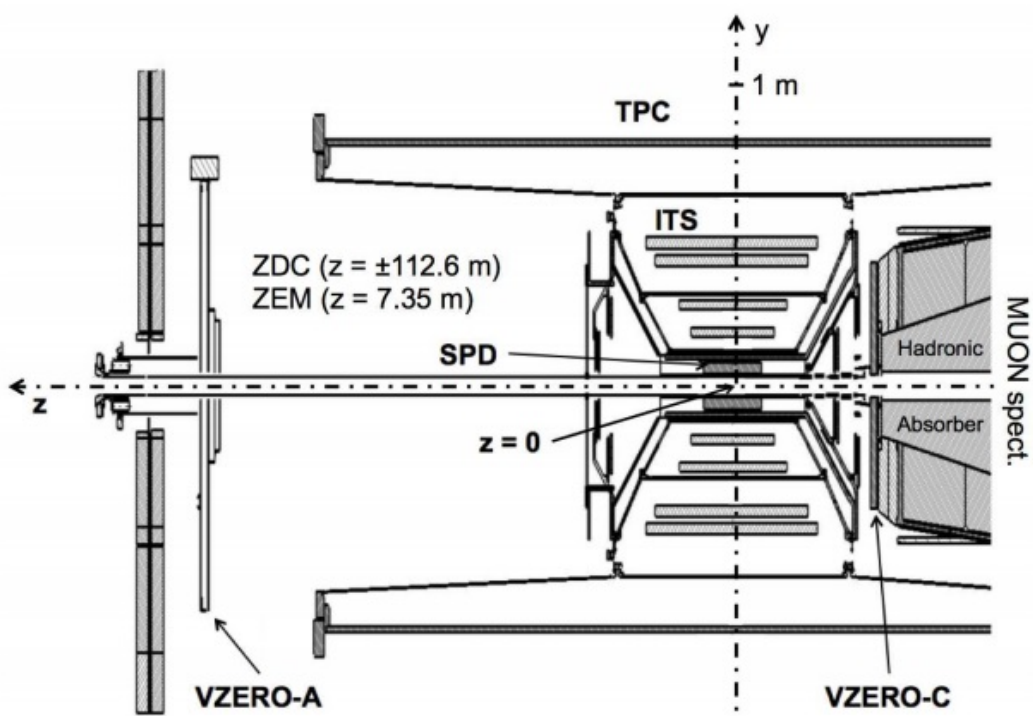
Figure 2.11: Position of the V0 detectors [52]

Chapter 3

Analysis

3.1 Run selection

This paper presents the π^0 and η meson measurements in p-Pb collisions at $\sqrt{s_{\mathrm{NN}}} = 5.02$ TeV collected in the beginning of 2013. Run periods are LHC13b, reconstruction pass3, and LHC13c, reconstruction pass2, the run list is shown in Appendix 1.

Data taking and detector condition may evolve with time. It is important to estimate the periods when the PHOS detector and data taking conditions are stable. In particular, the bad channel list may be not persistent because different modules of the detector may fail and be repaired afterwards. A way to monitor this long-term evolution is to study the dependence of basic physics observables versus time. In this paper, the good runs are selected by the following observables.

1. Average cluster energy

2. Average number of reconstructed clusters per event

3. Average number of cells per reconstructed cluster

These observables are delivered from the physics objects reconstructed in PHOS. The selection criteria for the clusters should be the same as the ones used in the physics analysis. The cluster energy is required to be above the minimum ionization energy $E_{\mathrm{cluster}} > 0.3$ GeV and the minimum number of cells in a cluster is 3 cells to reduce the contribution of non-photon clusters and noise. The observational results (Fig.3.1, 3.2 and 3.3) show the average cluster energy, the number of clusters per event and the number of cells per cluster, respectively. The average cluster energy is about 0.6 GeV for both modules. Average number of clusters per event is about 0.15 in Module2 and about 0.1 in Module4. This difference occurs from the number of stable cells. Average number of cells per cluster is about 7 cells in Module2 and about 6 cells in Module4, because Module2 is calibrated well as compared to Module4. Most runs are stable in each module but some runs have abnormal behavior. Run number 195596 is empty data because this run does not include PHOS. We can notice that run number 195346, 195532 and 195675 have abnormal behavior compared to other runs. Especially, run number 195346 has abnormal shape in the number of cells in cluster. These runs corresponding to about 2% of full statistics are excluded from this analysis because they may cause a negative effect for results.
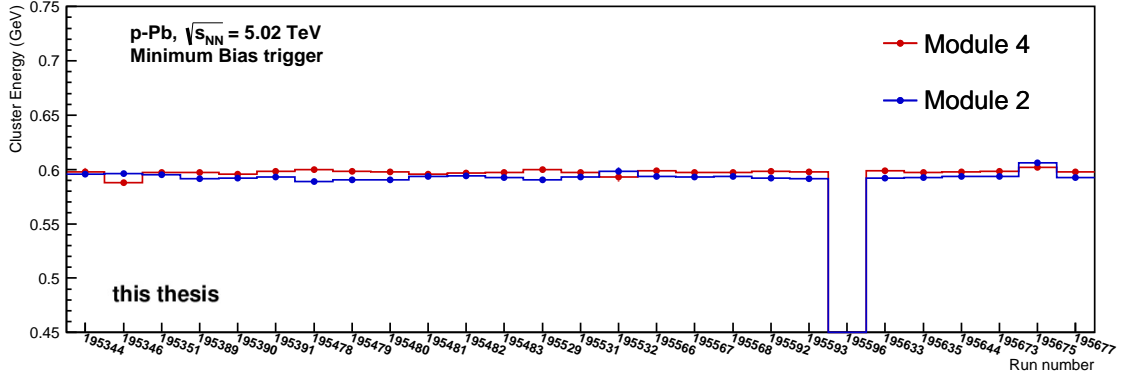
Figure 3.1: Average cluster energy
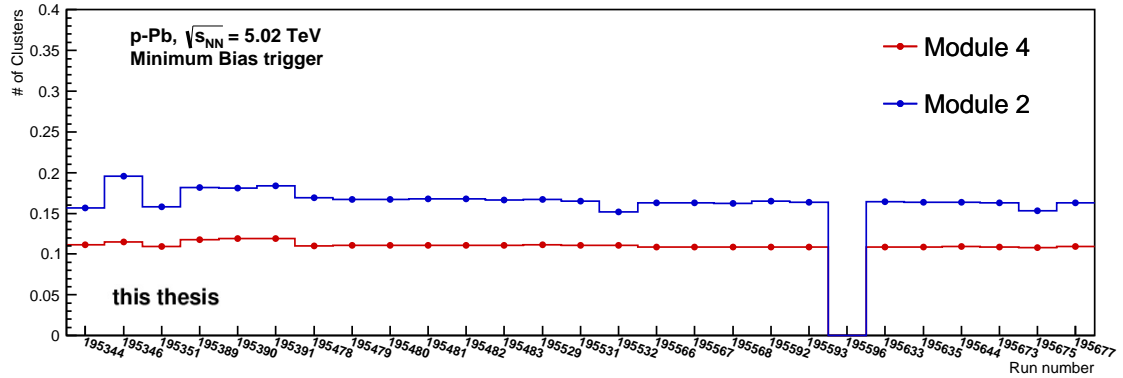
Figure 3.2: Average number of clusters per event
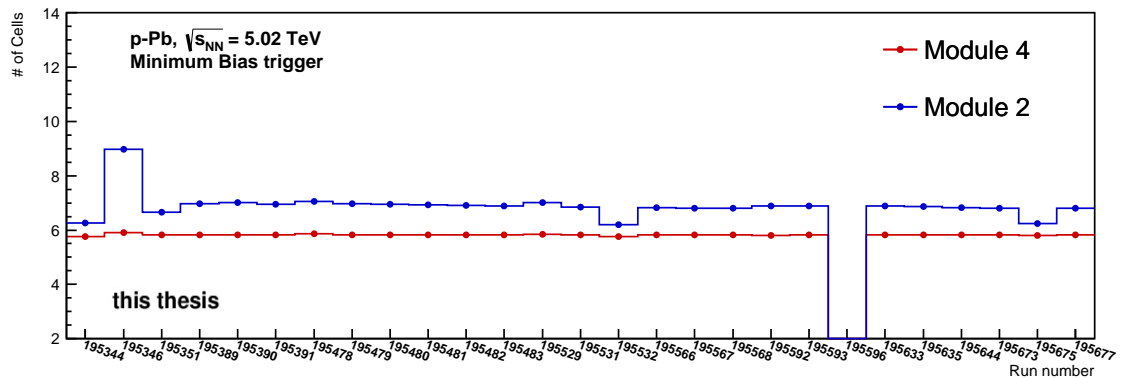
Figure 3.3: Average number of cells per cluster

39

In addition, the π^0 behaviors are checked in run-by-run. Here, the π^0 mesons are counted in bins within $\pm 3\sigma$ from the peak position at $p_\mathrm{T} > 1$ GeV/c after background subtraction. The background is estimated and subtracted with the event mixing technique. The details will be described in a later section. The invariant mass distributions per run are shown in Fig.3.4, 3.5, 3.6 and 3.7. Figure 3.4, 3.5 and 3.6 are mass distribution reconstructed within same module, and Fig.3.7 is sum of mass distribution reconstructed with only module4 and only module2. As it is obvious from Fig.3.5, we cannot find signal peak around the π^0 mass region due to a lot of hot channels in module3. We remove module3 from this analysis. The number of the π^0 per event, the peak position and peak width as a function of the run number are shown in Fig.3.8, 3.9 and 3.10. The above four runs have abnormal behaviors in the number of π^0, peak position and peak width.

3.2   Cluster selection

The number of analyzed events of the minimum bias triggered class is about 90 million after run selection, corresponding to an integrated luminosity $L_\mathrm{int} = 43.4 \pm 0.7\ \mu b^{-1}$. The integrated luminosity L_int is calculated as $N_\mathrm{pPb,MB}/\sigma_\mathrm{pPb,MB}$ where $N_\mathrm{pPb,MB}$ is the number of p-Pb collisions events passing the minimum bias trigger and $\sigma_\mathrm{pPb,MB}$ is the cross section of the V0 trigger, which was measured to be $2.09 \pm 3.5\%$ (syst) with the p-Pb Van Der Meer scan [53]. The ALICE minimum bias trigger requires a coincidence signal in both scintillator arrays of the V0-A and the V0-C, which is used by the standard physics selection with offline trigger AliVEvent::kINT7 for the event selection. The coincidence signal is required to reduce the contamination from single diffractive (SD) and electromagnetic events [54]. To select the primary collisions vertexes, the z-coordinate of each vertex (along the beam direction) is required to be within ± 10 cm ($|z_\mathrm{vtx}| < 10$ cm) with respect to the nominal interaction point, see Fig.3.11. The resulting event sample consists of mainly non-single diffractive (NSD) events [55], but there remains still SD and electromagnetic events. The remaining contamination is evaluated by the cocktail of MC models in earlier analyses [54].

PHOS generates electromagnetic showers by repeating the electron-positron pair creation, Compton scattering, bremsstrahlung and photoelectric effect of incident photons and electrons. The electromagnetic showers spreads out in longitudinal and transverse direction and deposits energy. Adjacent fired cells with energies above $E_\mathrm{cell}^\mathrm{min}$ were grouped together into clusters. The clusterization process started from cells with an energy exceeding E_seed. The choice of the values of E_seed and $E_\mathrm{cell}^\mathrm{min}$ was driven by the energy resolution and noise of the front-end electronics. PHOS choices $E_\mathrm{seed} = 50$ MeV and $E_\mathrm{cell}^\mathrm{min} = 15$ MeV.

To select photon candidate clusters, we apply the following cuts.

1. The low energy threshold is set at 0.3 GeV.
   This criterion is a natural choice in order to focus on electro-magnetic shower and therefore discard the signal from minimum ionizing particles (MIPs) which deposits energy in the range around 0.25 GeV.

2. The minimum number of cells in a cluster is 3 cells.
   This is selection for reduction of contributions of non-photon clusters and noise. To measure energy precisely, clusters which deposit maximum energy within 2.5 cm from a bad cell, are removed.

40
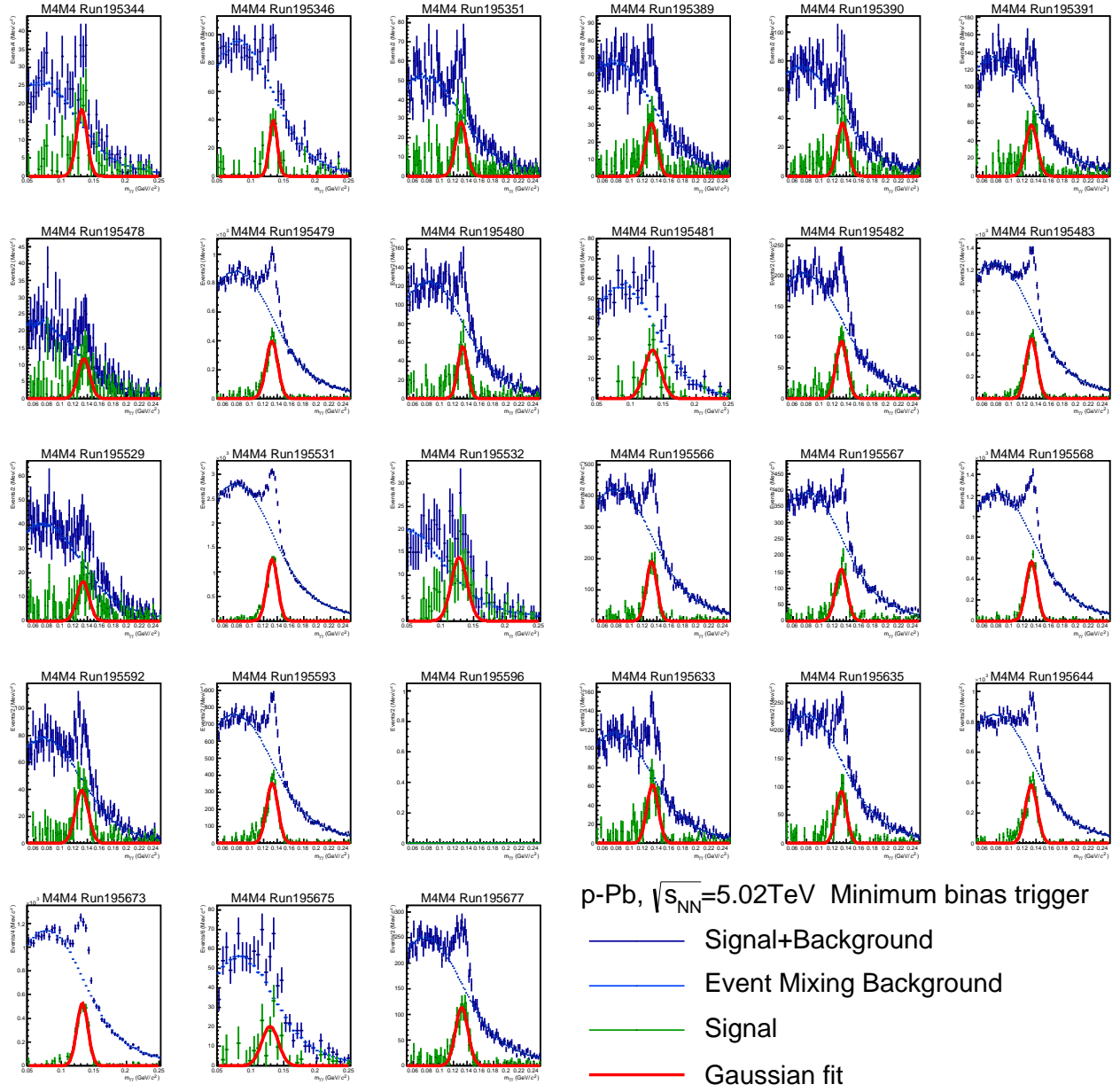
Figure 3.4: The invariant mass distribution of module4 in each run
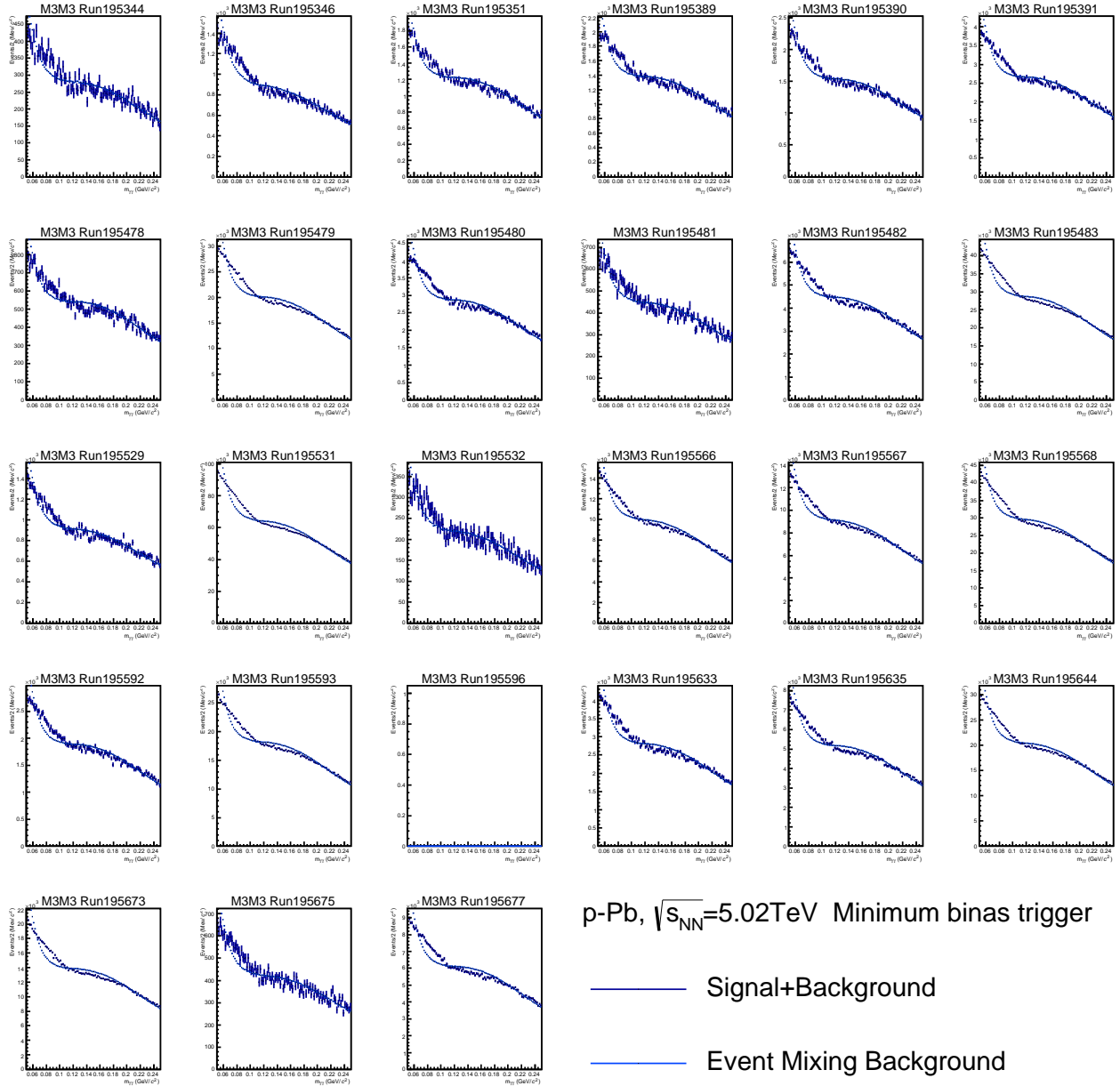
Figure 3.5: The invariant mass distribution of module3 in each run
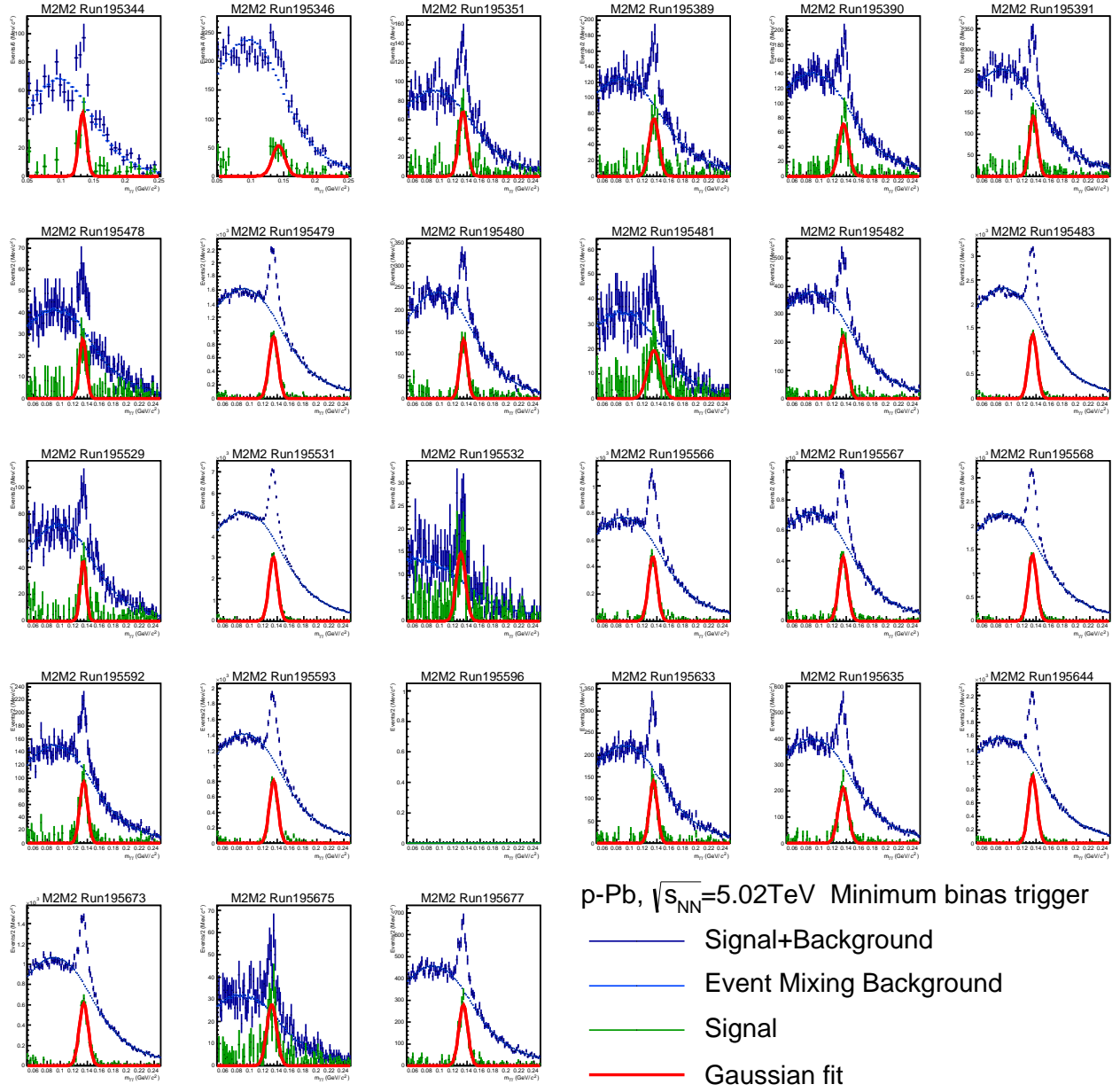
Figure 3.6: The invariant mass distribution of module2 in each run

43
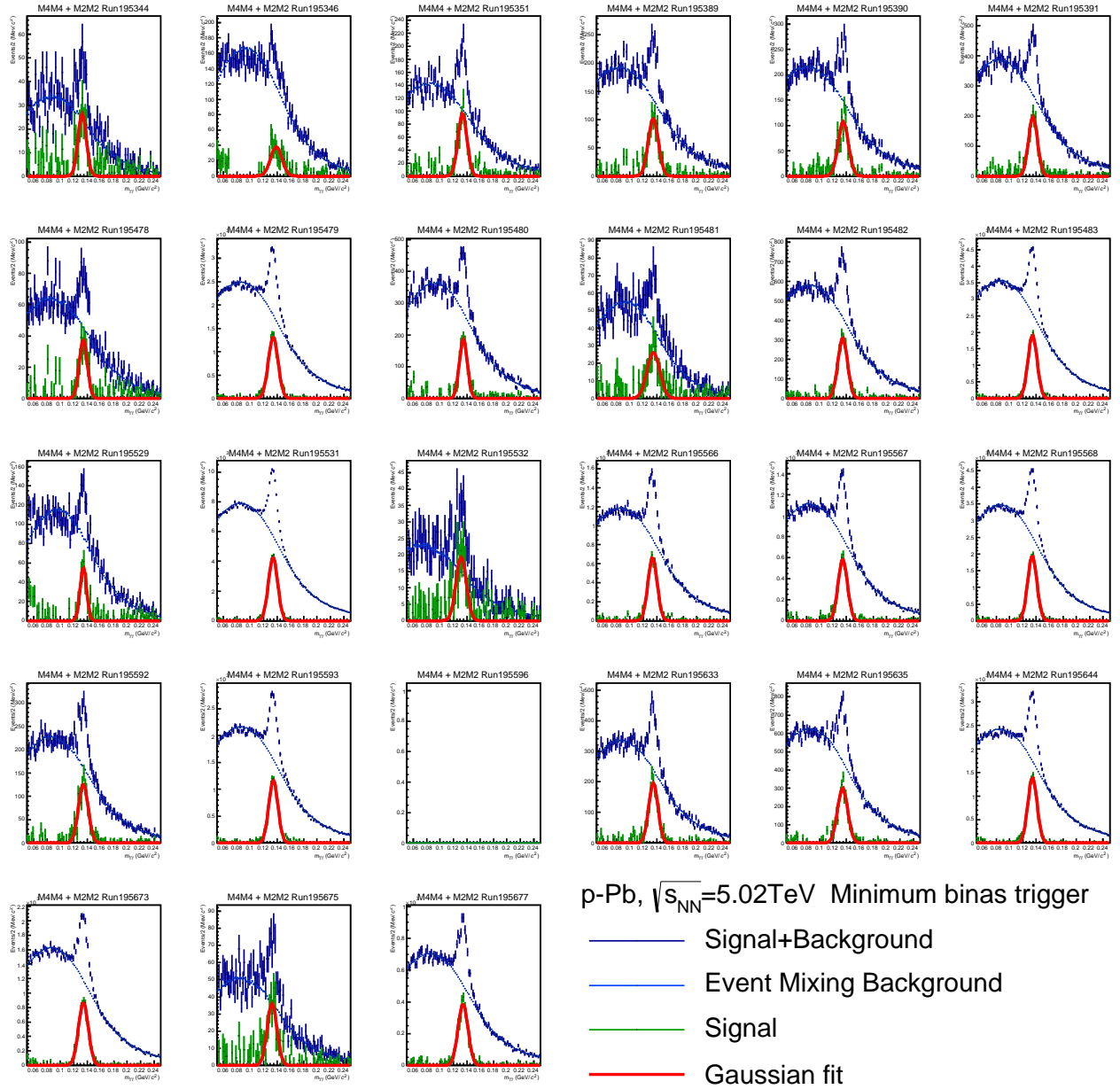
Figure 3.7: The invariant mass distribution of module4 and module2 in each run

44
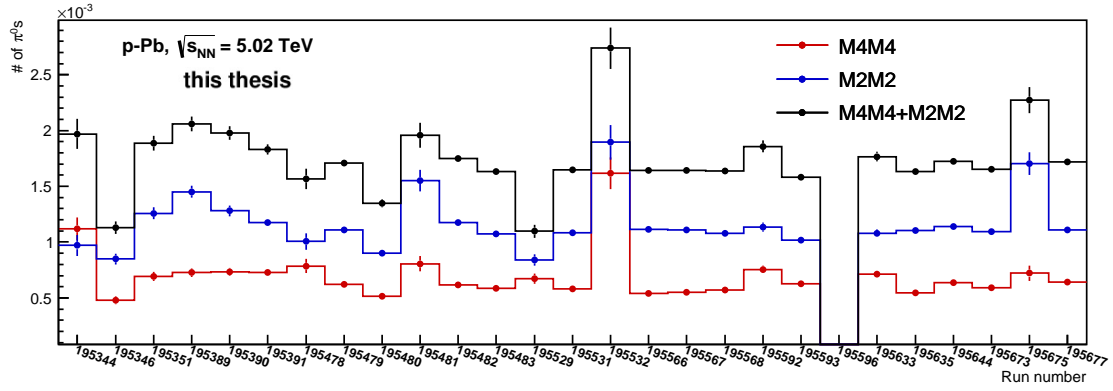
Figure 3.8: The number of the neutral π mesons per event vs. run
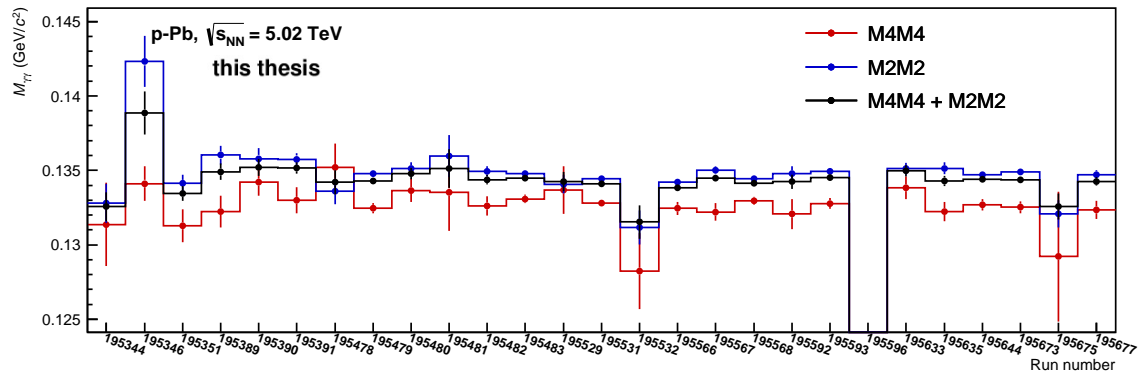
Figure 3.9: The neutral π mesons peak position vs. run
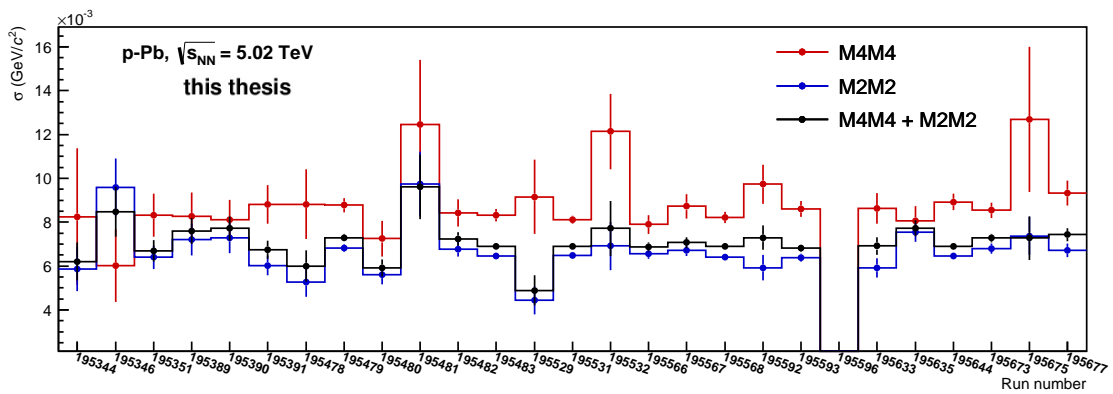
Figure 3.10: The neutral π mesons peak width vs. run

45
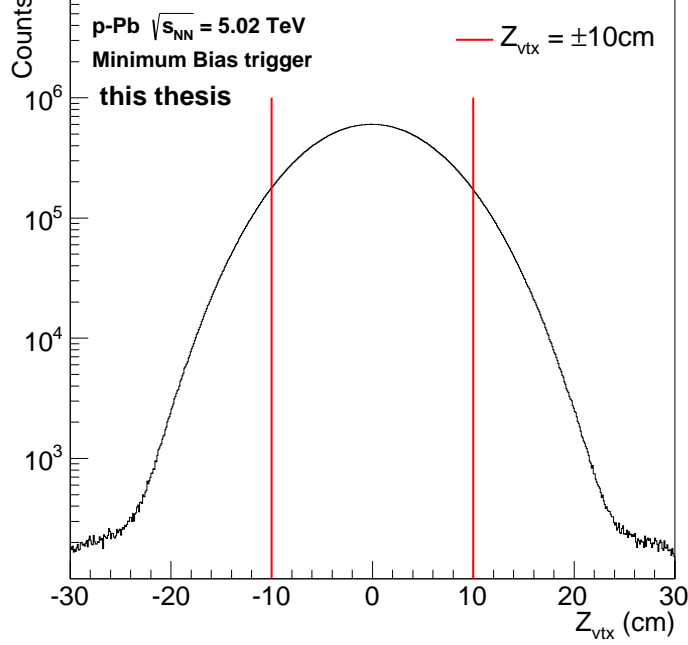
Figure 3.11: Vertex distribution in p-Pb collisions at $\sqrt{s_{\mathrm{NN}}} = 5.02$ TeV

3. The time-of-flight is applied within ± 100 ns ($|t_{\mathrm{cluster}}| < 100$ ns).

The TOF cut is effective to avoid clusters from next or previous bunch crossings. The TOF cut is applied within ± 100 ns because the bunch crossing time is 200 ns in p-Pb collisions at LHC-Run1 (Fig.3.12).

To avoid noisy and dead channels, I apply the good channels map (Fig.3.13) registered in Tender which supplies recalibration for data and MC simulation and modifying geometrical alignment. Green colored area indicates good cells and red colored area indicates bad (dead or noisy) cells. In addition, PHOS clusters having a center of gravity within 2.5 cm from a bad cell were removed for more precise measurement. The determination algorithm of basic bad channel is described in [56]. The Tender includes energy calibration and timing calibration. With applying Tender, the π^0 peak position comes close to the expected mass value and the peak width becomes smaller with increasing p_{T}. The comparison of peak position and width with applying Tender and without applying Tender is shown in Fig.3.14. In Fig.3.15, the small hump existing in right hand of main peak of time-of-flight distribution before applying timing calibration is vanished after applying timing calibration in Tender. These calibrations allow precise measurement for the π^0 yields.
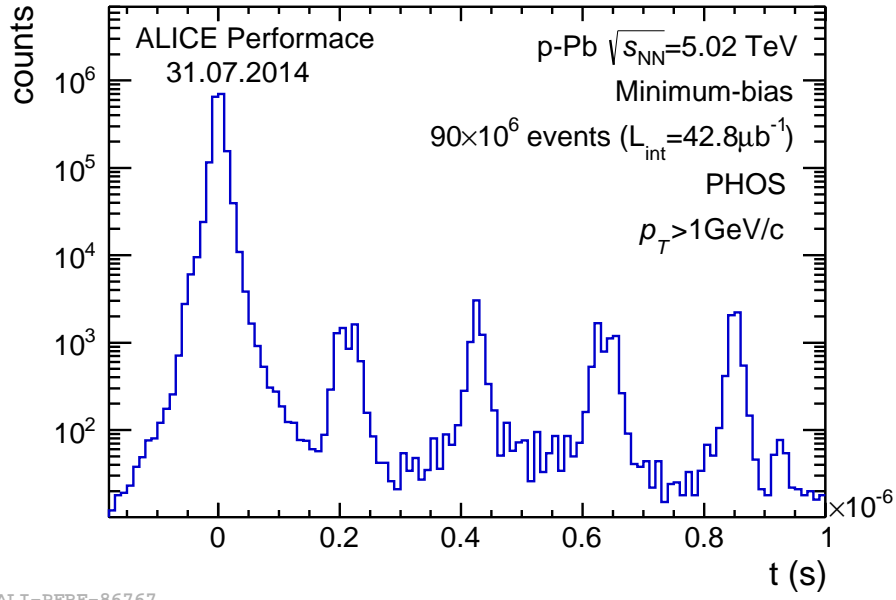
Figure 3.12: Timing spectrum of PHOS cluster in p-Pb collisions at $\sqrt{s_{\mathrm{NN}}} = 5.02$ TeV
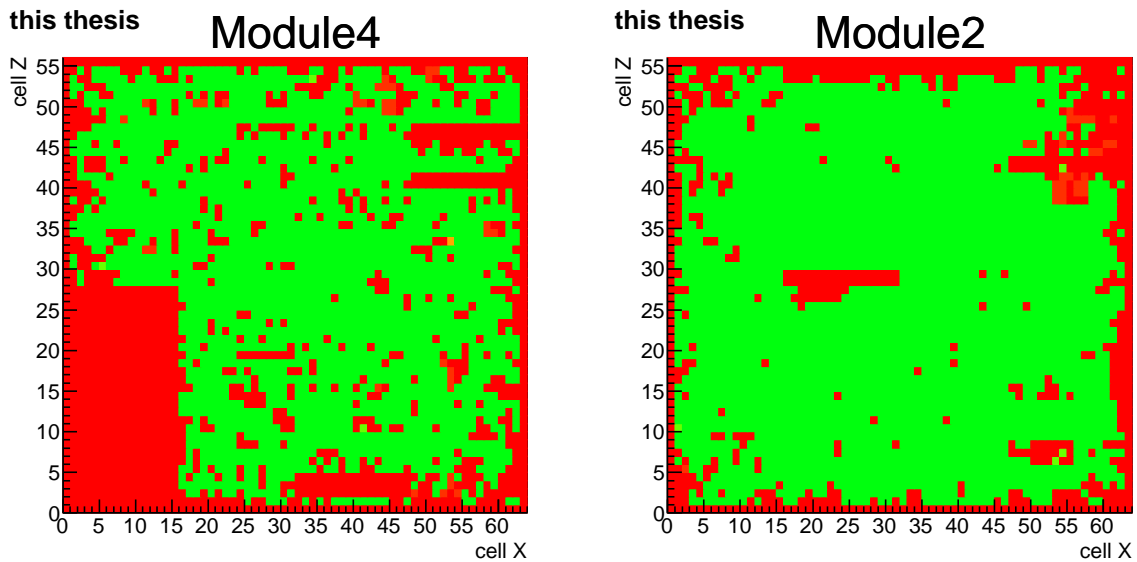
Figure 3.13: PHOS good channels map
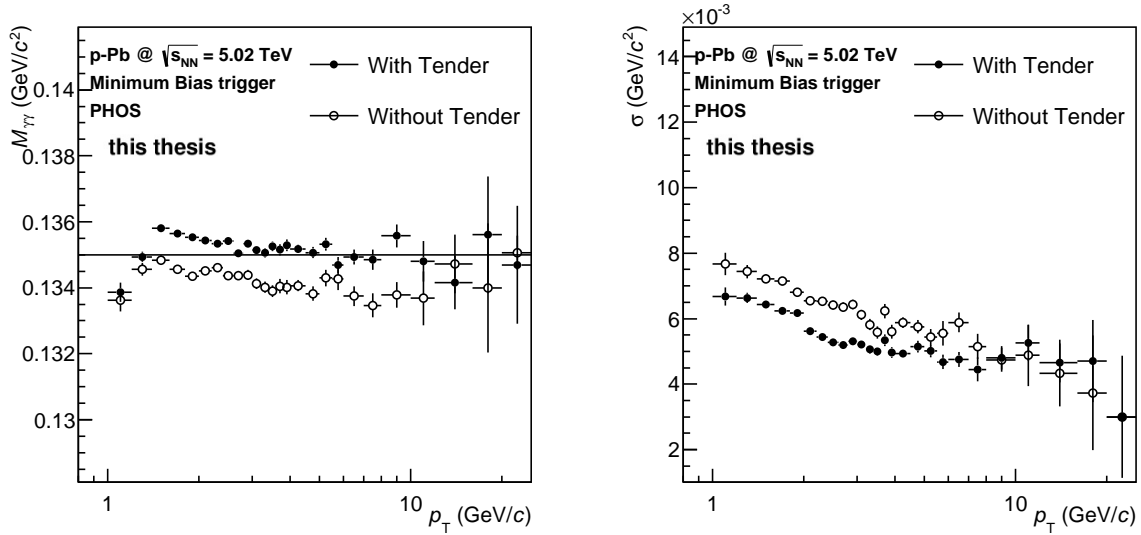
Figure 3.14: Comparison of π^0s peak position (left) and width (right) before and after applying Tender
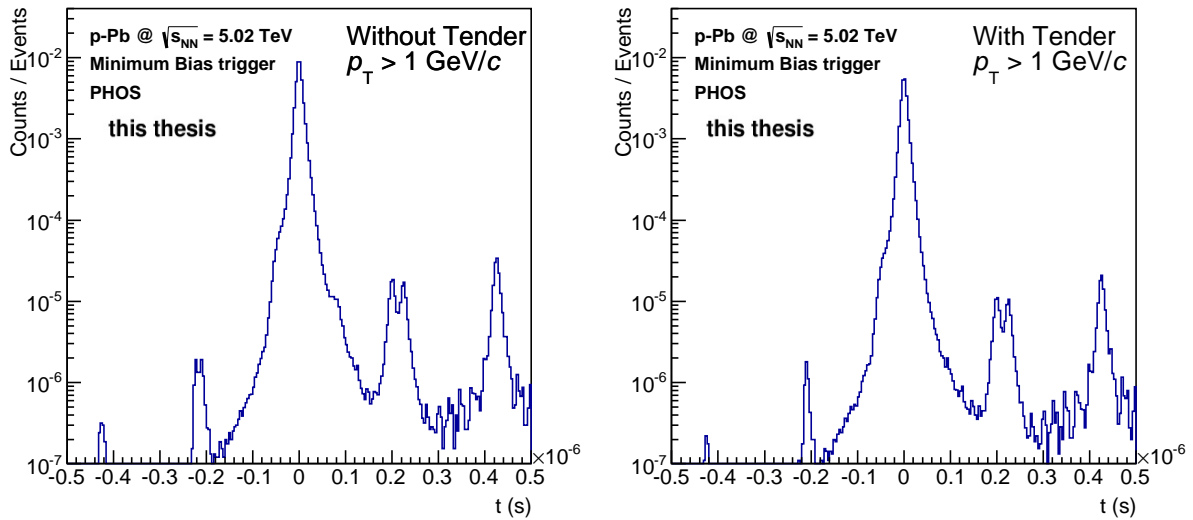
Figure 3.15: Comparison of time-of-flight distribution before (left) and after (right) applying Tender

3.3 Raw yield extraction

Raw spectrum of π^0 is measured in PHOS using invariant mass analysis with cluster pairs. To extract the π^0 signals and to count their yields from the two clusters invariant mass distribution, first the mixed event background is subtracted from same event mass distribution. In addition to same cluster criteria and z-vertex criteria, clusters detected in exact same cell are removed in the event mixing. The event mixing method reproduces well the combinatorial background. The mass distribution in event mixing method is reconstructed from pairs by taking one cluster from an event and the other cluster from another event. The mixed mass distribution has no peaks because cluster pairs don't have any relationship with each other. The combinatorial background estimated by the event mixing technique is normalized to the initial invariant mass distribution (where you are normalizing) and then subtracted. After background subtraction, the signal peak is fitted by the Gaussian function (Fig.3.16):

$$f(m) = A \cdot exp(\frac{-(m - M)^2}{2\sigma}) + c \tag{3.1}$$

where A, M, σ and c represent the height of the peak, the peak position, the peak width and constant free parameter, respectively. Raw yields are counted with numerical integral of the number of entries in the mass range from $M - 3\sigma$ to $M + 3\sigma$ in the Gaussian fitting parameters.

In addition, the invariant mass spectra are fitted by a Crystal Ball (Fig.3.16) and the raw yields are also counted in the same way, in the range from $M - 3\sigma$ to $M + 3\sigma$ in the Crystal Ball fitting parameters. The Gaussian does not properly reproduce the signal shape, see e.g. left wing of the π^0 peak. Therefore we try the Crystal Ball parameterization too:

$$f(m) = N \begin{cases} exp\left(-\frac{(m - \overline{m})^2}{2\sigma^2}\right), & \frac{m - \overline{m}}{\sigma} > -\alpha \\ A\left(B - \frac{m - \overline{m}}{\sigma}\right)^{-n}, & \frac{m - \overline{m}}{\sigma} \leqq -\alpha \end{cases} \tag{3.2}$$

where $A = \left(\frac{n}{|a|}\right)^n \cdot exp\left(-\frac{\alpha^2}{2}\right)$ and $B = \frac{n}{|\alpha|} - |\alpha|$. The Crystal Ball parameterization includes two more parameters (α, n), describing energy loss. The energy loss is expected by conversion electrons and energy leak in clustering. We look at the p_T dependence of these parameters (see Fig.3.17) and fix their values for the raw yield extraction:

$$\alpha = 1.56, \tag{3.3}$$
$$n = 3.28. \tag{3.4}$$

The parameters α and n for $p_T > 10$ GeV/c have large value with large errors and thus are excluded from the determination.

We estimate the signal description for the background normalization and subtraction by comparing raw yields with two assumptions about the signal shape, the Gaussian and the Crystal Ball [57]. The raw yields are calculated with bin counts of the histogram and analytical yield calculation in the two assumptions. Ratio of the raw yields to their average is shown in the left plot of Fig.3.18.
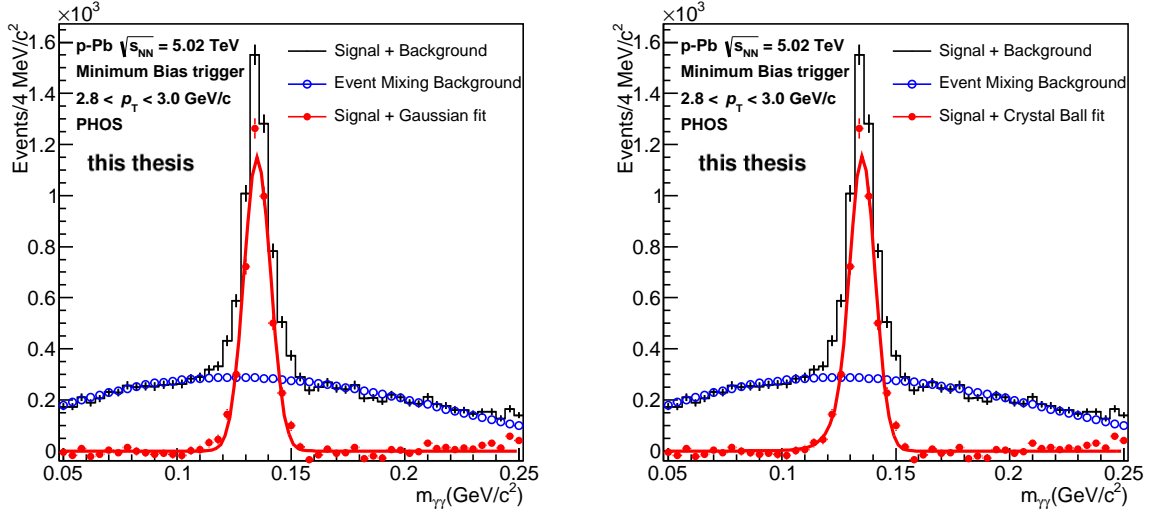
Figure 3.16: The π^0 mass peak with the Gaussian fit (left) and the Crystal Ball fit (right)
Black solid line represents the signal peak and the background. Blue open circle indicates the
event mixing background scaled by the same to mix mass ratio. Red filled circle is the signal peak
after subtracting the background.
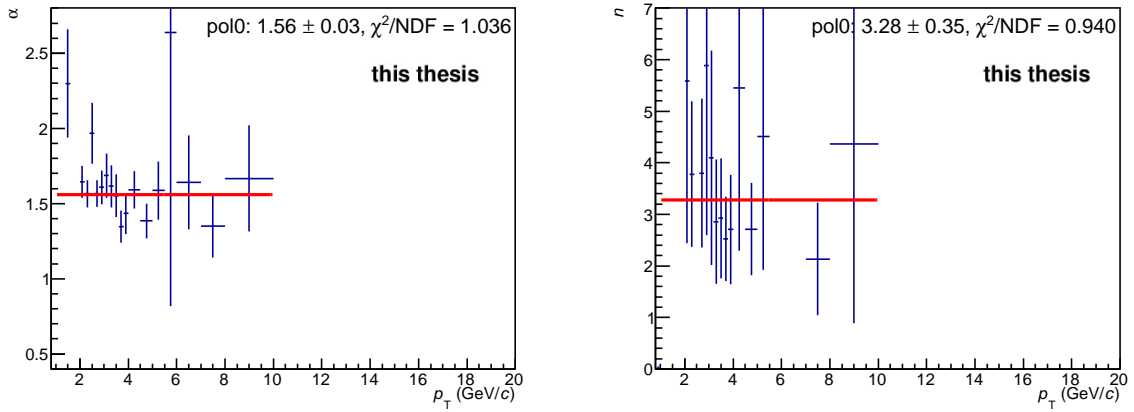
Figure 3.17: Parameters α and n in Crystal Ball fit

The yield calculated with analytical yield calculation of the Crystal Ball is larger than one calculated with analytical yield calculation of the Gaussian. However, this difference becomes smaller in comparing efficiency corrected yields, see the right plot of Fig.3.18. The efficiency is calculated in the same way, same peak assumption, as the data. The difference between yields calculated with integral of the histogram is smaller than one in the analytical yield calculation. This means that actual shape of the peak is intermediate between the Gaussian and the Crystal Ball. We use the Gaussian function in yield calculation, and two these extremes to calculate systematic uncertainties of raw yield extraction.

The raw spectrum of the reconstructed π^0 obtained from the invariant mass analysis is shown
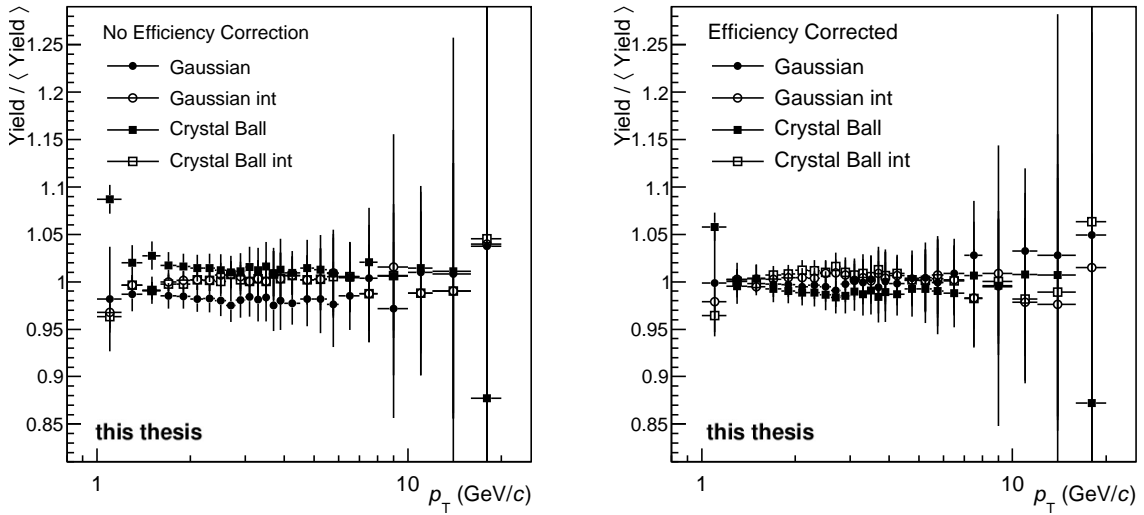
Figure 3.18: Comparison of the π^0 yield with different assumptions
Left figure represents ratio of the raw yield to their average and right figure presents ratio of the efficiency corrected yield to their average.

in Fig.3.19. As mentioned above, the invariant mass distributions are constructed from cluster pairs of the same event while the combinatorial background is estimated in event mixing method. The combinatorial background is normalized by a scaling parameter which is estimated by fitting the ratio of the same event mass distribution to the mixed mass distribution with the 2nd order polynomial in the mass range $0.07 - 0.22$ GeV/c^2. After background subtraction, the signal peak is fitted by the Gaussian function and the yields are counted by taking the numerical integral of the bins within $\pm 3\sigma$ from the peak position, for all p_T bins. The yield difference derived from different calculation assumptions is discussed later and is taken into account as a systematic uncertainty.
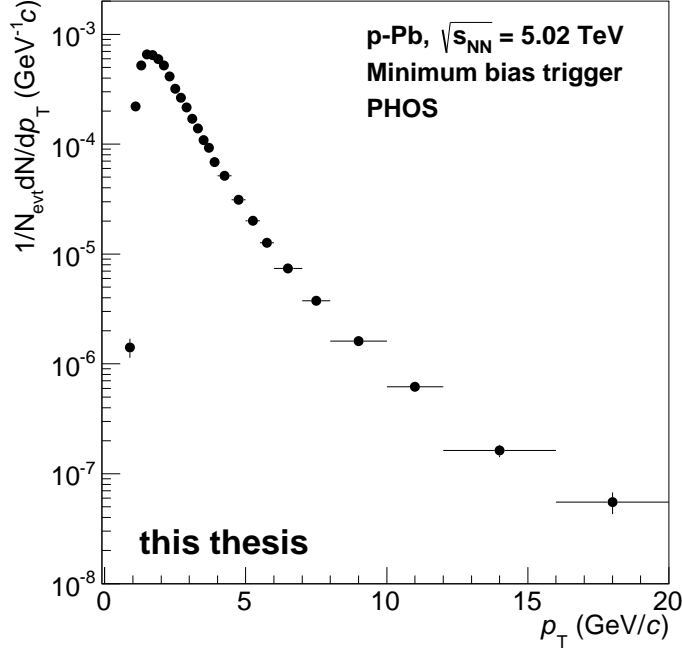
Figure 3.19: π^0 raw spectrum in p-Pb collisions at $\sqrt{s_{NN}} = 5.02$ TeV

3.4 Photon and meson reconstruction in EMCal

EMCal generates electromagnetic showers in response to incident photons and electrons, like the PHOS detector. Detail is described in Ref. [59]. The corresponding thresholds for EMCal is E_{seed} = 500 MeV and $E_{\text{cell}}^{\min} = 100$ MeV. The minimum number of cells in a cluster is set to two to reduce contributions of non-photon clusters and noise and the low energy threshold is set to 0.7 GeV to discard signals from MIPs and hadron showers. EMCal requires further photon identification to obtain more pure photon clusters by the cluster shape parameter λ_0^2 which is the principal eigen value of the cluster covariance matrix $\lambda_0^2 = (\sigma_{\eta\eta} + \sigma_{\phi\phi})/2 + \sqrt{(\sigma_{\eta\eta-\sigma_{\phi\phi}})^2/4 + \sigma_{\eta\phi}^2}$, where $\sigma_{ij} = \langle ij \rangle - \langle i \rangle \langle j \rangle$ (i, $j = \eta$ or ϕ) is the second moment of the cluster covariance matrix along the axes η, ϕ and $\langle i, j \rangle$ is the first moment weighted with the cell energy logarithm [63]. Photon clusters in EMCal were defined by the cluster axial symmetry cut $0.1 < \lambda_0^2 < 0.5$. Cluster timing cut, is applied in order to avoid clusters from next and previous collisions. In the EMCal the cell time of the leading cell of the cluster have to be within $|t| < 50$ ns of the collision time.

The π^0 and η meson are reconstructed by $\gamma\gamma$ pair candidates and calculated their invariant mass in transverse momentum bin. The invariant mass distribution measured in EMCal is shown in Fig.3.20 and Fig.3.21 for π^0 and η meson, respectively. The π^0 and η meson raw yields are extracted from background subtracted invariant mass. The background subtracted signal is fitted to reconstruct the mass position and width of the π^0 and η meson. The fit function consisted

of a Gaussian function convoluted with an exponential low-energy tail to account for electron bremsstrahlung [64] and an additional linear function to consider a possible remaining background. The reconstructed π^0 and η meson peak and width as a function of p_T compared to GEANT3 MC simulations are shown in Fig.3.22 and 3.23. The energy of the EMCal is not calibrated to the π^0 mass, but the cluster energy in MC is shifted such that it corresponds with the reconstructed mass in data. The systematic difference of about 3.0 % (6.0 %) that is observed for the EMCal π^0 (η) analysis, is taken into account in the systematic uncertainties.

The π^0 and η meson raw yields are obtained by integrating the background subtracted invariant mass distribution around the reconstructed meson mass determined by the fit function. The integrating ranges are selected according to the resolution of respective methods. The mass ranges from $M_{\pi^0} - 0.032$ GeV/c^2 to $M_{\pi^0} + 0.022$ GeV/c^2 and from $M_{\eta} - 0.060$ GeV/c^2 to $M_{\eta} + 0.050$ GeV/c^2 are used.

Correction for secondary π^0s from weak decays or hadronic interactions, mainly K_s^0, is taken into account. This correction is of the order of 2.5 % at low-p_T and 2 % at high-p_T.

3.5 Photon and meson reconstruction in PCM and PCM-Dalitz

PCM and PCM-Dalitz reconstructed photons converted to e^+e^- pairs in the material of the ITS and TPC [60,61]. To ensure good track quality, following cuts are applied to the charged tracks. A minimum track p_T is more than 0.05 GeV/c with kink daughters cut. The ratio of reconstructed TPC clusters to all findable clusters requires to be at least 0.6 for both tracks. A secondary vertex finding algorithm (V^0 finder) [62] is used for building candidates from charged track pairs with opposite sign (V^0s). The main contributions to the V^0 candidates are K_s^0, Λ, $\bar{\Lambda}$ and γ. In order to extract photons from V^0 candidates, electron selection and pion rejection cuts on the track level are performed. Therefore, the specific energy loss dE/dx in the TPC is used. The TPC dE/dx distribution in p-Pb collisions is shown in Fig.3.24. For the $\gamma\gamma$ decay channel only tracks with a dE/dx lying in a band of $[-3\sigma; +5\sigma]$ around the electron hypothesis and above the average pion dE/dx are considered for the further analysis. The cut on the pion band is only applied for tracks with a momentum larger than 0.4 GeV/c. For the Dalitz decay channel, an electron selection of $[-4\sigma; +5\sigma]$ and a pion rejection of 2σ (0.5σ) above the pion hypothesis for tracks with 0.5 GeV/c $< p <$ 3.5 GeV/c ($p >$ 3.5 GeV/c) is performed. The reconstructed conversion point had to lie in the fiducial volume restricted by a maximal conversion radius of 180 cm. When reconstructing neutral mesons via the $\gamma\gamma$ decay channel, an additional cut on a minimal conversion radius of 5 cm is applied to prevent contamination from Dalitz decays. Furthermore, the charged tracks as the reconstructed photon candidates are required to be in the pseudorapidity range of $|\eta_{\text{lab}}| <$ 0.9.

Primary electrons and positrons from the virtual photon (γ^*) in the Dalitz decay are reconstructed with both the ITS and the TPC. Additional cuts are applied in order to ensure their track quality. Tracks are required to cross at least 70 TPC pad rows and the ratio between found and expected (according to the geometry of the track) TPC crossed row pads has to be a larger than 0.8. The χ^2/NDF which determines the quality of the fit between the track and the TPC (ITS) clusters are required to be less than 4 (36). The $\chi^2_{\text{TPC−ITS}}$ defined in [58] which is used to improve the purity of the primary tracks at high-p_T is restricted to be smaller than 36. To ensure that the selected tracks come from the primary vertex, their distance of closest approach to the main vertex in lon-

gitudinal direction (DCA$_z$) has to be smaller than 2 cm. In addition, in order to reject e^+e^- pairs from photon conversions within the pipe, only tracks with at least one hit in any layer of the SPD are accepted. Electron identification is performed using the TPC dE/dx. Electrons are accepted within $[-4\sigma; +5\sigma]$ around the electron hypothesis. For the pion rejection at intermediate-p_T the same cut as described for the conversion electron tracks is used while at high-p_T the cut is not applied to maximize the efficiency. Only primary electron candidates with a minimum p_T of 125 GeV/c are taken into account.

In the Dalitz decay channel, the pion contamination in the primary electron sample is reduced by cutting on the γ^* invariant mass, $M_{e^+e^-} < 0.015$ GeV/c^2 at $p_T \leq 1$ GeV/c and $M_{e^+e^-} < 0.035$ GeV/c^2 at $p_T > 1$ GeV/c, exploiting that most of the pairs from π^0 Dalitz decays have a very small invariant mass, as given by the Kroll-Wada formula [65].

The π^0 and η meson are reconstructed by $\gamma\gamma$ or $\gamma^*\gamma$ pair candidates and calculated their invariant mass in transverse momentum bin. Their raw yields are extracted signal from background subtracted mass distribution. The π^0 invariant mass distributions by PCM and PCM-Dalitz measurements are shown in Fig.3.20 and η meson invariant mass distributions by PCM measurement are shown in Fig.3.21. The combinatorial background which is estimated by event mixing technique is scaled to match the background outside the main signal region, and subtracted. The signal is fitted to π^0 and η meson mass peak position and width. The PCM and PCM-Dalitz measurements use fit function with Gaussian function convoluted with an exponential low-energy tail to take into consideration of electron bremsstrahlung [64] and additional linear function to consider a possible remaining background. Mass peak position and width for reconstructed π^0 and η meson are compared to MC simulations are shown in Fig.3.22 and 3.23.

The raw yields are obtained by integrating bin entries of the background subtracted $\gamma\gamma$ or $\gamma^*\gamma$ invariant mass distribution around the mass peak which is determined by the fit function. The integration ranges from $M_{\pi^0} - 0.035$ GeV/c^2 to $M_{\pi^0} + 0.010$ GeV/c^2 and from $M_\eta - 0.048$ GeV/c^2 to $M_\eta + 0.22$ GeV/c^2 are used in both PCM and PCM-Dalitz.

Secondary π^0 correction from weak decays or hadronic interactions are estimated and subtracted. This correction is of the order of 7 % at low-p_T and 1 % at high-p_T for PCM and negligible for PCM-Dalitz. The PCM analysis is affected by pile-up due to the relatively large drift time of the TPC, and the correction is applied as described in [2]. (The pile-up contribution is negligible for the other methods.) The PCM-Dalitz analysis used MC simulations to apply an additional correction for the remaining contamination ~ 2.5 % of the $\pi^0 \to \gamma\gamma$ in the $\pi^0 \to \gamma^*\gamma$ decay channel.
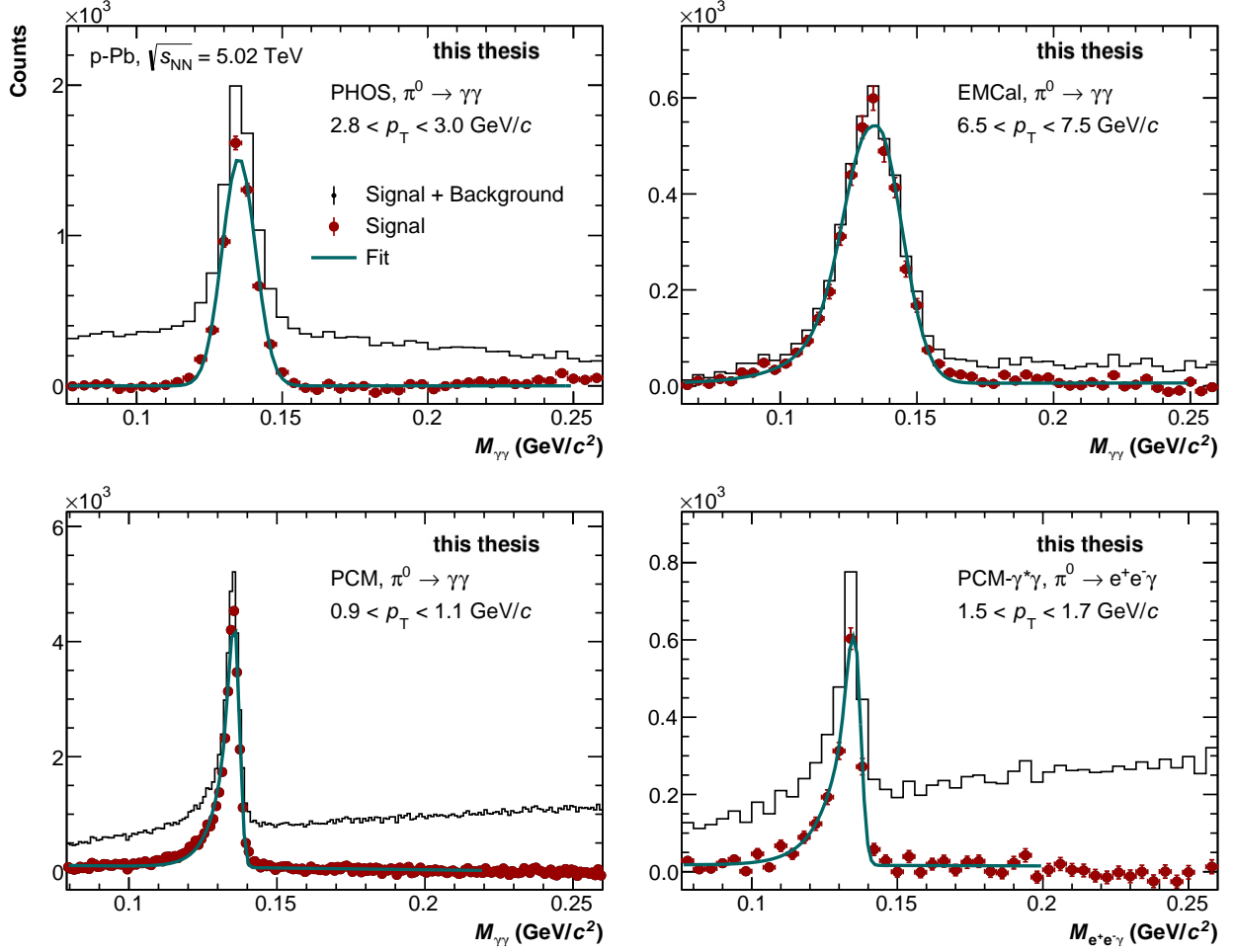
Figure 3.20: π^0 invariant mass distribution for PHOS, EMCal, PCM and PCM-Dalitz
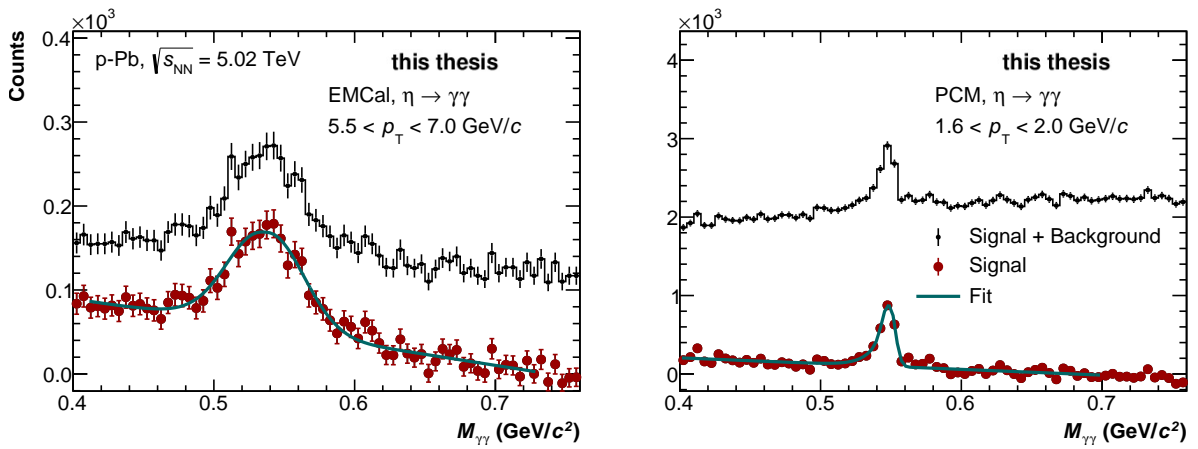
Figure 3.21: η invariant mass distribution for EMCal and PCM
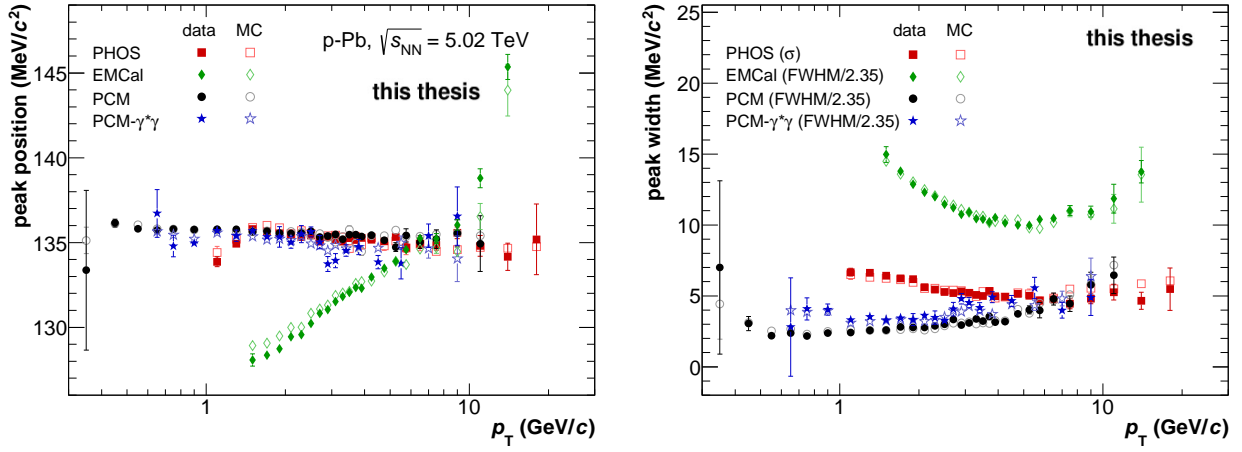
Figure 3.22: π^0 mass (left) and width (right) as a function of p_T for PHOS, EMCal, PCM and PCM-Dalitz
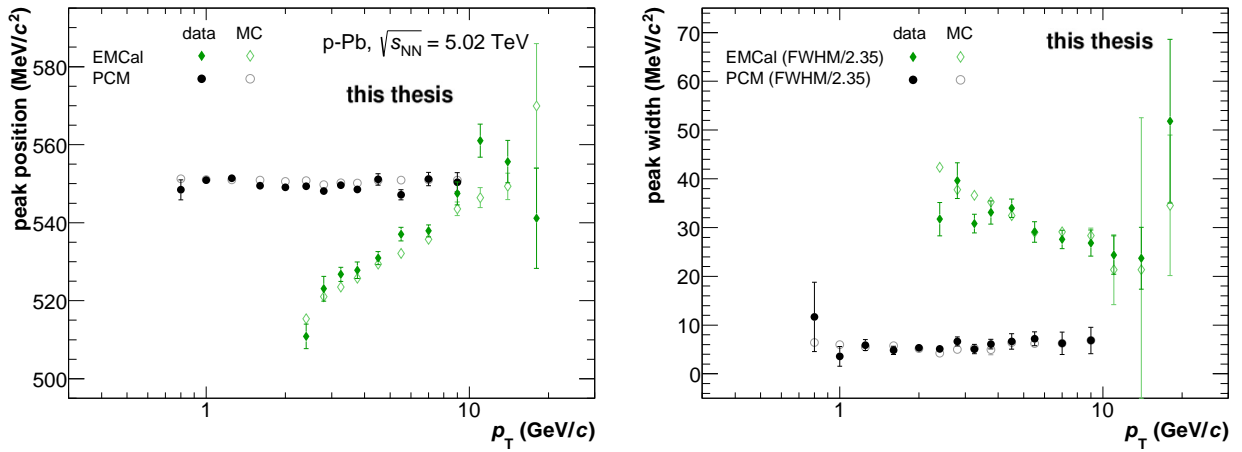
Figure 3.23: η mass (left) and width (right) as a function of p_T for EMCal and PCM
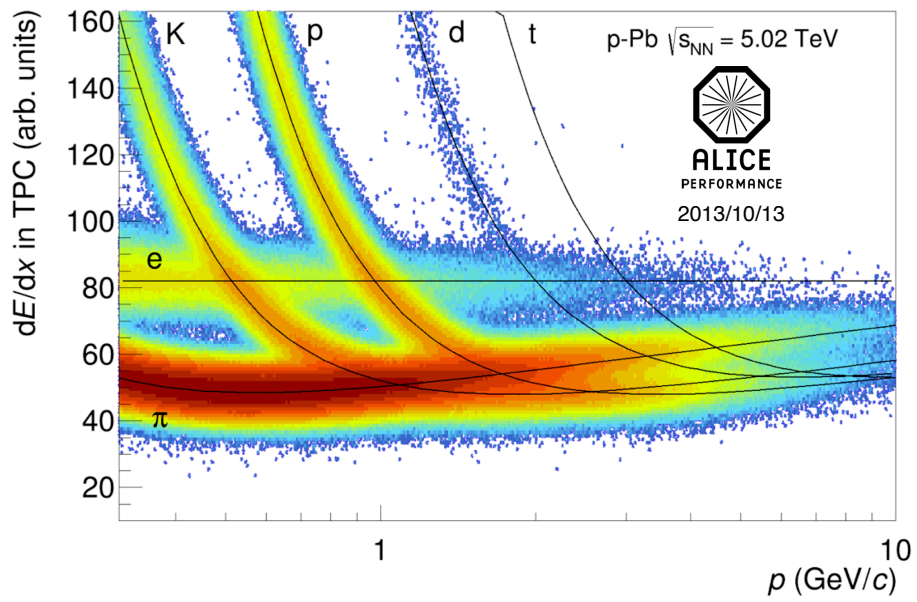
Figure 3.24: TPC dE/dx distribution in p-Pb collisions at $\sqrt{s_{\mathrm{NN}}} = 5.02$ TeV

Chapter 4

Efficiency calculation

4.1 Acceptances and reconstruction efficiencies

The raw spectrum is obtained from invariant mass analysis. It is corrected with PHOS acceptance, finite geometrical coverage and the probability of loosing π^0s due to photon conversion in the medium, and the efficiency of the number of extracted π^0s from the invariant mass analysis of cluster pairs. All these corrections, being applied to the raw spectrum, should result in the π^0s production spectrum which is the final goal of the measurements. The acceptance and reconstruction efficiency are defined by the following formulae.

$$\varepsilon_{\text{Acc}} = \frac{\pi^0 \text{ generated in PHOS acceptance}(|y| < 0.13, \ 260° < \phi < 320°)}{\text{Generated } \pi^0(|y| < 0.5, \ 0° < \phi < 360°)} \tag{4.1}$$

$$\varepsilon_{\text{Rec}} = \frac{\pi^0 \text{ reconstructed in PHOS}}{\pi^0 \text{ generated in PHOS acceptance}(|y| < 0.13, \ 260° < \phi < 320°)} \tag{4.2}$$

$$\varepsilon_{\text{Acc}\times\text{Rec}} = \varepsilon_{\text{Acc}} \times \varepsilon_{\text{Rec}} \tag{4.3}$$

The acceptances and reconstruction efficiencies are calculated with the ALICE official Monte Carlo productions. The productions are LHC13b2_efix which is DPMJET [66] minimum bias generator anchored to LHC13b and LHC13c, and LHC13e7 which is HIJING [67] generator with added π^0s generated per event in the p_{T} range 1 to 30 GeV/c in uniform distributions over azimuthal angle $260° < \phi < 320°$ and rapidity range $|y| < 0.13$. The $y - \phi$ distributions for the π^0s from the underlying events generated by HIJING and for the added π^0s are shown in the top plots of Fig.4.1. The p_{T} distribution within $|y| < 0.5$ and full azimuthal of underlying events π^0s is shown in the left bottom plot of Fig.4.1 and the p_{T} distribution of the added π^0s ($260° < \phi < 320°$ and $|y| < 0.13$) is shown in the right bottom plot of Fig.4.1. It can be seen that separates the added signals from the underlying events in LHC13e7. The DPMJET minimum bias event generator is suitable for the efficiency calculation at low-p_{T}. However the π^0 spectrum in this generator vanishes at high-p_{T} due to the lack of available statistics. So, HIJING generator with added π^0s becomes important, and the efficiencies are calculated with the HIJING plus added signals generator at $p_{\text{T}} > 7$ GeV/c. In addition, the added π^0s are weighted with a Tsallis function (Eq.6.1) in order to reproduce a
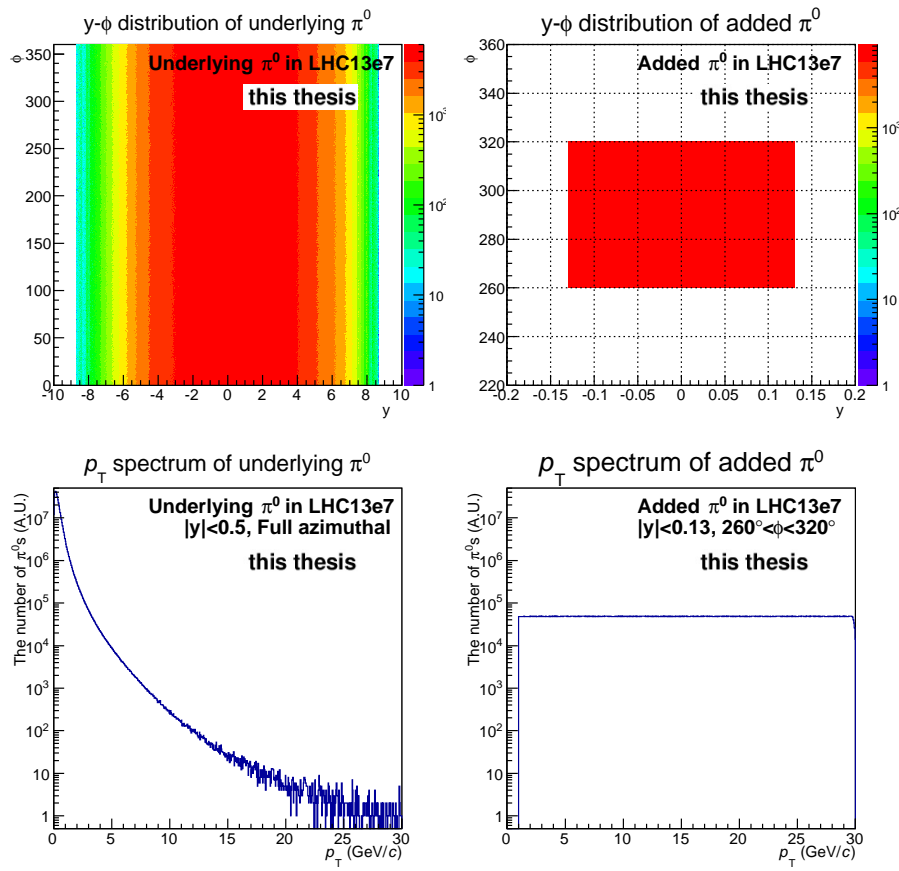
Figure 4.1: $y - \phi$ distribution and p_T spectrum of the π^0 of underlying events and added signals

realistic p_T spectrum (Fig.4.2). The parameters of the function have been defined by an iterative procedure, so as to better describe the realistic spectrum. The π^0 spectra with varying Tsallis parameter "n" are compared in Fig.4.3. Other parameters are fixed in this iteration. The ratio of the weighted generated π^0 spectrum to the final π^0 spectrum is flat with the χ^2/NDF of the zero order polynomial (constant function) fitting is minimum when parameter is n = 7.50. We have decided that this value of the parameter "n" is optimal and calculated the efficiency by weighting the flat distribution of the added π^0s with the corresponding Tsallis function. The mass (peak position) and the width of the π^0 in MC are compared with the corresponding quantities in real data (Fig.4.4). In these figures of Fig.4.4, DPMJET is used up to 7 GeV/c and added π^0 signals from LHC13e7 are used from 7 GeV/c. DPMJET is tuned with an energy calibration to reproduce the real PHOS response. The tuning method is described in a later section (section 5.4). The mass and width in MC are consistent with that in real data (Fig.4.4).
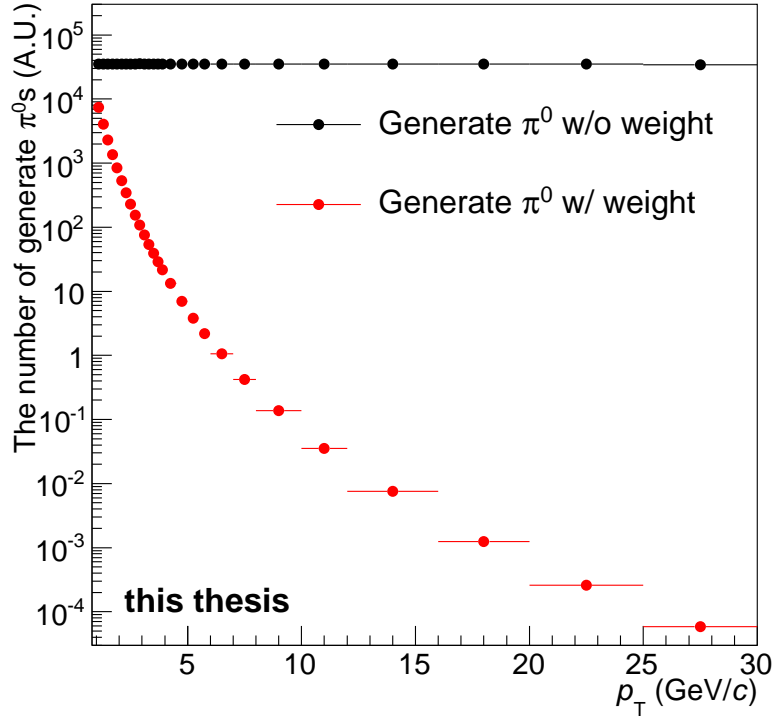
Figure 4.2: Generated π^0 spectrum with weight (red) and without weight (black)

The acceptances and reconstruction efficiencies are calculated independently by using DPMJET and added signals. The acceptance of added signals is obtained by the numerical calculation. After those independent calculations, efficiencies are merged into one efficiency. Figure 4.5 shows the acceptance and reconstruction efficiencies calculated by DPMJET and added signals, and the merged efficiency as well ($p_T < 7$ GeV/c: DPMJET, $p_T > 7$ GeV/c: added signals). The π^0 raw
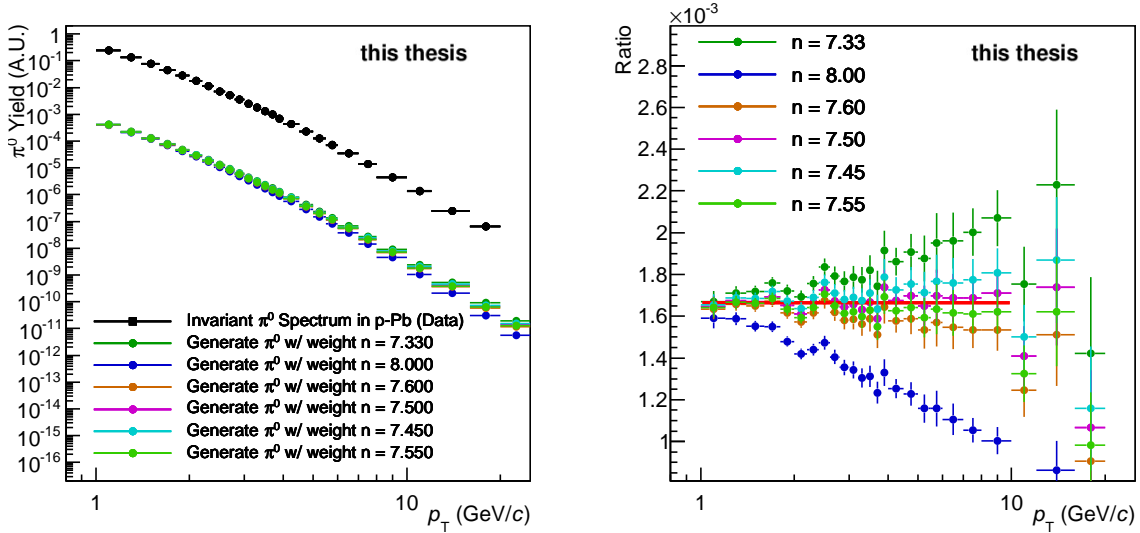
Figure 4.3: Final spectrum and generated spectrum with weight (added signals, left) and ratio of the generated spectrum to the final spectrum (right)
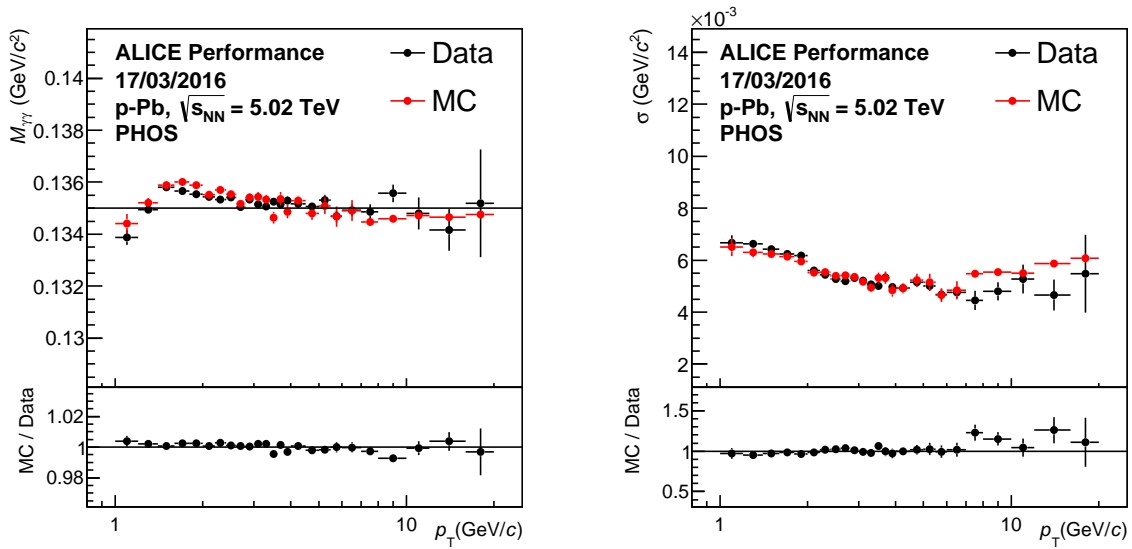
Figure 4.4: Comparison of π^0 mass (peak position, left) and width (right) between data and MC simulations

yield is converted to an invariant spectrum with using this efficiency.
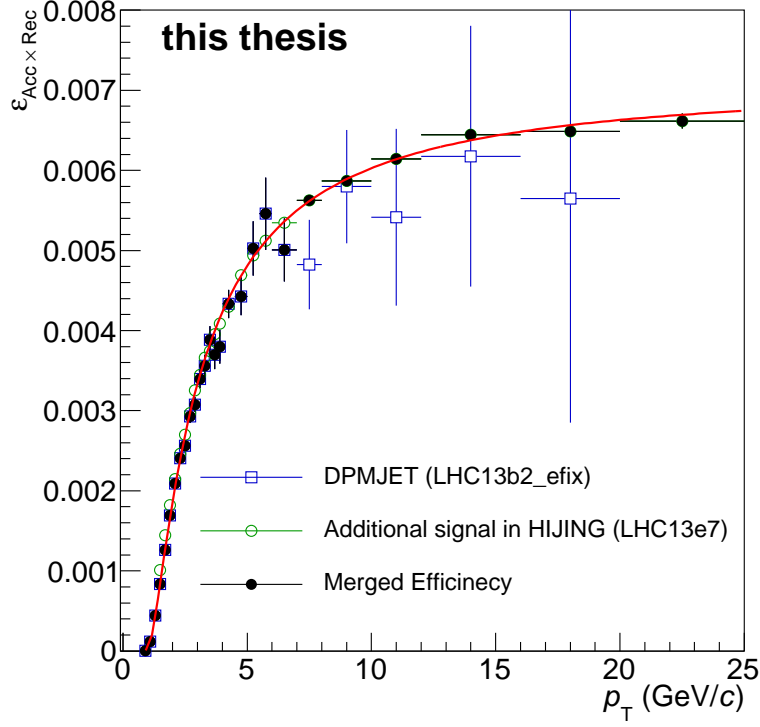
Figure 4.5: Acceptances and reconstruction efficiencies
Blue square shows the acceptance and reconstruction efficiencies calculated by DPMJET
(LHC13b2_efix) and green circle shows efficiencies calculated by additional signal in HIJING
(LHC13e7). Black marker shows merged efficiencies

4.2 Time-of-flight cut efficiency

The π^0 spectrum is corrected with the Time-Of-Flight (TOF) cut efficiency. The cluster timing
distribution in MC simulation does not reproduce data correctly. Therefore, TOF cut efficiency
$\varepsilon_{\mathrm{TOF}}$ is estimated via real data and is defined as below,

$$\varepsilon_{\mathrm{TOF}} = \frac{N_{\mathrm{one\ cluster}}}{N_{\mathrm{both\ clusters}}}, \tag{4.4}$$

where, $N_{\mathrm{one\ cluster}}$ is the π^0 spectrum if TOF cut is applied to at least one cluster and $N_{\mathrm{both\ clusters}}$
is the π^0 spectrum if TOF cut is applied to both clusters. Having $\varepsilon_{\mathrm{TOF}}$, the TOF cut efficiency

corrected yield is calculated following:

$$\text{TOF cut efficiency corrected yield} = \frac{\text{N}_{\text{both clusters}}}{\varepsilon_{\text{TOF}} \times \varepsilon_{\text{TOF}}}. \tag{4.5}$$

The ratio of the raw yields when TOF cut is applied to one cluster only or to both clusters and when no TOF cut is applied is shown in Fig.4.6. Both ratios have no p_{T} dependence.

The purity of TOF cut is used to estimate the probability whether a π^0 has been produced by
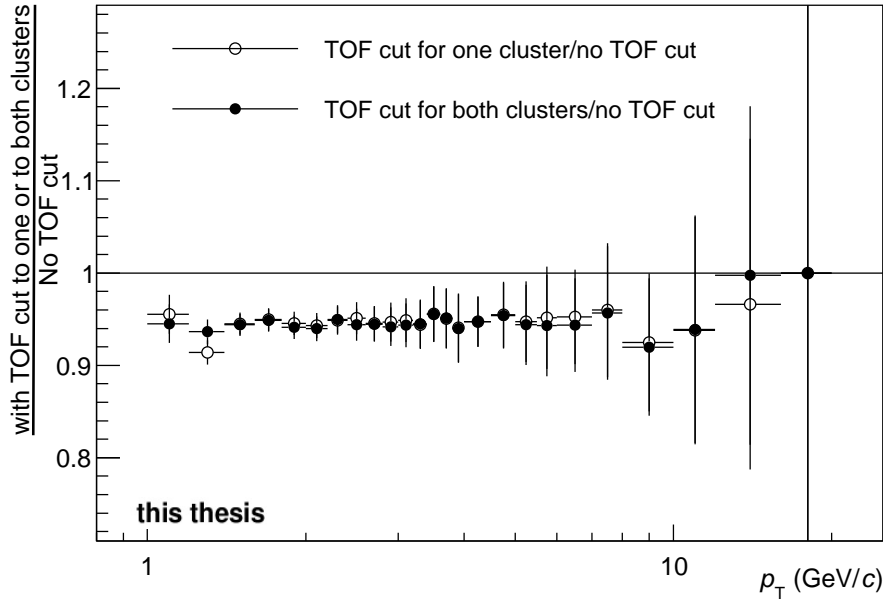
Figure 4.6: The yield ratio of with TOF cut to without TOF cut

the next bunch. The TOF cut probability "Prob" is defined as the probability of a photon in the main bunch crossing to pass the TOF cut or not to pass the TOF cut, and it is estimated as

$$\text{Prob} \times (1 - \text{Prob}) = \frac{1}{2} \times \frac{\text{N01}}{\text{N1} + \text{N0} + \text{N01}}. \tag{4.6}$$

Here N0 is the number of π^0s when both photons pass the cut $|t_{\text{cluster}}| < 100$ ns, N1 is the number of π^0s when both photons pass the cut $|t_{\text{cluster}} - 200| < 100$ ns, and N01 is the number of π^0s when one photon pass the cut $|t_{\text{cluster}}| < 100$ ns and second photon pass the cut $|t_{\text{cluster}} - 200| < 100$ ns or second photon pass the cut $|t_{\text{cluster}}| < 100$ ns and first photon pass the cut $|t_{\text{cluster}} - 200| < 100$ ns. From this equation (Eq.4.6) we get following two solutions.

$$\text{Prob}_+ = \frac{1}{2} + \frac{1}{2}\sqrt{\frac{\text{N1} + \text{N0} - \text{N01}}{\text{N1} + \text{N0} + \text{N01}}}, \tag{4.7}$$

$$\text{Prob}_- = \frac{1}{2} - \frac{1}{2}\sqrt{\frac{\text{N1} + \text{N0} - \text{N01}}{\text{N1} + \text{N0} + \text{N01}}} \tag{4.8}$$

63

Prob$_+$ (i.e. $1 -$ Prob$_-$) indicates the probability of a photon in the main bunch crossing to pass the TOF cut, and Prob$_-$ (i.e. $1 -$ Prob$_+$) indicates the probability of a photon in the main bunch crossing not to pass the TOF cut. We estimate the ratio of the contributions come from second peak of bunch crossing as N1 $\times$ $(1 -$ Prob$_+)$/N0 and the purity of the TOF cut estimated as $($N0 $-$ N1 $\times$ $(1 -$ Prob$_+))$/N0. The former is shown in the left of Fig.4.7 and the latter is shown in the right of Fig.4.7. It can be neglected because the contribution from the neighbouring bunch crossing is negligible compared to the number of π^0s from the main bunch crossing (N0).
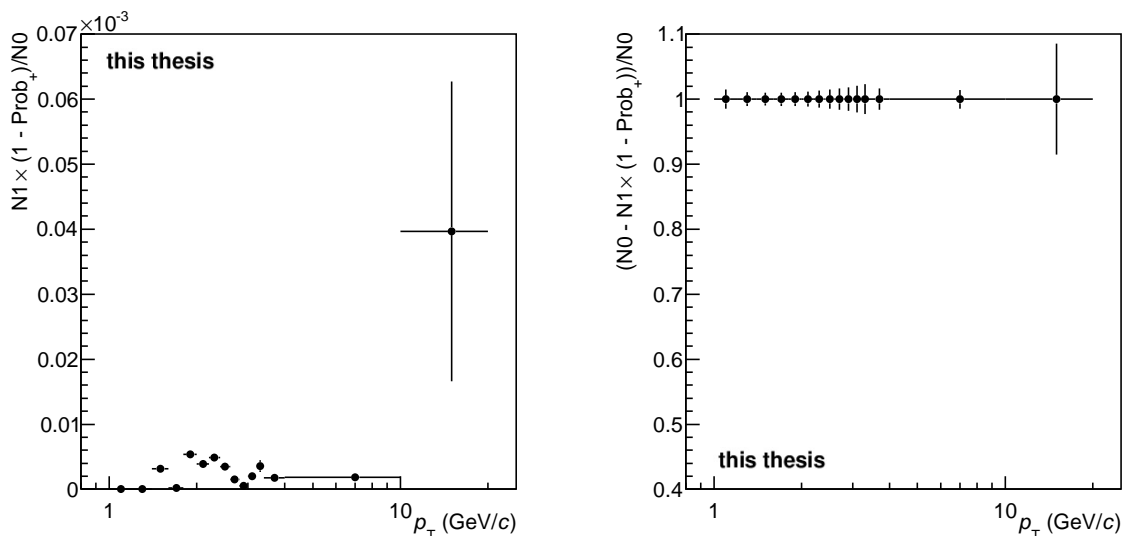
Figure 4.7: Contamination (left) and purity (right) for time-of-flight cut

4.3   Off-vertex π^0s production

Measurement for the π^0 yields is influenced by secondary π^0 from weak decays, mainly K_s^0 $\rightarrow 2\pi^0$. Detail is described in Ref. [57] and co-analyzer's (B. Polishchuk) ALICE analysis note. Invariant mass is reconstructed via photon candidates pairs assuming all photons come from the primary vertex. Therefore it includes photons from π^0 by hadron decay which happen close the primary vertex. This effect is not considered well in the experimentally and is estimated with single simulations.

Relative contributions of π^0 yields from non-π^0 hadrons are shown in the left plot of Fig.4.8. The contribution from hadrons other than K_s^0 is negligible. The contamination to yields from K_s^0 is about $4 \sim 10$ % in low-p_T and less than 2 % in high-p_T shown in Fig.4.8.
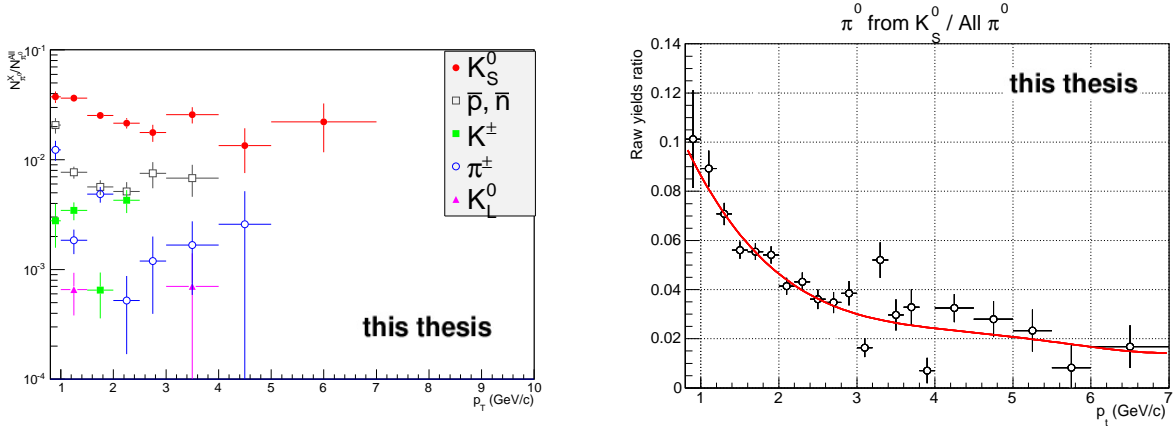
Figure 4.8: Relative contributions to π^0 yields (left) and feed-down correction (right)

4.4 Efficiency calculation in EMCal, PCM and PCM-Dalitz

Acceptance and reconstruction efficiencies for the π^0 and η meson measurements are estimated with DPMJET event generator for EMCal and HIJING event generator for PCM and PCM-Dalitz. The statistics at high-p_T in the HIJING sample is improved by adding extra π^0 and η signals with a flat p_T distribution. The PCM-Dalitz used a custom MC simulation also with HIJING as an event generator where the branching ratio $\pi^0 \to \gamma^*\gamma$ is increased by almost a factor 10 to gain statistics at a reasonable computing time. Using these simulations the p_T-dependent acceptance is calculated by taking the ratio between the number of π^0 (η) mesons with the daughters in the detector acceptance and the total number of generated π^0 (η) in the given rapidity interval. The p_T-dependent reconstruction efficiency is obtained by calculating the ratio of reconstructed π^0s to the generated π^0s in MC simulations.

65

Chapter 5

Systematic uncertainties

The relevant sources of systematic uncertainties on the π^0 measurement in p-Pb collisions at $\sqrt{s_{\mathrm{NN}}} = 5.02$ TeV have been identified and discussed below.

1. uncertainties due to different assumption in the raw yield extraction

2. uncertainties due to background estimation

3. uncertainties due to the absolute scale of the energy measurements in PHOS

4. uncertainties due to unknown non-linearity of the energy response of PHOS

5. uncertainties due to cluster timing cut

6. uncertainties in the π^0 yields due to the loss of the reconstructed π^0 due to the photon conversion in the ALICE medium

7. uncertainties due to finite acceptance of PHOS

5.1 Raw yield extraction

The systematic uncertainty due to the raw yield extraction is estimated by changing the assumption on the shape of the mass peak. We compare the efficiency corrected yield calculated by taking the numerical integral of the number of entries within $\pm 2\sigma$ and $\pm 3\sigma$ from the peak position in the Gaussian fit and the Crystal Ball fit for signal peak (Fig.5.1). For both cases, background around signal peak is subtracted by estimating with using the event mixing technique described in the chapter 3. The yields in the MC simulation are counted as in the real data, by assuming the same functions for the signal and by varying the fit limits within the same intervals ($\pm 2\sigma$, $\pm 3\sigma$). The yields differences are compared via the ratio of the individual yield to the average yield and the RMS/Mean at each p_{T} bin is attributed to the systematic uncertainty of the yield extraction.
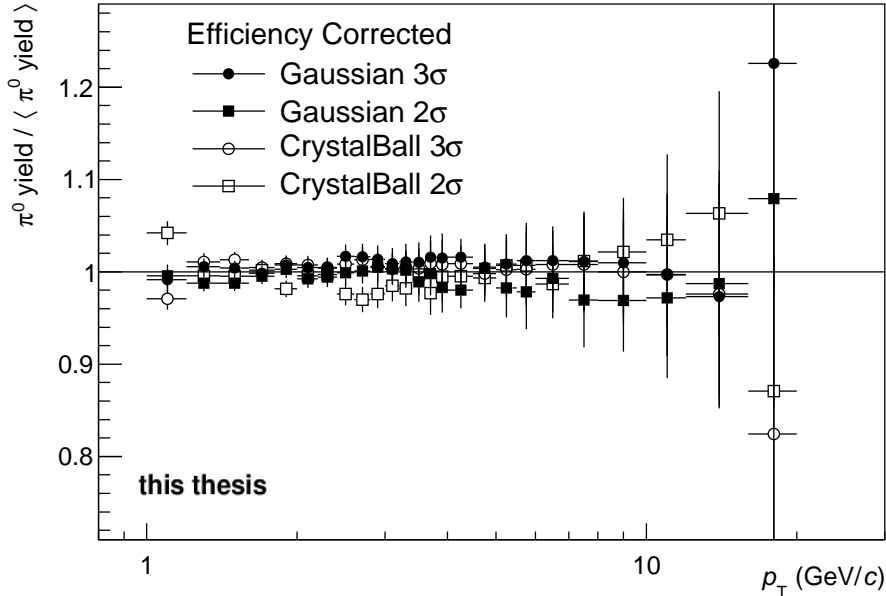
Figure 5.1: Comparison of π^0 raw yield with different assumptions

5.2 Background estimation

The background is estimated by the event mixing technique. The mixed mass distribution is normalized to the same mass distribution with a second order polynomial. However the π^0 yields are changed slightly by using function in the normalization. The systematic uncertainty due to background subtraction is calculated by comparing the difference of the efficiency corrected yields, if a first order polynomial or a second order polynomial is used in the fitting. Besides the yield depends on the fitting range. To estimate the contributions of this effect, two different ranges have been selected. The fit mass ranges are 0.07 - 0.22 GeV/c^2 and 0.09 - 0.25 GeV/c^2. In MC simulation, the same procedure is followed. The ratio of the efficiency corrected yield to their average is shown in Fig.5.2. In each p_T, the RMS/Mean in Fig.5.2 is selected as systematic uncertainty due to background estimation. This uncertainty becomes larger in the low-p_T region because the background becomes larger at low-p_T and it is hard to estimate it.

5.3 Absolute energy scale

The absolute energy scale has two components. To fix absolute energy scale we use π^0 peak. As a result, this scale depends on the uncertainty in geometrical position of PHOS. We estimate this uncertainty using charged track extrapolations to PHOS, as described in the ALICE internal analysis note for pp [57] and PbPb [68]. Within this approach we estimated uncertainty as 0.2 %.

67
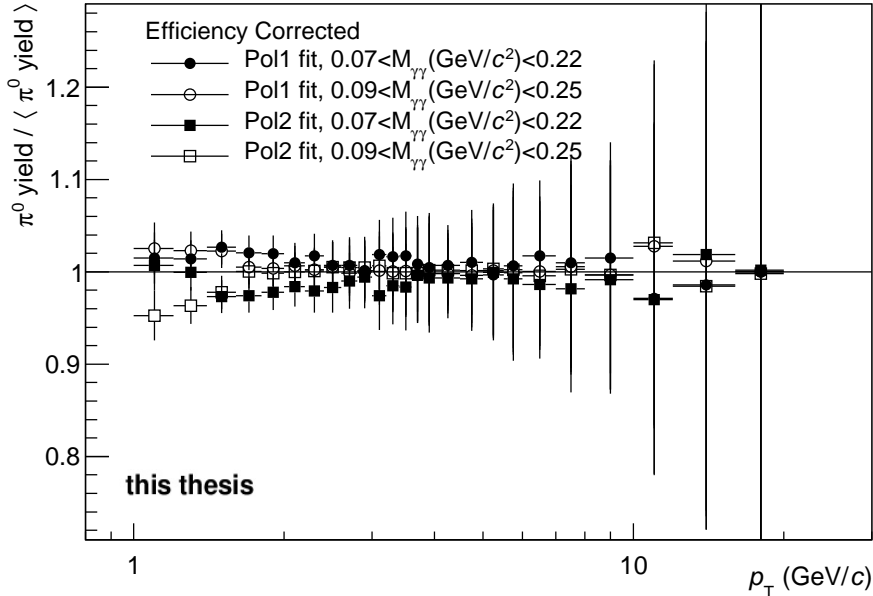
Figure 5.2: Comparison of π^0 efficiency corrected yield with different fit functions and fit ranges

Later we cross-checked absolute energy scale using electron energy-momentum E/p ratio. Electron analysis demonstrated somewhat worse agreement between PHOS and tracking system energy scale: 0.5 %, what partially can be attributed to imperfections in TPC calibration and uncertainty in the material budget between PHOS and TPC. The 0.5 % uncertainty is used in the absolute energy scale and this uncertainty is estimated with following formula:

$$Error = Max(1 - f(p_{\mathrm{T}} + \delta p_{\mathrm{T}})/f(p_{\mathrm{T}}), \; f(p_{\mathrm{T}} - \delta p_{\mathrm{T}})/f(p_{\mathrm{T}}) - 1). \tag{5.1}$$

Here, the function "$f(p_{\mathrm{T}})$" is the Tsallis function described by Eq.6.1. The result of $f(p_{\mathrm{T}} \pm \delta p_{\mathrm{T}})/f(p_{\mathrm{T}})$ is shown on the left plot of Fig.5.3. The largest deviation from unity is shown on the right plot of Fig.5.3 and is used as the systematic uncertainty related to the absolute energy scale.

5.4 Non-linearity

The π^0 mass depends on the p_{T}. This dependence appears due to two effects. The first is related to the final resolution and variable slope of the π^0 spectrum. The second and most important is the non-linearity of PHOS [57]. This effect is non-linearity response coming from discrepancy of energy measurement between real and simulation. The non-linearity effect in energy response in PHOS is calculated by the Monte Carlo simulations used for the efficiency calculation. MC simulations and a simple non-linearity model are used to correct the measured cluster energy:

$$E_{\mathrm{cor}} = E \cdot f(E), \quad f(E) = c \left(1 + \frac{a}{1 + E^2/b^2} \right) \tag{5.2}$$
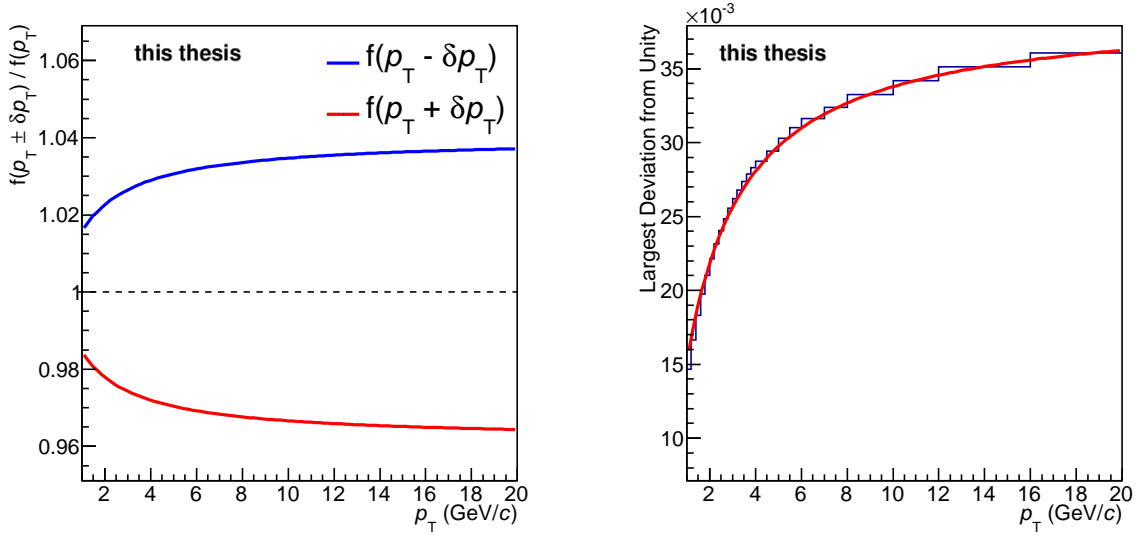
Figure 5.3: Ratio of $f(p_T \pm \delta p_T)/f(p_T)$ (left) and largest deviation from unity (right)

where E_{cor} is the corrected cluster energy, E is the measured cluster energy and others (a, b and c) are correction parameters. Besides, the additional PHOS mis-calibrations have been simulated by smearing the energy of each cell in the cluster with a Gaussian of dispersion w around the original value. The best value of the correction parameters are defined by χ^2 calculation of the difference between the peak position in MC simulation and real data. Since here we are interested only in the difference in shape, we first calculate the ratio of peak positions R_m. Then we calculated mean of this ratio:

$$< R_m >= \sum \frac{R_i}{\sigma_i} / \sum \frac{1}{\sigma_i} \tag{5.3}$$

where σ_i is an error in a given bin. Then we calculate χ^2 as a deviation from the mean:

$$\chi^2 = \sum \frac{(R_i - < R_m >)^2}{\sigma_i}. \tag{5.4}$$

The dependence of the χ^2 on the parameters a and b is shown in the Fig.5.4. The masses as a function of p_T for different parameters a and b, are shown in Fig.5.5 and Fig.5.6. In the left figure of Fig.5.5 and Fig.5.6, black marker represents the real data and other colors represent the MC simulation varying parameter. The values of the parameters a and b for which the χ^2 is minimum are $a = 0.087$ and $b = 1.01$. So the nearest parameters are used as optimal parameters,

$$a = 0.085, \quad b = 1.00. \tag{5.5}$$

The optimal value of parameter c is determined by general χ^2 calculation of the difference between the peak position and width in MC simulation and real data which is shown in Fig.5.7. In the left figure of Fig.5.7, black marker represents the real data and other colors represent the MC simulation

varying parameter. The value of the parameter c for which the χ^2 is minimum is $c = 1.03$. The final non-linearity correction with optimal parameters is following:

$$E_{\mathrm{cor}} = E \cdot f(E), \quad f(E) = 1.03 \left(1 + \frac{0.085}{1 + E^2/1.00^2} \right). \tag{5.6}$$

This correction is applied to the MC simulation in order to reproduce non linearity effect in the MC simulation.
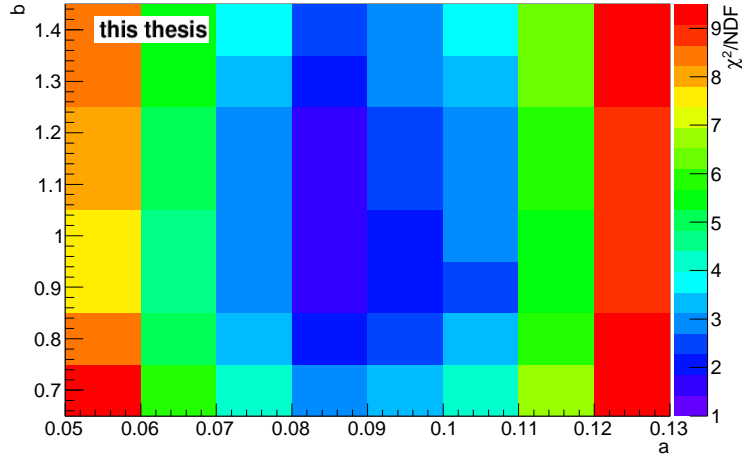
Figure 5.4: Parameter dependence of χ^2 calculation

The π^0 mass peak and width by using optimal values for the correction parameters are shown in Fig.5.8. Both mass peak position and width become close to the real data by using the optimal parameters. Then the efficiencies are estimated with $(a \pm \delta a, b)$ and $(a, b \pm \delta b)$ combinations (see left plot in Fig.5.9) and found the maximum deviation from the default (see right plot in Fig.5.9) which is fitted by the following,

$$f(p_{\mathrm{T}}) = \frac{p_0}{p_{\mathrm{T}}^n} + p_1 \tag{5.7}$$

where p_0 and p_1 are free parameters, and n is indefinite parameter. The optimal n is found by requiring χ^2/NDF of the fit is minimum. The χ^2/NDF is minimum at $n = 9$. So Eq.(5.8) is use as the systematic uncertainty related to non linearity.

$$f(p_{\mathrm{T}}) = \frac{0.05}{p_{\mathrm{T}}^9} + 0.03 \tag{5.8}$$

5.5   Cluster timing cut

The systematic uncertainty due to the cluster timing cut is estimated by a TOF cut at 100 ns, 50 ns and 80 ns. The TOF cut at 50 ns and 80 ns are slightly severe cuts than the default cut. The
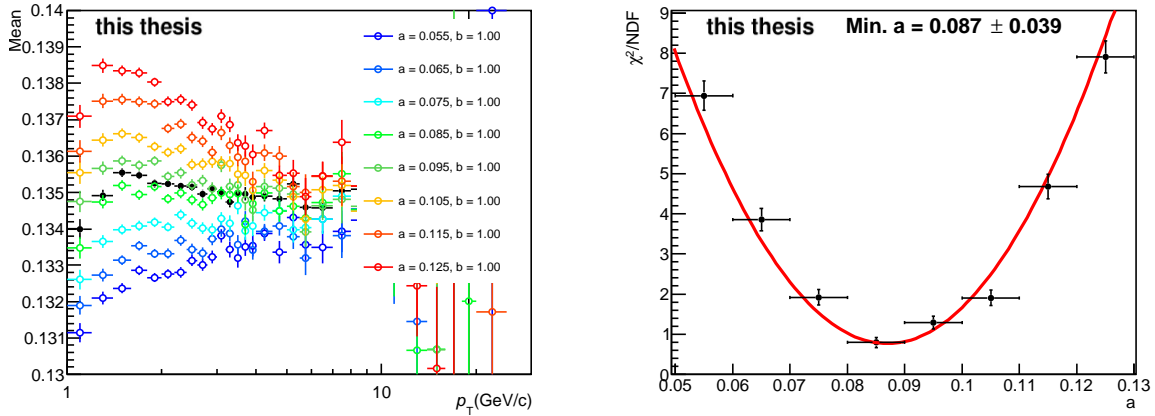
Figure 5.5: Comparison of the π^0 mass in real data and MC for varying parameter a
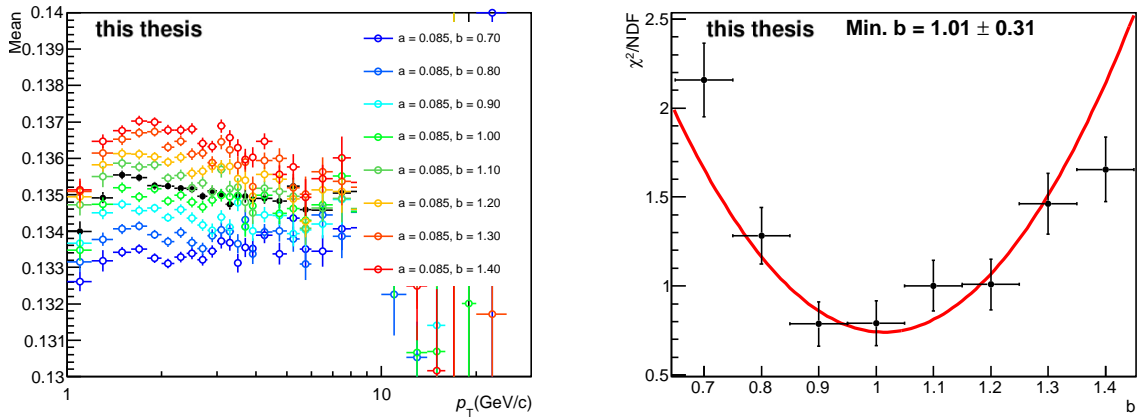
Figure 5.6: Comparison of the π^0 mass in real data and MC for varying parameter b
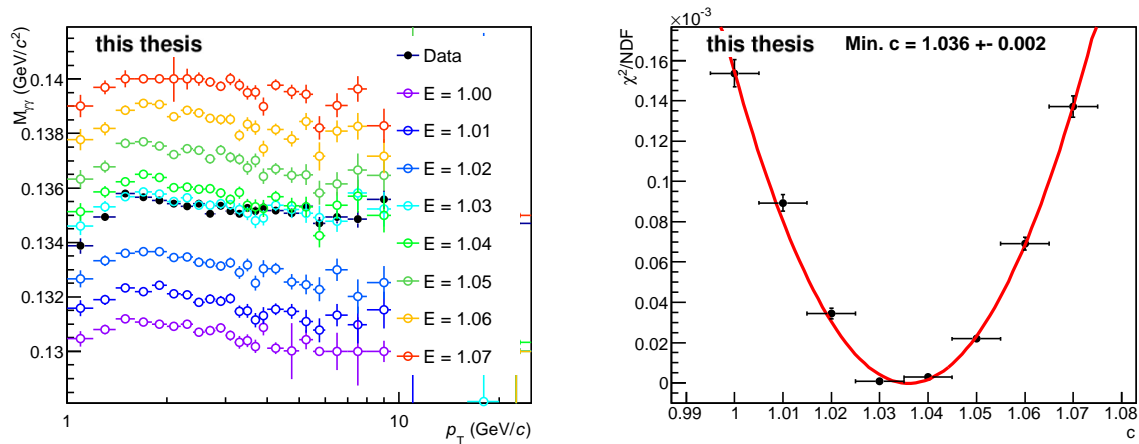
Figure 5.7: Comparison of the π^0 mass in real data and MC for varying parameter c
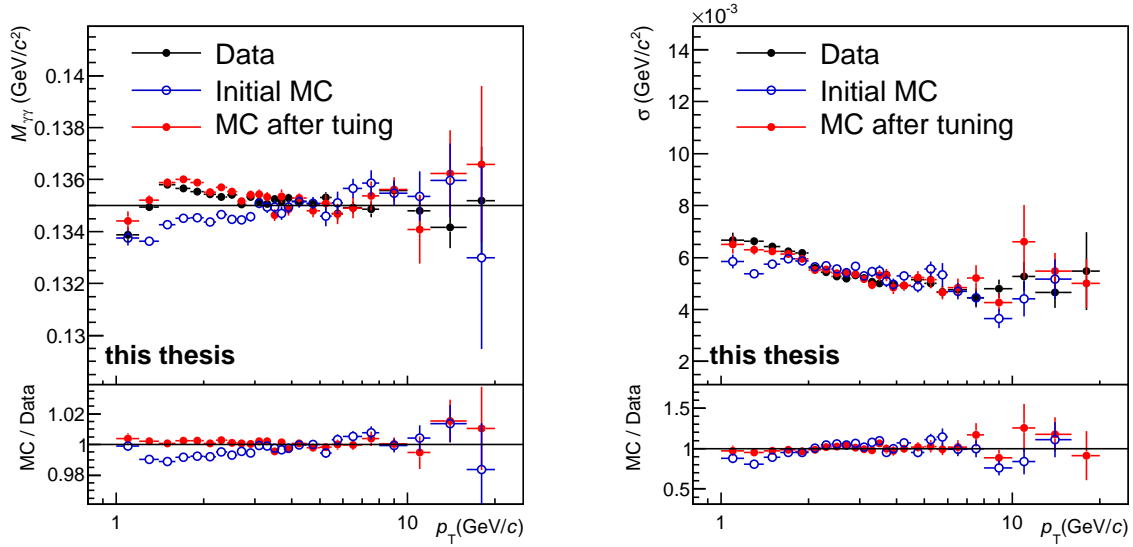
Figure 5.8: Comparison of the π^0 mass (left) and width (right) in data and MC with and without tuning using the optimal parameters
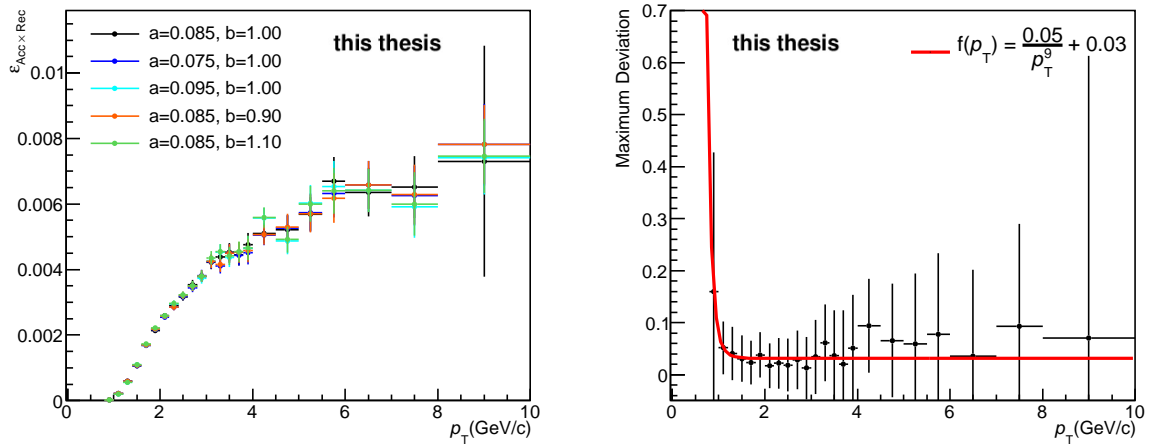
Figure 5.9: Efficiencies (left) and the maximum deviation from default (right)

TOF cut efficiency corrected yields are compared in the left plot of Fig.5.10 and the ratio of RMS to Mean in each p_T is selected as systematic uncertainty shown in the right plot of Fig.5.10. It is under 0.1 % for almost entire p_T range and found to be negligible because it is smaller than the other uncertainties.
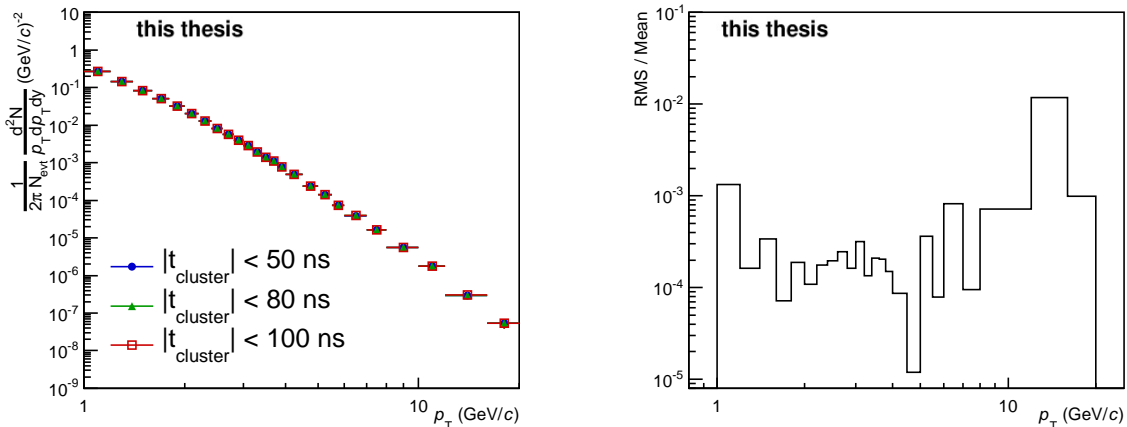
Figure 5.10: Comparison of efficiency corrected yield with a TOF cut at 100 ns, 80 ns and 50 ns (left), and RMS/Mean (right)

5.6 Conversion

The uncertainty related to conversion (3.5 %) is taken from pp published paper [32] because the detector setup does not change. According to Ref. [32] and its ALICE internal analysis note [57], the conversion probability is estimated by comparing π^0 measurement with and without magnetic field. Photon conversion can reduce the number of π^0s detected by PHOS. However PHOS can detect electron and positron which are pair-created in the surface of PHOS. The distance between the electron and positron on the surface of PHOS depends on the distance from the conversion point to PHOS, π^0 energy and strength of the magnetic field. If the distance between the electron and positron on the surface of PHOS is small enough, the conversion electron-positron pair may produce only one single cluster. It is too close hit points to separate clusters. In this case the cluster energy is comparable to the energy of original photon, and the original π^0 can still be reconstructed. For a more complicated situation, we may reconstruct two π^0 from one π^0. When the converted photon carried out only a small portion of π^0 momentum and the electron-positron hit slightly different places on the PHOS surface, we can have three clusters created by the electron and the positron and the other photon. Two cluster pairs, electron-photon pair and positron-photon pair, can be reconstructed with the effective mass close to the π^0 mass, and then one π^0 is recognized as two π^0 with a little smaller mass.

If the magnetic field is off, the converted electron and positron via photon conversion with the inner detectors hit close points on the PHOS and create only one cluster because the opening of

them are usually quite small. Thus the number of π^0 without the magnetic field is equal to one without the inner detectors. The number of π^0 with and without the magnetic field are examined in order to estimate the material budgets between the collision vertex and PHOS.

5.7 Acceptance

The influence of PHOS acceptance on the π^0 is studied and it is taken into account as an uncertainty. Raw yields and efficiency are calculated by varying the distance from the closest bad channel and this uncertainty is estimated by comparing efficiency corrected yields. PHOS hit maps of clusters located 1, 2 and 3 cells away from the closest bad channel are shown in Fig.5.11, 5.12 and 5.13. The π^0 raw yields in data and MC are calculated for each distance to the bad channel with the same method described in the chapter 3 and it is shown in Fig.5.14. The uncertainty related to the different acceptance is estimated by comparing efficiency corrected yields. The ratio of each efficiency corrected yield to the average yield is shown in Fig.5.15 and each ratio is fitted by a constant function in p_T range from 2 to 10 GeV/c. The largest deviation from unity in fitting is 2.8 % and it is used as systematic uncertainty due to the acceptance.

In summary, the different contributions to the total systematic uncertainty are presented in Fig.5.16 and Table.5.1. The largest contribution to the total systematic uncertainties comes from the material budget (conversion) in front of the PHOS.

p_T(GeV/c)	1.1	5.2	9	14	18
Raw yield extraction(%)	2.6	1.0	1.9	3.7	16.2
Background Estimation(%)	2.8	0.2	0.9	1.5	1.5
Conversion(%)	3.5	3.5	3.5	3.5	3.5
Acceptance(%)	2.8	2.8	2.8	2.8	2.8
Non-linearity(%)	5.2	3.1	3.1	3.1	3.1
Absolute energy scale(%)	1.5	3.0	3.3	3.5	3.6
Time-of-flight cut(%)	0.1	<0.1	<0.1	1.2	0.1
Total(%)	7.8	6.3	6.7	7.7	17.5

Table 5.1: Summary table of different contributions to systematic uncertainties

5.8 Systematic uncertainty in EMCal analysis

Systematic uncertainties for π^0 and η meson measurement in p-Pb collisions at $\sqrt{s_{NN}} = 5.02$ TeV for EMCal analysis are estimated by varying the cut parameters (more description in Ref. [59]). The variations are chosen such that a reasonable deviations can be accessed. All uncertainties within one cut variation are calculated bin by bin as maximum negative or positive deviation from the standard cut and then the average of the maximum deviations in both directions is taken as the systematic uncertainty for this particular cut variation in the corresponding p_T bin. Uncertainty

Figure 5.11: PHOS hit map of clusters located 1 cells away from the closest bad channel

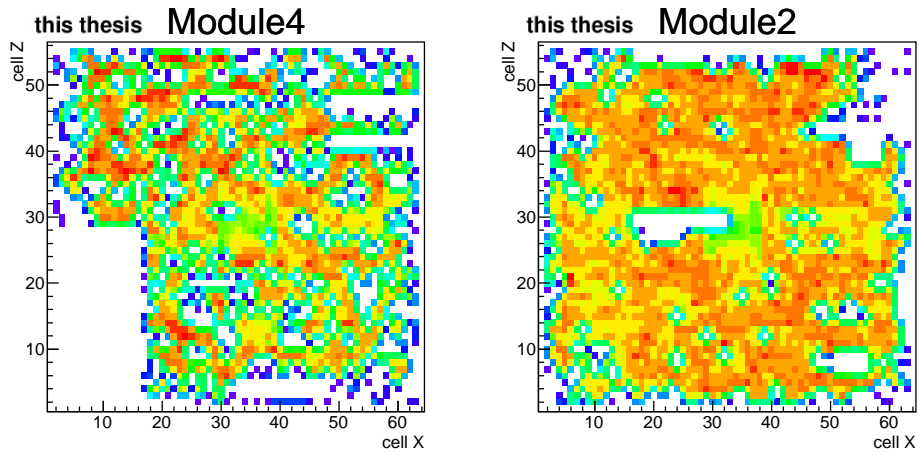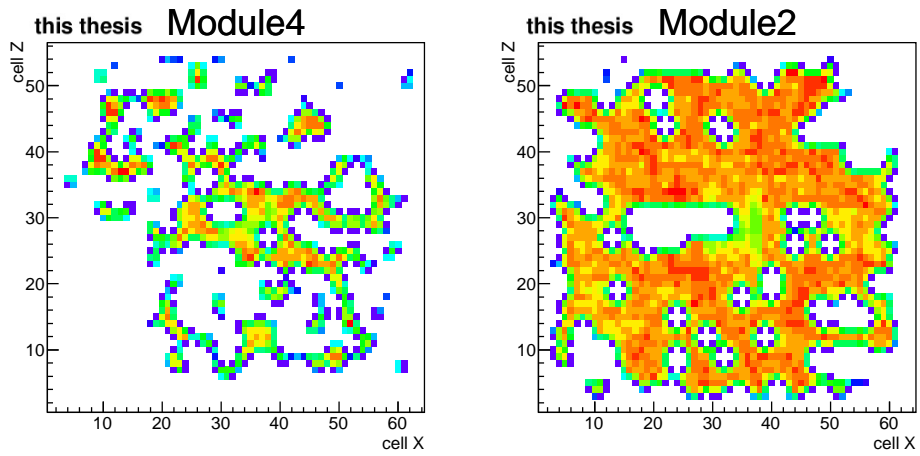Figure 5.12: PHOS hit map of clusters located 2 cells away from the closest bad channel
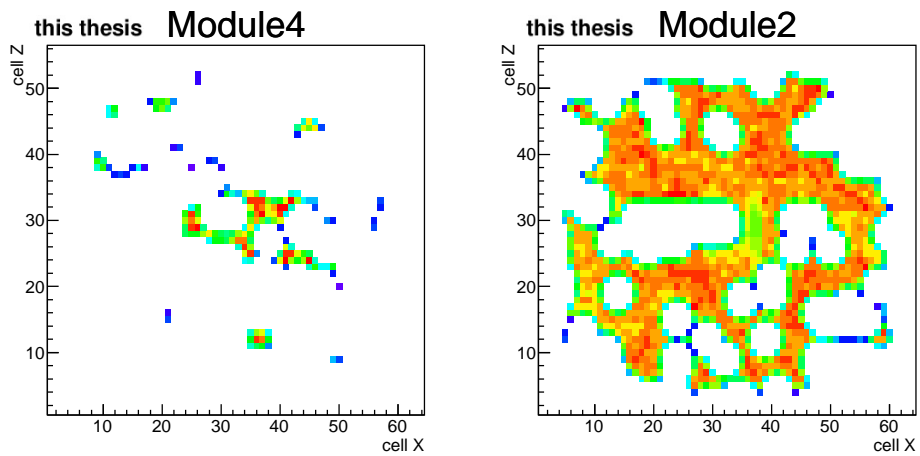
Figure 5.13: PHOS hit map of clusters located 3 cells away from the closest bad channel

75
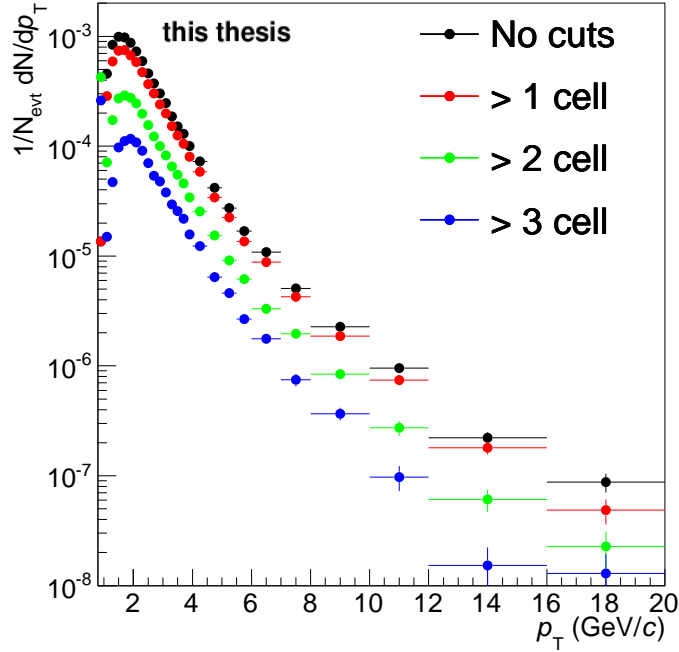
Figure 5.14: Raw π^0 yields if clusters located 1, 2 and 3 cells away from a bad channel are considered.
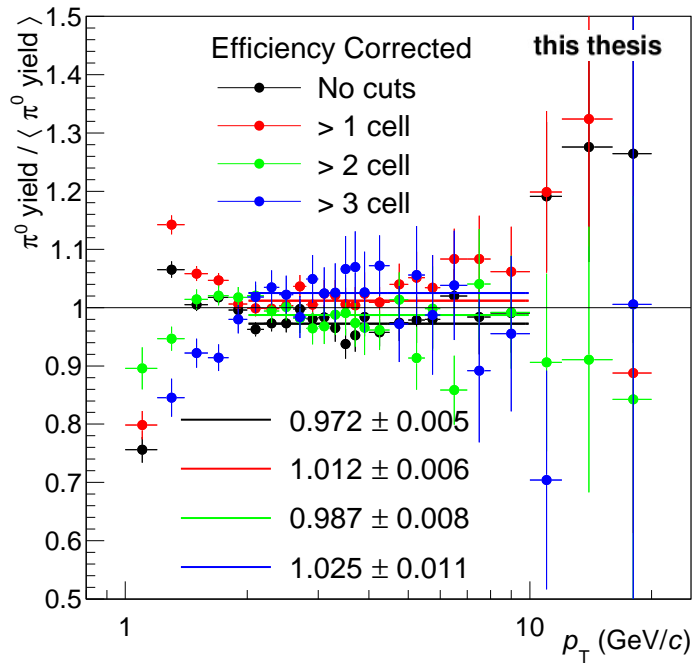
Figure 5.15: Comparison of efficiency corrected yields if clusters located 1, 2 and 3 cells away from a bad channel are considered.
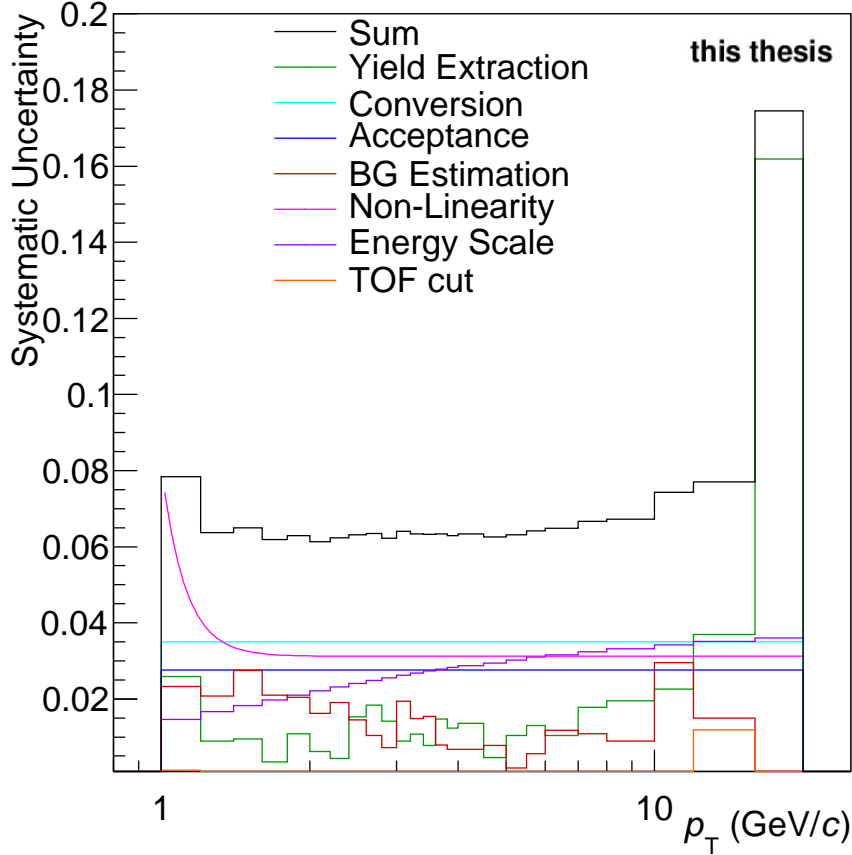
Figure 5.16: Summary of different contributions to systematic uncertainties

on photon reconstruction is varied parameters of cluster formation, which are track matching, minimum cluster energy, the minimum number of cells of cluster and shower shape parameter M_{02}. Uncertainty related to meson reconstruction is estimated by varying parameters, opening angle and rapidity range. Uncertainty due to material budget is estimated by comparing the results for π^0 spectrum in each module with and without Traditional Radiation Detector (TRD) in front of EMCal, resulting in a 3 % uncertainty. The TRD material budget represents $\approx 1/2$ of the total material in front of EMCal, thus such an estimation does not allow to access the full uncertainty. The next largest contribution would to the material should be the Time-Of-Flight detector (TOF), which is so close to EMCal that most of the converted photons will still be reconstructed in the same cluster. An initial estimation on this uncertainty is 5 %, which is added quadratically to the uncertainty from the TRD material budget. Thus the systematic uncertainty related to the material budget in front of EMCal is 5.83 %. Uncertainty due to yield extraction is estimated varying the integration window for the signal extraction as well as the range for the normalization of the

background. It contains a constant uncertainty of 4 % to account for the difference the validate and pure reconstruction efficiency. The uncertainty of yield extraction is one of the largest sources.

Cluster energy calibration is estimated by using a different method to obtain cluster energy correction. The correction can be obtained by reconstructing π^0 where both photons are reconstructed with EMCal or one with EMCal and the other with PCM. The fully corrected spectra for the π^0 using both correction methods give access to the systematic uncertainty. In addition, uncertainty of 0.95 % is attributed to the cell timing cut. Once again, this uncertainty is obtained by comparing the fully corrected spectra of the π^0, where different cell timing cuts are applied. The standard timing cut is $|t_{\text{cell}}| < 500$ ns, and variation cuts are $|t_{\text{cell}}| < 100$ ns and $|t_{\text{cell}}| < 200$ ns.

5.9 Systematic uncertainty in PCM and PCM-Dalitz analyses

Systematic uncertainties for π^0 and η meson measurement in p-Pb collisions at $\sqrt{s_{\text{NN}}} = 5.02$ TeV for PCM [60] and PCM-Dalitz [61] analyses are estimated by varying the cut criteria within reasonable ranges. Uncertainty due to material budget is estimated comparing measurements without magnetic field to the standard measurements with magnetic field and used 9 % for PCM analysis, and 4.5 % for PCM-Dalitz as only one photon is present in the Dalitz decay channel. Uncertainty related to yield extraction is estimated the difference between originating range and a narrow or a wider ranges for the integration window. Uncertainty of track reconstruction includes the contribution from transverse momentum cut on the electrons and ratio of found the number of TPC clusters to findable the number of TPC clusters. For PCM-Dalitz, in addition, it contains the contribution from DCA cut, transverse momentum cut, ratio of found the number of TPC clusters to findable the number of TPC clusters and the number of TPC clusters for primary electrons. The cut criteria are different between primary electrons and non-primary electrons. Uncertainty related to electron selection and hadron rejection contains the $\mathrm{d}E/\mathrm{d}x$ cuts and momentum range to apply the different number of σ. Contribution from background is estimated via variation of the number of tracks in event mixing.

5.10 Summary of systematic uncertainties

Systematic uncertainties of π^0 measurement for different methods are summarized in Tab.5.2. The largest contribution to the total systematic uncertainties for PHOS and EMCal comes from the material budget in front of the calorimeters, the raw yields extraction and the cluster selection cuts, and that for PCM and PCM-Dalitz are the material budget and photon extraction. The systematic uncertainties for the η meson measurement is slightly larger than π^0 measurement. The reason is that mainly the uncertainty related to the yield extraction increases. The systematic uncertainties of the η/π^0 ratio are evaluated independently such that the material budget uncertainty is canceled out.

	PHOS		EMCal		PCM		PCM-Dalitz	
p_{T} (GeV/c)	1.5	7.5	1.5	7.5	1.5	7.5	0.9	3.1
Material budget	3.5	3.5	5.8	5.8	9	9	4.5	4.5
Yield extraction	1.0	1.8	0.8	0.8	0.7	2.8	3.5	1.1
γ reconstruction			3.3	3.8	1.2	5.2	2.3	1.8
e$^+$ / e$^-$ reconstruction					0.7	4.8	2.7	2.3
Track reconstruction					0.6	2.9	1.6	2.0
e$^+$ / e$^-$ sec. rejection							4.5	2.8
Dalitz branching ratio							3.0	3.0
Cluster energy scale	1.8	3.2	3.0	3.0				
Cluster non-linearity	3.2	3.1	1.0	1.3				
Cluster shape			1.6	3.2				
π^0 reconstruction			1.6	1.8	0.4	1.5	1.9	2.0
Generator efficiency			4.0	4.0				
Acceptance	2.8	2.8						
Background estimation	2.8	1.1			0.3	2.1	1.8	2.0
Pile-up correction					0.3	0.3		
Total	6.5	6.7	8.8	9.4	9.2	12.4	9.2	7.7

Table 5.2: Summary of systematic uncertainties of π^0 measurement for PHOS, EMCal, PCM and PCM-Dalitz

Chapter 6

Results

6.1 π^0 and η meson invariant yield

The reconstructed π^0 raw yield is converted to an invariant yield spectrum by applying the acceptance and reconstruction efficiencies. The efficiencies are calculated by MC simulation which are reproducing the real detector. The π^0 invariant yield measured by PHOS in p-Pb collisions at $\sqrt{s_{\mathrm{NN}}} = 5.02$ TeV is shown in Fig.6.1. The π^0 invariant yield in p-Pb collisions at $\sqrt{s_{\mathrm{NN}}} = 5.02$
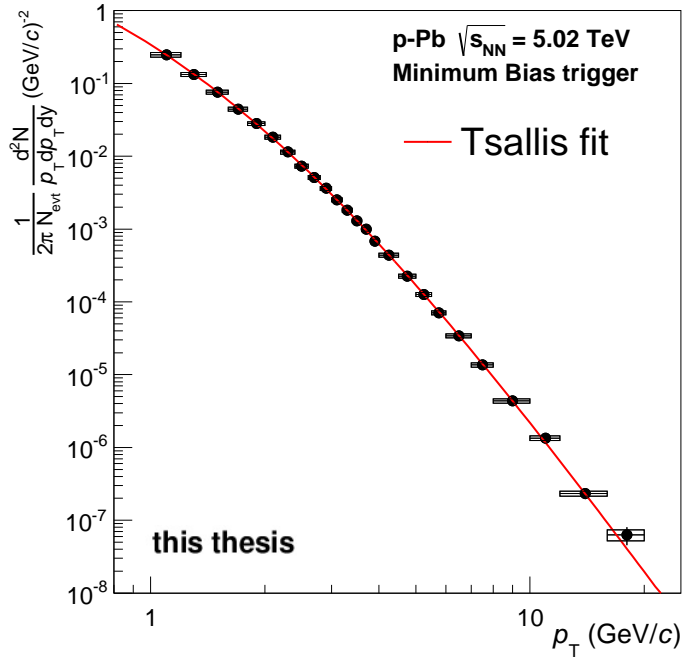

Figure 6.1: The π^0 invariant yield in p-Pb collisions at $\sqrt{s_{\mathrm{NN}}} = 5.02$ TeV

TeV is fitted by the Tsallis parameterization as defined

$$\frac{1}{2\pi p_{\mathrm{T}} N_{ev}} \frac{\mathrm{d}^2 N}{\mathrm{d}p_{\mathrm{T}} \mathrm{d}y} = \frac{A}{2\pi} \frac{(n-1)(n-2)}{nC[nC + m(n-2)]} \frac{1}{c^2} \cdot \left(1 + \frac{\sqrt{p_{\mathrm{T}}^2 + m^2} - m}{nC}\right)^{-n}, \qquad (6.1)$$

where A, C and n are fit parameters, and m is the meson rest mass. To measure the π^0, the ALICE experiment has individual ways, PHOS, EMCal, PCM and PCM-Dalitz. The π^0 in PHOS and EMCal are reconstructed by detecting photon pairs. The PCM and PCM-Dalitz reconstruct the π^0 via their photon decay channel $\pi^0 \to \gamma\gamma \to e^+e^-e^+e^-$ and via their Dalitz decay channel $\pi^0 \to e^+e^-\gamma$, respectively with using the ALICE inner detectors, the Inner Tracking System (ITS) and the Time Projection Chamber (TPC). The comparison of the π^0 invariant yield from the individual analyses, PHOS, EMCal, PCM and PCM-Dalitz, is shown in Fig.6.2.

The PCM covers the low-p_{T} region from 0.3 to 14 GeV/c and PHOS covers the high-p_{T} region
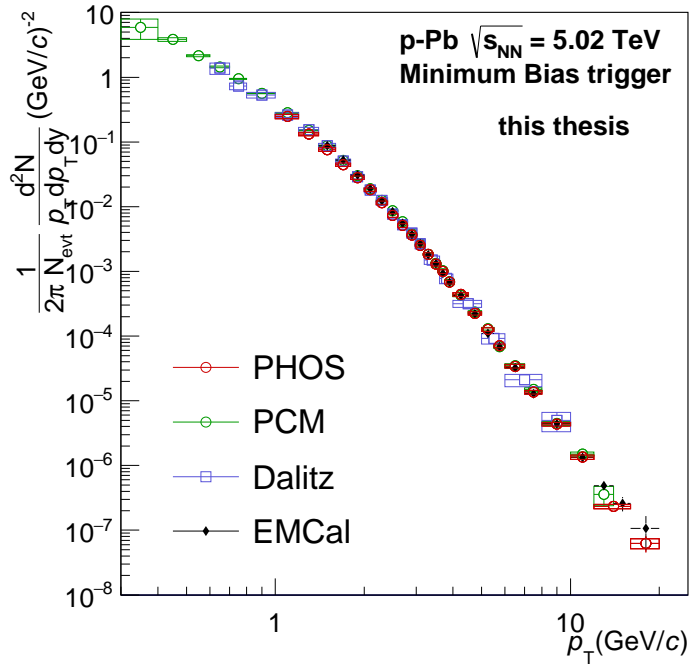
Figure 6.2: Comparison of π^0 invariant yields in p-Pb collisions at $\sqrt{s_{\mathrm{NN}}} = 5.02$ TeV obtained by the different methods.

from 1 to 20 GeV/c. PHOS, EMCal, PCM and PCM-Dalitz analyses are consistent within their uncertainties for almost entire p_{T}.

Individual four π^0 invariant yields in p-Pb collisions are combined to a common invariant yield. Since all π^0 analyses do not cover the same p_{T} range and do not have the same p_{T} binning, the finest possible binning for the combined yield is chosen. The two last EMCal points do not
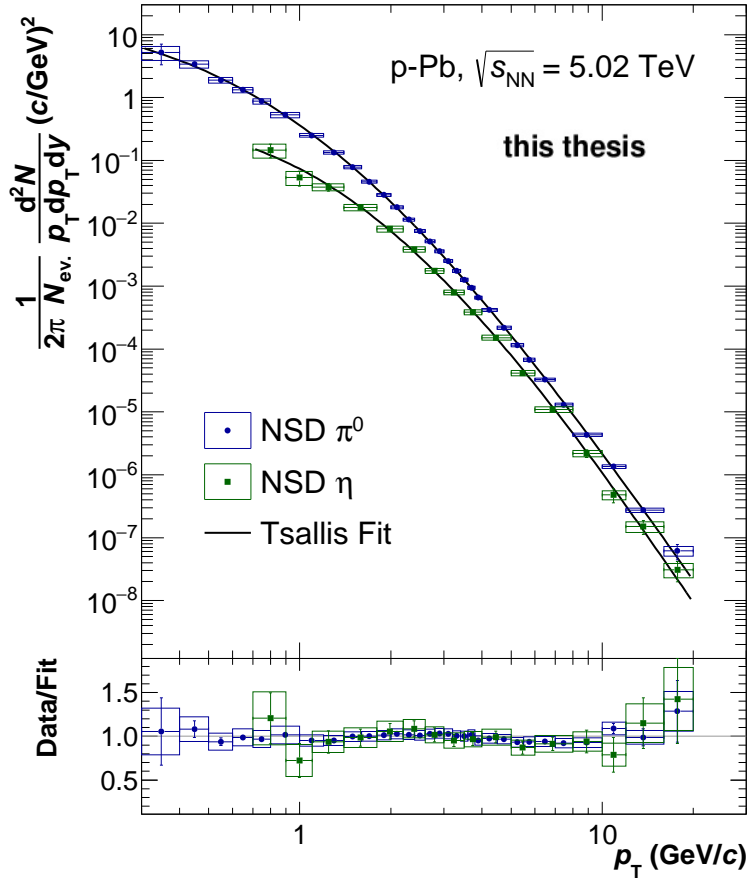
Figure 6.3: The π^0 and η meson invariant yield in p-Pb collisions with Tsallis fit.
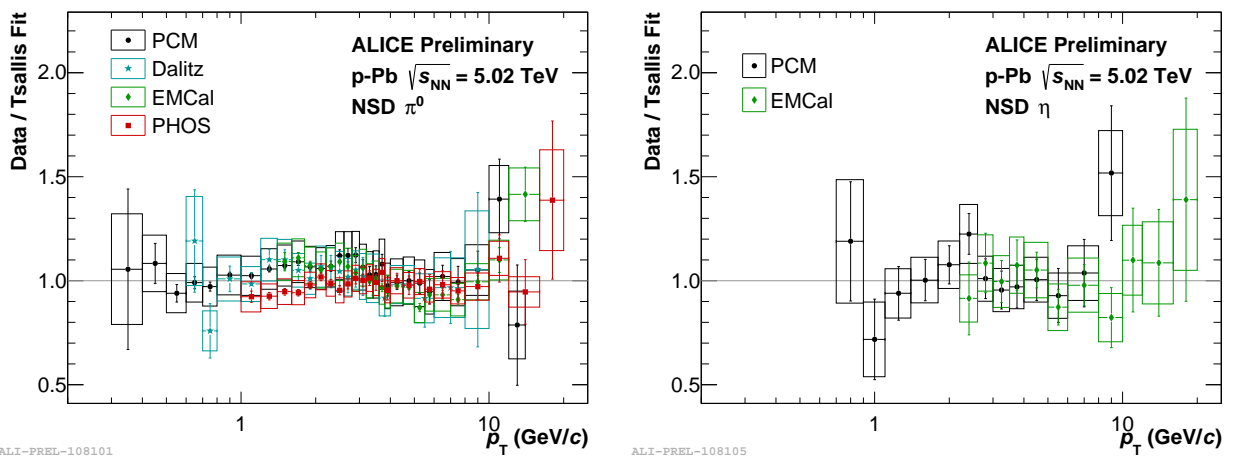
Figure 6.4: Ratio of individual π^0 (left) and η meson (right) invariant yield to Tsallis fit to combined yield.

contribute to the combination as the MC efficiencies suffer from too low statistics and are just not reliable there. The yields are combined bin by bin with weight according to their statistics and systematic uncertainty. For η meson, invariant yields measured by EMCal and PCM are combined to a common invariant yield with same procedure. The combined invariant π^0 yield normalized to the total number of NSD collisions with a normalization factor of 96.4 ± 3.1 % [54]. The combined π^0 and η meson invariant differential yields in p-Pb collisions at $\sqrt{s_{NN}} = 5.02$ TeV is shown in Fig.6.3. The combined π^0 yields are measured by PHOS, EMCal, PCM and PCM-Dalitz within the p_T range $0.3 - 20$ GeV/c and the combined η meson yields are measured by EMCal and PCM within the p_T range $0.7 - 20$ GeV/c. There is not enough statistics and small acceptance for η meson measurement in PHOS and PCM-Dalitz. The invariant yields are fitted by the Tsallis function 6.1 and the ratio of measured yield to the corresponding fit is shown in the bottom panel of the Fig.6.3. The Tsallis fit describes well the meson yield and the fit parameters and χ^2/NDF are collected in Tab.6.1. The fit is used to perform bin shift correction in x-direction for the finite bin width of spectrum. Ratio of individual π^0 (left plot) and η meson (right plot) invariant yield to the Tsallis fit to combined yield are presented in Fig.6.4

	A	C (GeV/c)	n	χ^2/NDF
π^0 spectrum fit	8.20 ± 0.44	0.17 ± 0.01	7.19 ± 0.09	0.43
η spectrum fit	0.91 ± 0.13	0.27 ± 0.02	7.50 ± 0.39	0.31

Table 6.1: Tsallis fit parameters of π^0 and η meson invariant yield in p-Pb collisions

Figure 6.5 presents comparison of combined invariant yields for the π^0 and η meson to EPOS3 theoretical calculations. The model calculation reproduces well the π^0 yields in entire p_T range but $p_T > 10$ GeV/c, and overestimates the data by a few percent in this region. For η meson, the model reproduces the yields in only intermediate-p_T region, $2.5 - 4$ GeV/c. Differences of 40 % at a maximum are observed in low-p_T, and the model calculation is overestimated the data by almost a factor 2 at $p_T > 10$ GeV/c.

6.2 η/π^0 ratio

The η/π^0 ratio in p-Pb collisions has been measured and it is shown in Fig.6.6. The p_T binning of the π^0 is coordinated and reconstructed in the same binning as the η meson in this calculation. The ratio is calculated individually with PCM and EMCal and then combined because some systematic uncertainties of the yield measurement cancel this way. The ratio in p-Pb collisions increases with p_T in the low-p_T region below 4 GeV/c and reaches a plateau of 0.47 ± 0.02 in the high-p_T region from 4 GeV/c. The plateau value for η/π^0 ratio in the world result reaches 0.48 ± 0.03 (0.47 ± 0.03) above 2 GeV/c measured in pp (d-Au) collisions with PHENIX [69] and agrees with the world η/π^0 ratio for pp, p-A and A-A collisions. Figure 6.6 is compared to the ALICE pp measurement at $\sqrt{s} = 7$ TeV [32] and it is good agreement between pp and p-Pb collisions. In addition, ALICE has measured η/π^0 ratio in Pb-Pb collisions with two centrality classes ($0 - 10$ % and $20 - 50$ % centrality classes) [34] and $K^{\pm}/\pi^0$ ratio in central Pb-Pb collisions [36], and η/π^0 ratio in p-Pb collisions is consistent with them. It means that the ratio does not depend on the collision system
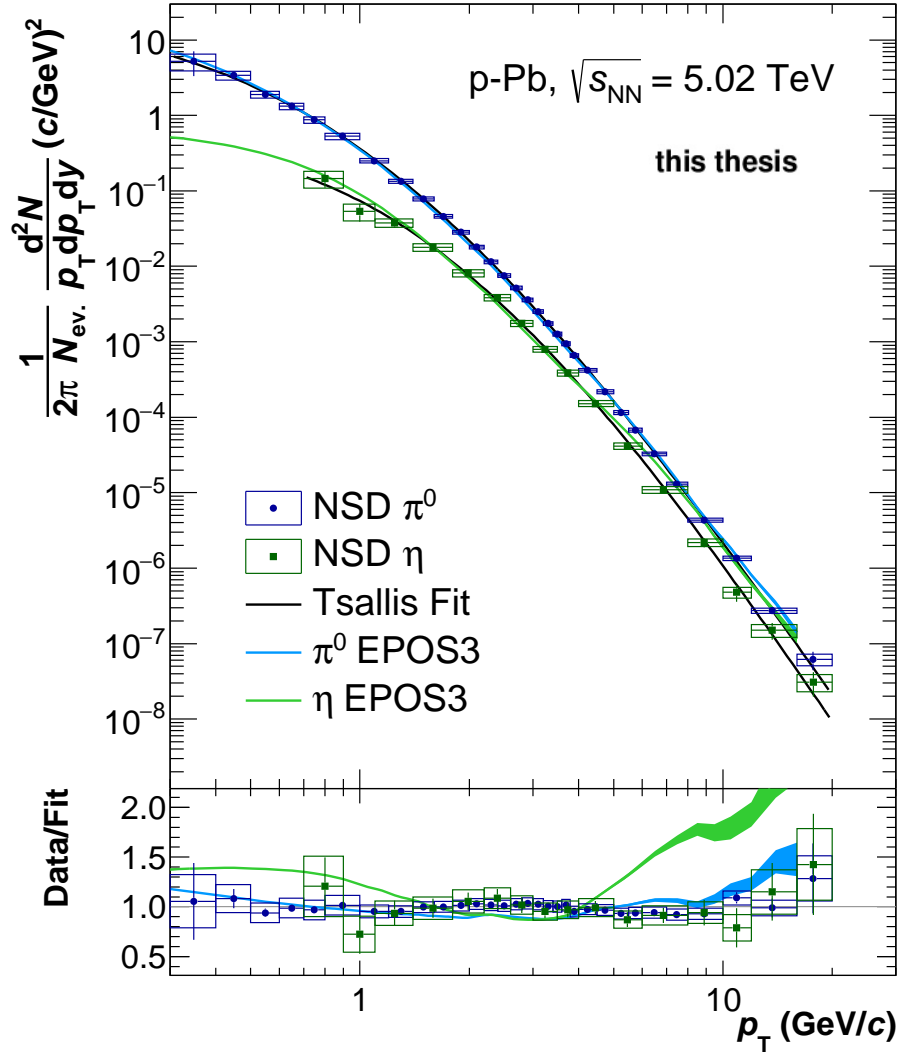
Figure 6.5: The π^0 and η meson invariant yields in p-Pb collisions at $\sqrt{s_{NN}} = 5.02$ TeV compared to EPOS3 model calculations.
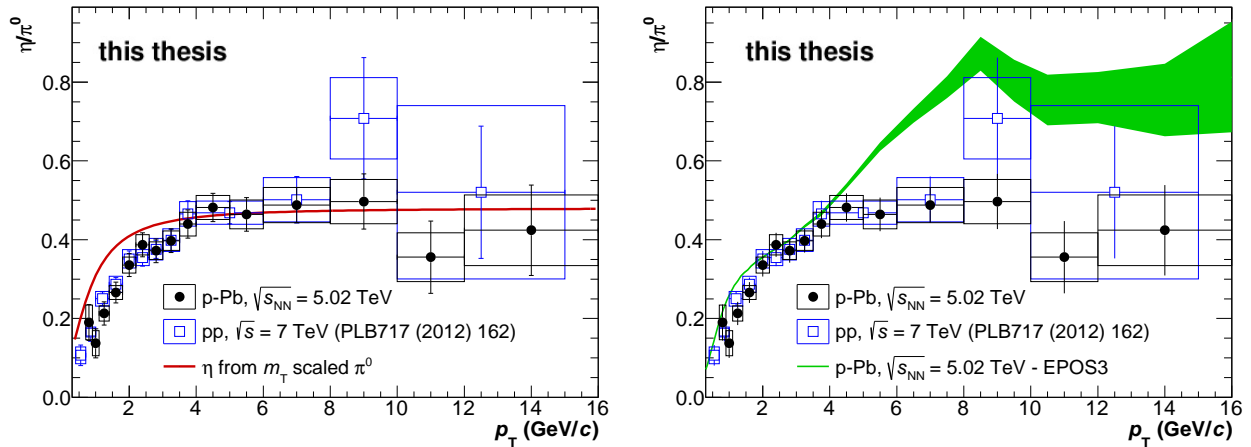
Figure 6.6: The η/π^0 ratio in p-Pb collisions compared to that in pp collisions at $\sqrt{s} = 7$ TeV (left) and comparison to EPOS3 model calculations with statistical errors (right).

and the collision energy.

Moreover, the data is compared to the η/π^0 ratio with m_{T} scaling (transverse mass: $m_{\mathrm{T}} = \sqrt{p_{\mathrm{T}}^2 + m^2}$) [70]. Identified particle spectra are described successfully by a universal parameterization. This phenomenon is known as m_{T} scaling. The Tsallis fit to the combined π^0 yield is used as parameterization and the η meson yield is calculated as

$$E\frac{\mathrm{d}^3 N^\eta}{\mathrm{d}p^3} = C_m \cdot f_{\pi^0}(\sqrt{p_{\mathrm{T}}^2 + m_\eta^2}) \tag{6.2}$$

with an absolute normalization factor $C_m = 0.48 \pm 0.03$. The shown ratio is the fraction of this m_{T} scaled η meson yield and the π^0 with the Tsallis fit. The m_{T} scaling curve has good description of measured ratio above 4 GeV/c, but discrepancy between measured ratio and the m_{T} scaling is observed in low-p_{T} region. Therefore measured η meson yield especially at low-p_{T} is crucial as m_{T} scaling from the measured π^0 yield fails to describe the η meson correctly. Comparison to EPOS3 model calculations is shown in the right of Fig.6.6. The model calculation is good description for data in low-p_{T} region and is closer than the m_{T} scaling prediction. However, it continues to increasing instead of reaching a plateau behavior observed in data. This model is nonetheless able to describe the charged pions and charged kaons spectra.

6.3 Nuclear modification factor

The modification of the hadron yields for different p_{T} intervals in p-Pb collisions with respect to pp collisions can be quantified with the nuclear modification factor,

$$R_{\mathrm{pPb}}(p_{\mathrm{T}}) = \frac{\mathrm{d}^2 N/\mathrm{d}p_{\mathrm{T}}\mathrm{d}y|_{\mathrm{pPb}}}{\langle T_{\mathrm{pPb}}\rangle \times \mathrm{d}^2\sigma/\mathrm{d}p_{\mathrm{T}}\mathrm{d}y|_{\mathrm{pp}}}, \tag{6.3}$$

where the nuclear overlap function $\langle T_{\mathrm{pPb}} \rangle$ is related to the average number of inelastic proton-nucleon collisions, calculated by applying the Glauber model, which gives

$$\langle T_{\mathrm{pPb}} \rangle = \langle N_{\mathrm{coll}} \rangle / \sigma_{\mathrm{NN}} = 0.0983 \pm 0.0035 \, \mathrm{mb}^{-1}, \tag{6.4}$$

with the number of binary nucleus-nucleus collisions $\langle N_{\mathrm{coll}} \rangle = 6.9 \pm 0.7$ and the production cross section in pp collisions $\sigma_{\mathrm{NN}} = 70 \pm 5$ mb [22]. There is no reconstructed pp spectrum for referenced π^0 cross section at $\sqrt{s} = 5.02$ TeV. So we calculated it by interpolation of invariant π^0 cross section in pp collisions at $\sqrt{s} = 2.76$ TeV and 7 TeV.

It is found out that the $\sqrt{s} = 7$ TeV data still includes some pile-up influence which is not known at the time of the publication. The pile-up effect for the interpolated π^0 spectrum and the π^0 R_{pPb} is estimated. For PHOS measurement, it is assumed $\sqrt{s} = 7$ TeV π^0 spectrum has -5 % difference at a maximum by influence of pile-up correction, and added -5 % uniformly to the π^0 spectrum in pp collisions at $\sqrt{s} = 7$ TeV. The interpolated π^0 spectrum with pile-up correction has about 3 % difference as compared to one without pile-up correction in Fig.6.7. The π^0 R_{pPb} which is calculated by the interpolated spectrum with and without adding -5 % as assumption of pile-up correction has about 3 % difference, shown in Fig.6.8. In the result of estimation for pile-up correction, the pile-up effect is less than about 25 % of the systematic uncertainty and is within the statistical uncertainty. The pile-up effect on the R_{pPb} is even smaller. In addition, the pile-up effect is also considered from another approach by PCM measurement. The ratio between the invariant π^0 cross section in pp collisions at $\sqrt{s} = 7$ TeV with and without applied pile-up correction is shown in Fig.6.9. Except for the very low-p_{T} part, the differences on the PCM R_{pPb} are of the order of 2 % which is well covered within the systematic uncertainties. As the pile-up effect mainly influences the lowest p_{T} region, it has been decided to reject this part in the combined R_{pPb} and perform a cut at 1 GeV/c.

In the estimation of interpolated π^0 spectrum as input, it is fitted the π^0 cross section in pp collisions at $\sqrt{s} = 2.76$ TeV and 7 TeV in each p_{T} bin by a function of power law $f(x) = A \times x^B$ where A and B are free parameters. Evaluated the π^0 cross section at $\sqrt{s} = 5.02$ TeV is shown in Fig.6.10. The referenced data to calculate the interpolated spectrum for the PHOS measurement is used π^0 spectrum measured by PHOS only, not combined π^0 spectrum. Figure 6.11 shows the interpolated π^0 cross section at $\sqrt{s} = 5.02$ TeV and the π^0 cross section at $\sqrt{s} = 2.76$ TeV and 7 TeV. The π^0 R_{pPb} is calculated individually in each method and combined them to the final result of R_{pPb} instead of calculating the combined R_{pPb} directly from the combined π^0 spectrum. The PHOS part of the published pp spectra is used as input for the reconstruction of the PHOS pp reference, and the PCM part of the published pp spectra is used as input for that of the PCM pp reference. As there is no own pp reference for the EMCal and PCM-Dalitz analyses, the combined PHOS and PCM published pp spectra are used as input for EMCal, and the PCM part of the published pp spectra are used as input for PCM-Dalitz which allows to partially cancel out the material budget uncertainty. This approach has advantages. For the PHOS analysis, uncertainties for the material budget, non-linearity and global energy scale partially cancel out. For PCM analysis, the material budget uncertainty completely cancels out. The individual π^0 R_{pPb} measured by different methods are shown in Fig.6.12 For the combination of the individual R_{pPb}, the same procedure is used as for the combined meson spectra. The result of combined R_{pPb} is shown in Fig.6.13. The uncertainties of the p-Pb and pp spectra are added in quadrature, separately for the statistical and systematic uncertainties. The uncertainty of the T_{pPb} is shown as overall normalization uncertainty
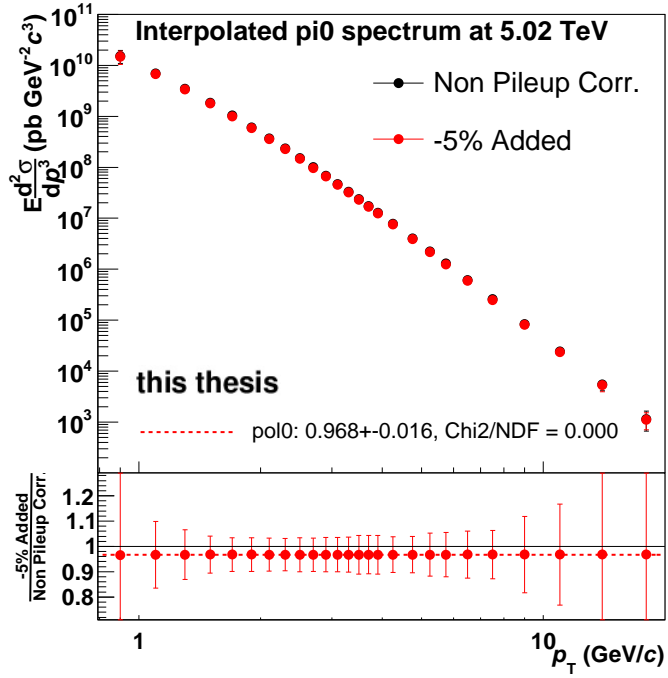
Figure 6.7: Comparison of the interpolated π^0 spectrum between with and without pile-up correction
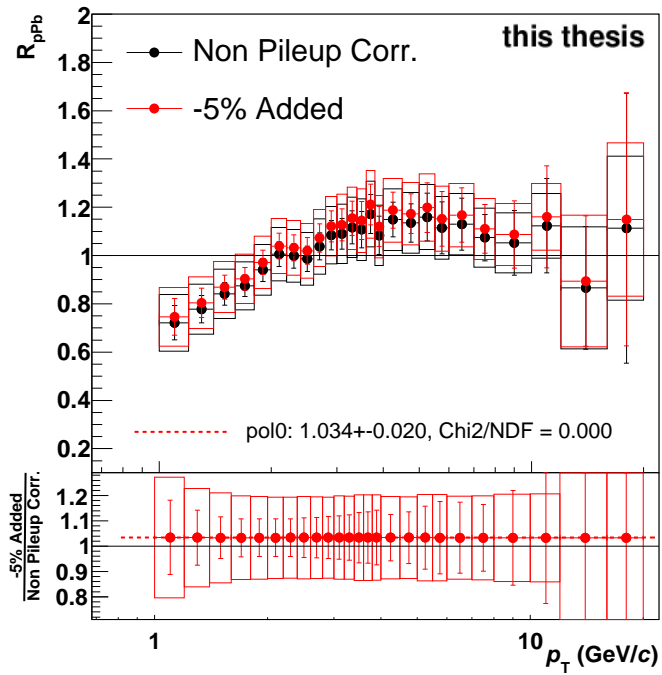

Figure 6.8: Comparison of the π^0s R_{pPb} between with and without pile-up correction
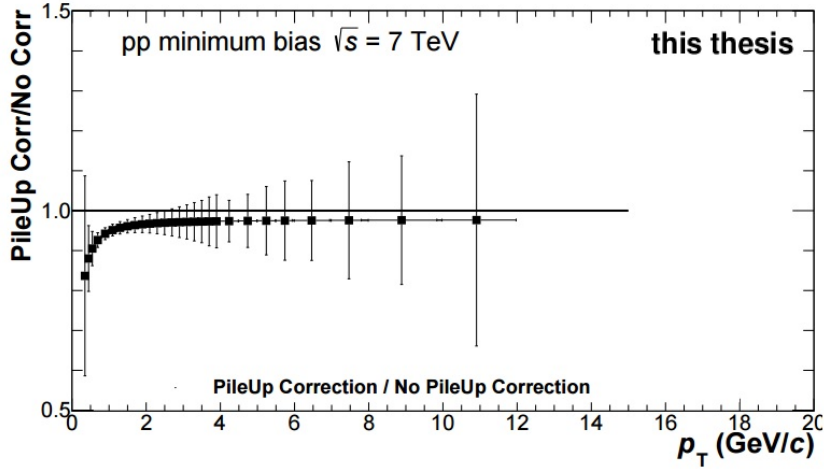
87

Figure 6.9: Ratio between the pp collisions at $\sqrt{s} = 7$ TeV invariant π^0 cross section with and without applied pile-up correction.

represented as blue box around unity at low-p_T. As described before, the combined R_{pPb} is not shown below a p_T of 1 GeV/c due to the missing pile-up correction in the published pp data at $\sqrt{s} = 7$ TeV. The π^0 R_{pPb} increases with p_T in the low-p_T region and consists with unity at $p_T > 2$ GeV/c within uncertainties. At the low-p_T region ($p_T < 3$ GeV/c), R_{pPb} increment at low-p_T is attributed to a soft physics (N_{part} scaling) not due to N_{coll} scaling. It seems that there is a slight enhancement (less than 10 %) of the Cronin effect at $p_T \sim 3 - 4$ GeV/c due to initial-state multiple scattering or anti-shadowing. The result that R_{pPb} consists with unity indicates that particles production in p-Pb collisions can be explained by that scaled in pp collisions. Therefore there is negligible or no system size dependence in collision for the initial-state effects to modify p_T-spectrum of the π^0.

For comparison, Fig.6.14 presents the R_{pPb} calculated with combined π^0 spectrum as input. At the time of verifying this difference, it was not fully considered canceling the systematic uncertainties. We focus only on the difference of their magnitudes. The results for two approaches (one is method using combined π^0 p-Pb spectrum and published pp spectrum and another is method using individual R_{pPb} and combining them) are agreement.

In Fig.6.15 and 6.16, the nuclear modification factor for π^0 in p-Pb collisions is compared to the nuclear modification factor for $\pi^\pm$ [71] and charged particles [22] in p-Pb collisions at $\sqrt{s_{NN}} = 5.02$ TeV and also to that for π^0 [2] and $\pi^\pm$ [36] in central ($0 - 5$ % centrality) Pb-Pb collisions at $\sqrt{s_{NN}} = 2.76$ TeV. The π^0 R_{pPb} is good agreement with the R_{pPb} for $\pi^\pm$ and charged particles for the entire p_T range. It means that the π^0, $\pi^\pm$ and charged particles have same production mechanism. Strong suppression of high-p_T π^0 observed in central Pb-Pb collisions is not observed in π^0 measurement in p-Pb collisions at $\sqrt{s_{NN}} = 5.02$ TeV.

Figure 6.17 represents comparison of R_{pPb} and R_{dAu} for π^0 in d-Au collisions at $\sqrt{s_{NN}} = 200$ GeV with minimum bias trigger measured by RHIC-PHENIX. There is no obvious difference between R_{pPb} and R_{dAu} for π^0.
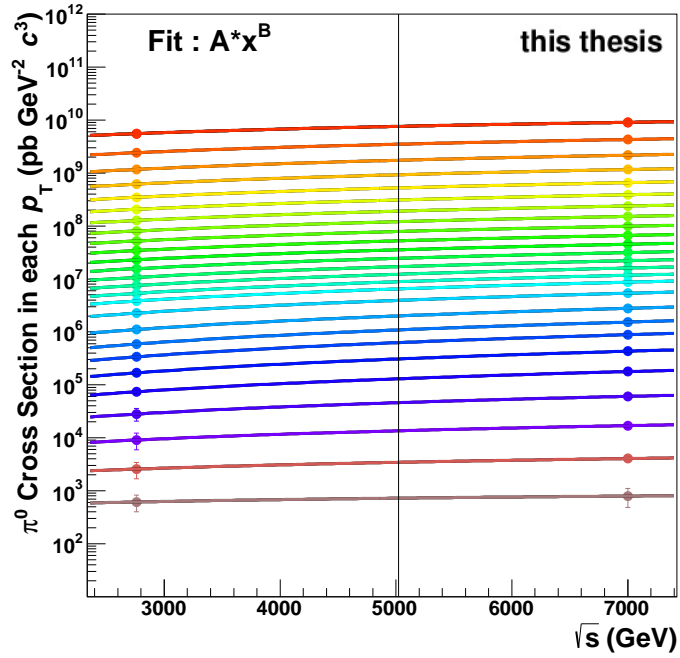
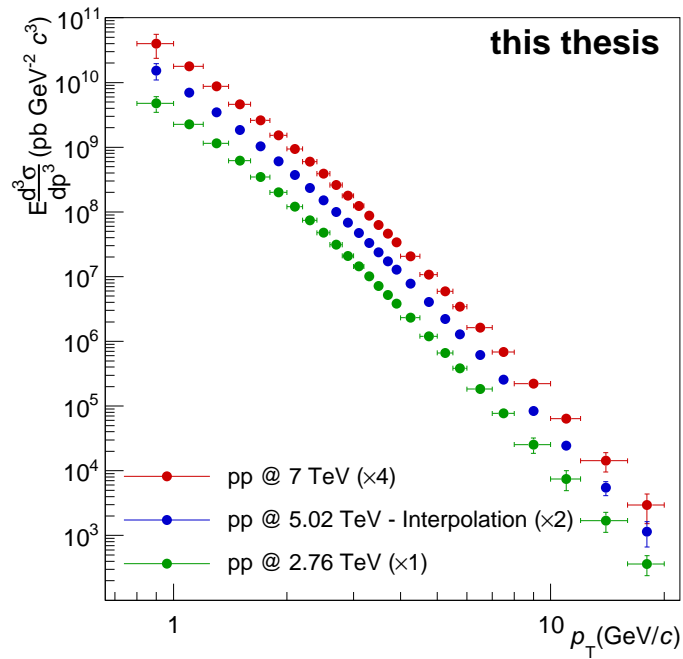Figure 6.10: $\sqrt{s}$ dependence of the π^0 cross section in pp collisions

Figure 6.11: The interpolate π^0 cross section in pp collisions at $\sqrt{s} = 5.02$ TeV together with the cross sections in pp collisions at 2.76 TeV and 7 TeV.
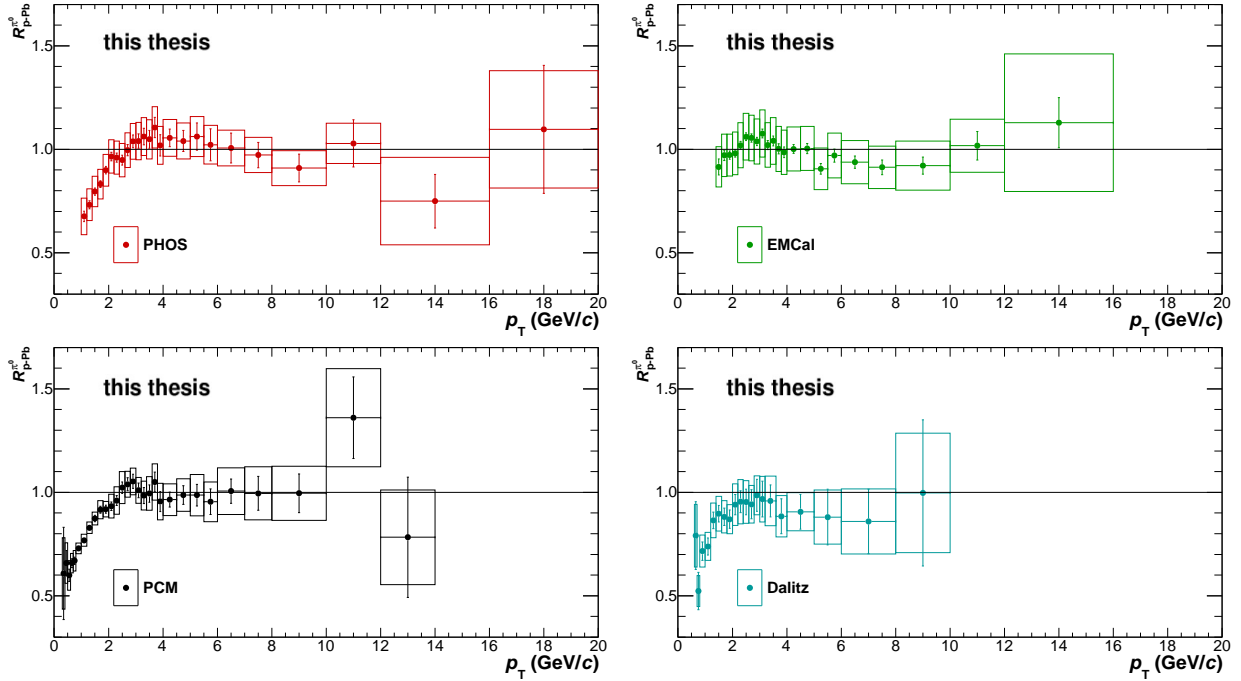
Figure 6.12: The π^0 R_{pPb} at $\sqrt{s_{NN}} = 5.02$ TeV measured by PHOS (top left), EMCal (top right), PCM (bottom left) and PCM-Dalitz (bottom right).
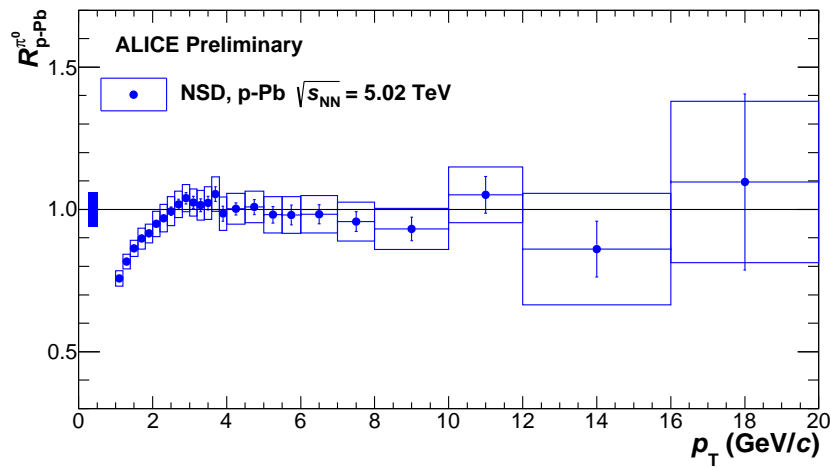

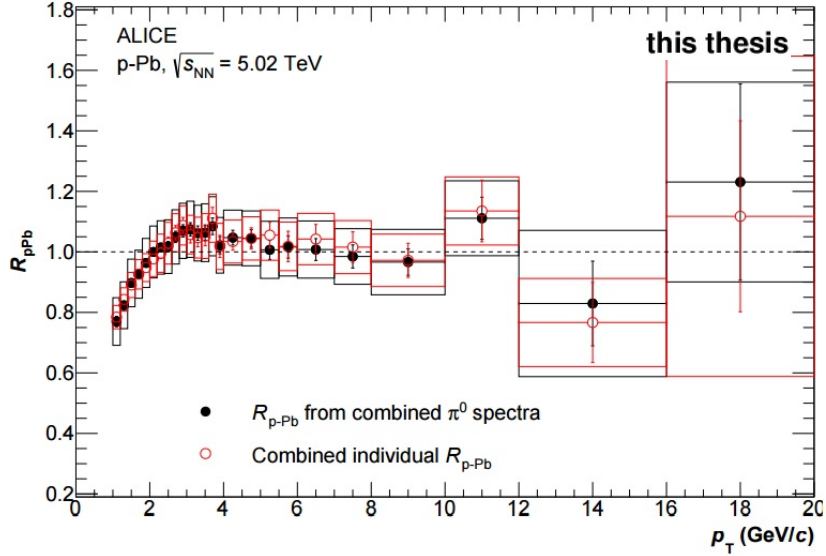Figure 6.13: The combined nuclear modification factor R_{pPb} for π^0

Figure 6.14: Difference between combined individual R_{pPb} and R_{pPb} from combined π^0 spectra

The π^0 R_{pPb} is compared to pQCD NLO model predictions in Fig.6.18. The predictions are calculated by EPS09s that is a set of spatially dependent nPDFs and three different FF: KKP [72], AKK [73], fDSS [74] which do not lead to a significant difference in the R_{pPb}. KKP is FF for $\pi^{\pm}$, $\mathrm{K}^{\pm}$ and proton at both LO and NLO calculations, AKK is FF for $\pi^{\pm}$, $\mathrm{K}^{\pm}$, proton, anti-proton, K^0_s and $\Lambda/\bar{\Lambda}$ at NLO calculation, and fDSS is FF for π^0, $\pi^{\pm}$, $\mathrm{K}^{\pm}$ and K^0_s at NLO calculation with their uncertainties. The CGC calculation is able to reproduce the R_{pPb}. All shown model predictions describe the data satisfactorily although the data points slightly exceed both predictions for intermediate-p_{T} region, $2 - 4$ GeV/c. So there may be a small enhancement, not visible when comparing to unity, but compared to the models that do not predict the R_{pPb} being at one in this p_{T} region. Therefore I conclude the suppression observed in Pb-Pb collisions comes from final-state effects such as hot and dense matter rather than initial-state effects.
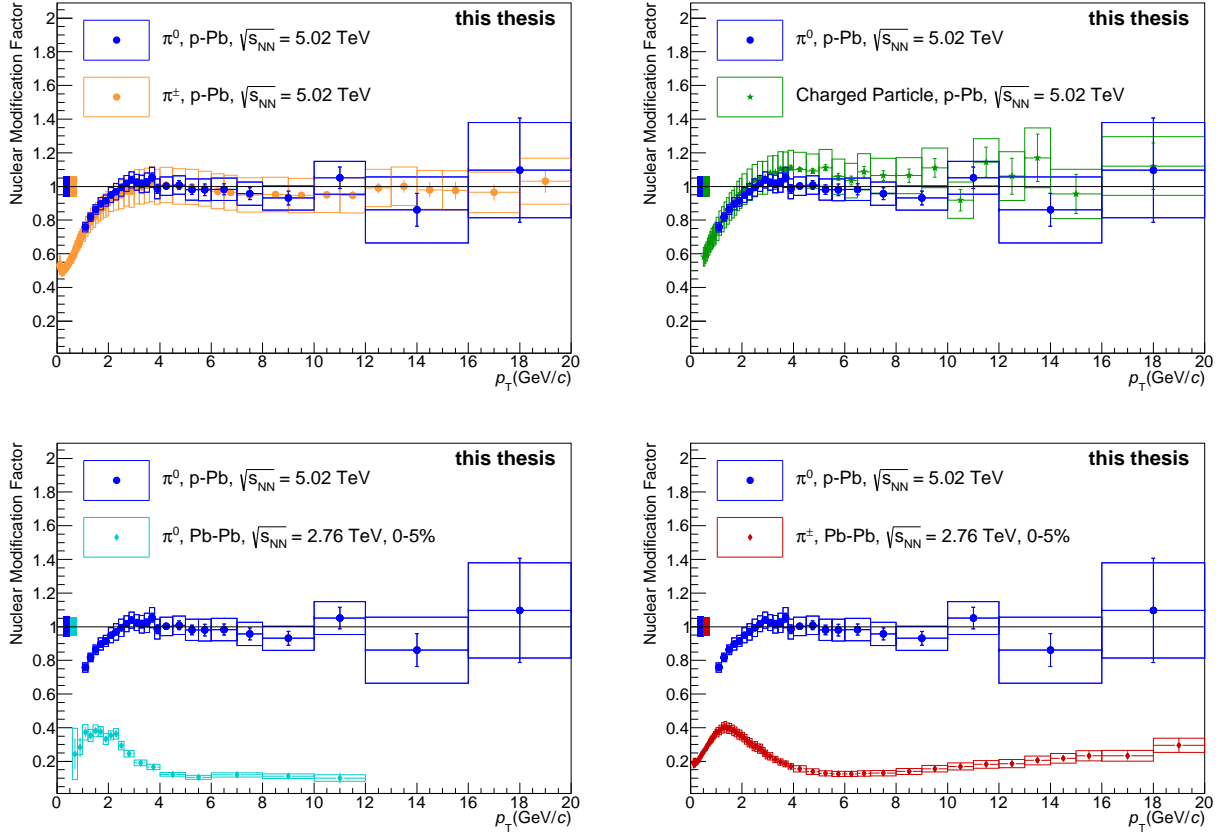
Figure 6.15: The π^0 nuclear modification factor in p-Pb collisions as compared to other particles with different collision system and energy in ALICE
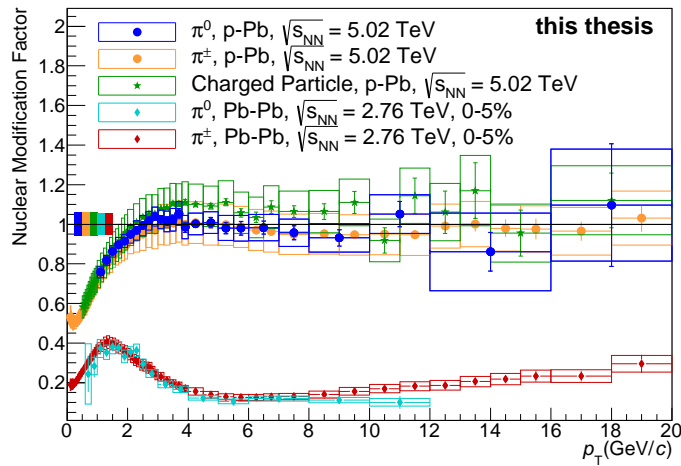

Figure 6.16: Summary of the π^0 nuclear modification factor in p-Pb collisions as compared to other particles with different collision system and energy in ALICE
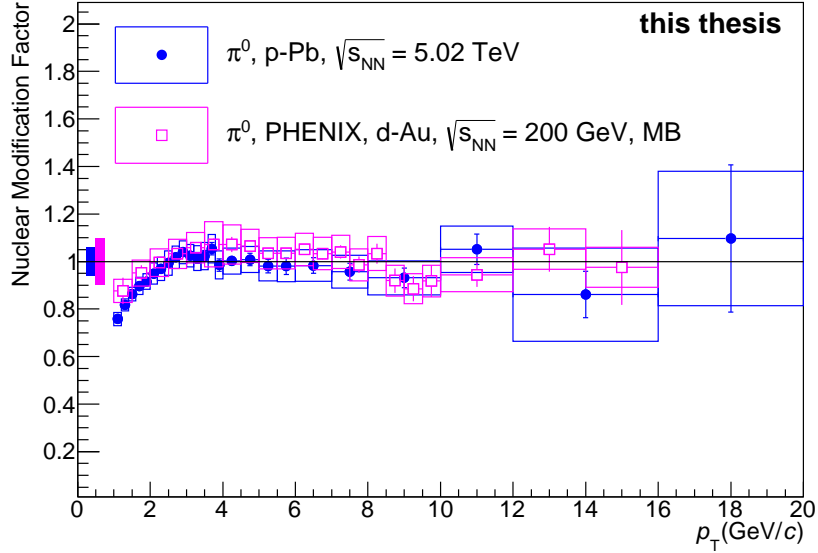
Figure 6.17: Comparison of π^0 R_{pPb} by ALICE and π^0 R_{dAu} by RHIC-PHENIX
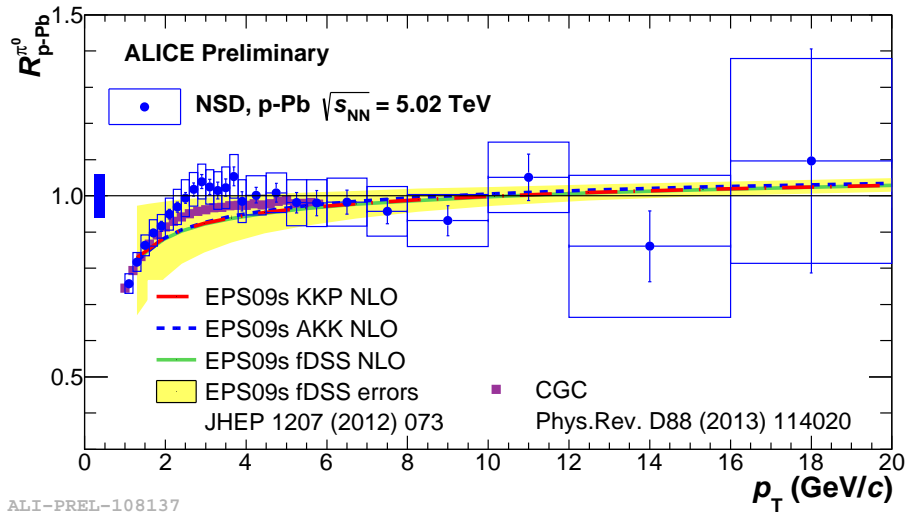

Figure 6.18: The π^0 R_{pPb} compared to pQCD NLO calculation using the nPDF EPS09s and three different FF (KKP, AKK, and fDSS) and CGC prediction. The yellow band corresponds to the uncertainties calculated using only fDSS.

Chapter 7

Conclusion

This paper presents measurement of the π^0 and η meson production in p-Pb collisions at $\sqrt{s_{NN}} = 5.02$ TeV and the nuclear modification factor (R_{pPb}) for π^0 from the LHC-ALICE experiment for the first time. The π^0 invariant yield is measured in p_T range of $0.3 - 20$ GeV/c by individual four methods via the ALICE electromagnetic calorimeters, PHOS and EMCal, and photon conversion methods (PCM and PCM-Dalitz), and the η meson invariant yield is measured in p_T range of $0.7 - 20$ GeV/c via EMCal and PCM. I contributed to this analysis via using the PHOS detector. The final spectra are achieved via combination of individual analyses with weight according to their uncertainties. Both π^0 and η meson invariant yields are a nice agreement by the Tsallis fit and all measurements are consistent with each other within the uncertainties. The EPOS3 event generator reproduces well in the almost entire p_T region for π^0 and the intermediate-p_T region for η meson. But it does not describe high-p_T region ($p_T > 10$ GeV/c) for both π^0 and η meson.

The η/π^0 ratio increases at $p_T < 4$ GeV/c and arrives a plateau of 0.47 ± 0.02 at $p_T > 4$ GeV/c. It is consistent with the ALICE pp and Pb-Pb measurements and the world results. The m_T scaling for the η/π^0 ratio is good description at $p_T > 4$ GeV/c, but the discrepancy is observed in low-p_T region. The EPOS3 generator is good reproduction for data in low-p_T region and is closer than the m_T scaling prediction. But it fails to reproduce data in high-p_T region.

The π^0 nuclear modification factor in p-Pb collisions increases in low-p_T region and consists with unity at $p_T > 2$ GeV/c. It is not observed particle yield suppression as observed in Pb-Pb collisions and system size dependence for the initial-state effects to modify p_T-spectrum of the π^0. In addition, the π^0 nuclear modification factor in p-Pb collisions at LHC energy and in d-Au collisions at RHIC energy have no obvious difference. Theoretical model via using EPS09s NLO calculations and CGC model calculation are able to describe R_{pPb}. These results provide direction that strong suppression of high-p_T π^0 observed in Pb-Pb collisions comes from final-state effects due to parton energy loss in the hot QCD medium rather than initial-state effects.

However, in this time, I studied about the π^0 measurement in p-Pb collisions with only minimum bias triggered data and am unaware of data with high energy photon triggered events, high multiplicity events and different centrality classes, especially most central collisions due to a lack of statistics and small detector acceptance. Since operation of the LHC-Run2 has started from the Spring of 2015, the ALICE experiment has recorded data with LHC full energy, in pp collisions at $\sqrt{s} = 13$ TeV, in p-Pb collisions at $\sqrt{s_{NN}} = 8$ TeV and in Pb-Pb collisions at $\sqrt{s_{NN}} = 5.02$ TeV.

Moreover all detectors are restored and improved. The PHOS detector improved readout speed so that it can be accommodated to high rate data taking and also achieved wide acceptance by installing additional half module. I expect the LHC-Run2 data enables more precise measurements in distinguishing events as described above.

Acknowledgments

Bibliography

[1] S. Borsanyi, G. Endrodi, Z. Fodor, A. Jakovac, S. D. Katz, *et al.*, "The QCD equation of state with dynamical quarks", JHEP **11** 077 (2010), arXiv:1007.2580 [hep-lat]

[2] **ALICE** Collaboration, "Neutral pion production at midrapidity in pp and PbPb collisions at $\sqrt{s_{NN}} = 2.76$ TeV", Eur. Phys. J. **C74** 3108 (2014), arXiv:1405.3794 [nucl-ex]

[3] **PHENIX** Collaboration, "Suppression Pattern of Neutral Pions at High Transverse Momentum in Au + Au Collisions at $\sqrt{s_{NN}} = 200$ GeV and Constraints on Medium Transport Coefficients", Phys. Rev. Lett. **101** 232301 (2008)

[4] **PHENIX** Collaboration, "Evolution of π^0 Suppression in Au + Au Collisions from $\sqrt{s_{NN}} = 39$ to 200 GeV", Phys. Rev. Lett. **109** 152301 (2012)

[5] **WA98** Collaboration, "Suppression of High-p_T Neutral Pion Production in Central Pb + Pb Collisions at $\sqrt{s_{NN}} = 17.3$ GeV Relative to p + C and p + Pb Collisions", Phys. Rev. Lett. **100** 242301 (2008)

[6] C. A. Salgado *et al.* , "Proton-nucleus collisions at the LHC: scientific opportunities and requirements", CERN-PH-TH-/2011-119, LHC-Project-Report-1181, arXiv:1105.3919 [hep-ph]

[7] Particle Adventure supported by the Particle Data Group of the Lawrence Berkeley National Laboratory (LBNL), "History of the Universe Poster", http://particleadventure.org/

[8] K. Fukushima and T. Hatsuda, "The phase diagram of dense QCD", Rept. Prog. Phys. **74** 014001 (2011), arXiv:1005.4814 [hep-ph]

[9] F. Karsch, "Recent lattice results on finite temperature and density QCD, part I", PoS CPOD07, 026 (2007), arXiv:0711.0656 [hep-lat]

[10] T. K. Nayak, "Heavy Ions: Results from the Large Hadron Collider", J. Phys. **79** 719-735 (2012), arXiv:1201.4264 [nucl-ex]

[11] K.J. Eskola, V.J. Kolhinen and C.A. Salgado, "The scale dependent nuclear effects in parton distributions for practical applications", Eur. Phys. J. **C9** 61-68 (1999), arXiv:hep-ph/9807297

[12] **PHENIX** Collaboration, "Centrality Dependence of π^0 and η Production at Large Transverse Momentum in $\sqrt{s_{NN}} = 200$ GeV d + Au Collisions", Phys. Rev. Lett. **98** 172302 (2007)

[13] T. Lappi, H. Mäntysaari, "Single inclusive particle production at high energy from HERA data to proton-nucleus collisions", Phys. Rev. **D88** 114020 (2013), arXiv:1309.6963 [hep-ph]

[14] F. Gelis, E. Iancu, J. Jalilian-Marian and R. Venugopalan, "The Color Glass Condensate", Annu. Rev. Nucl. Part. Sci. **60** 463-489 (2010)

[15] K. J. Eskola. H. Ponkkunen and C. A. Salgado, "EPS09 - A new generation of NLO and LO nuclear parton distribution functions", JHEP **04** (2009) 065, arXiv:0902.4154 [hep-ph]

[16] I. Helenius, K. J. Eskola, H. Honkanen and C. A. Salgado, "Impact-parameter dependent nuclear parton distribution functions: EPS09s and EKS98s and their applications in nuclear hard processes", JHEP **07** (2012) 073, arXiv:1205.5359 [hep-ph]

[17] M. Hirai, S. Kumano, and T. H. Nagai, "Determination of nuclear parton distribution functions and their uncertainties at next-to-leading order", Phys. Rev. **C76** 065207 (2007), arXiv:0709.3038 [hep-ph]

[18] D. de Florian and R. Sassot, "Nuclear parton distributions at next to leading order", Phys. Rev. **D69** 074028 (2004), arXiv:hep-ph/0311227

[19] K. Kovarik *et al.* , "nCTEQ15: Global analysis of nuclear parton distributions with uncertainties in the CTEQ framework", Phys. Rev. **D93** 085037 (2016), arXiv:1509.00792 [hep-ph]

[20] J. W. Cronin, H. J. Frisch, M. J. Shochet, J. P. Boymond, P. A. Piroue, and R. L. Sumner, "Production of hadrons at large transverse momentum at 200, 300, and 400 GeV", Phys. Rev. **D11** 3105 (1975)

[21] B. Z. Kopeliovich, J. Nemchik, A. Schafer, and A. V. Tarasov, "Cronin Effect in Hadron Production Off Nuclei", Phys. Rev. Lett. **88** 232303 (2002), arXiv:hep-ph/0201010

[22] **ALICE** Collaboration, "Transverse Momentum Distribution and Nuclear Modification Factor of Charged Particles in $p + $ Pb Collisions at $\sqrt{s_{NN}} = 5.02$ TeV", Phys. Rev. Lett. **110** 082302 (2013)

[23] M. L. Miller, K. Reygers, S. J. Sanders and P. Steinberg, "Glauber Modeling in High Energy Nuclear Collisions", Ann. Rev. Nucl. Part. Sci. **57** 205-243 (2007), arXiv:nucl-ex/0701025

[24] K.Werner, B. Guiot, Iu.Karpenko and T.Pierog, "Analysing radial flow features in p-Pb and p-p collisions at several TeV by studying identified particle production in EPOS3", Phys. Rev. **C89** 064903 (2014), arXiv:1312.1233 [nucl-th]

[25] S. Campbell, "Photon production from gluon mediated quark-anti-quark annihilation at confinement", Phys. Rev. **C92** 014907 (2015), arXiv:1504.01654 [nucl-ex]

[26] J. Kapusta, P. Lichard and D. Seibert, "High-energy photons from quark-gluon plasma versus hot hadronic gas", Phys. Rev. **D44** 2774 (1991)

[27] **Particle Data Group** Collaboration, "Review of Particle Physics", Chin. Phys. **C40** 100001 (2016), http://www-pdg.lbl.gov/

[28] **STAR** Collaboration, "Evidence from d+Au Measurements for Final-State Suppression of High-p_T Hadrons in Au+Au Collisions at RHIC", Phys. Rev. Lett. **91** 072304 (2003), arXiv:nucl-ex/0306024

[29] **ALICE** Collaboration, "Centrality dependence of particle production in p - Pb collisions at $\sqrt{s_\mathrm{NN}} = 5.02$ TeV", Phys. Rev. **C91** 064905 (2015)

[30] B. Alver, M. Backer, C. Loinzides, and P. Steinberg, "The PHOBOS Glauber Monte Carlo", arXiv:0805.4411

[31] M. L. Miller, K. Reygers, S. J. Sanders, and P. Steinberg, "Glauber Modeling in High-Energy Nuclear Collisions", Ann. Rev. Nucl. Part. Sci. **57** 205-243 (2007)

[32] **ALICE** Collaboration, "Neutral pion and η meson production in proton-proton collisions at $\sqrt{s} = 0.9$ TeV and $\sqrt{s} =$ 7 TeV", Phys. Lett. **B717** 162-172 (2012)

[33] K. Reygers for the **ALICE** Collaboration, "Production of Neutral Pions and Eta-mesons in pp Collisions Measured with ALICE" (QM2011 Proceedings), J. Phys. **G38** 124076 (2011) arXiv:1106.5932 [hep-ex]

[34] A. Morreale on behalf of the **ALICE** collaboration, "Measurement of neutral mesons in pp and Pb-Pb collisions at mid-rapidity with ALICE" (QM2015 Proceedings), Nucl. Phys. **A956** 645-648 (2016), arXiv:1512.05250

[35] D. de Florian, R. Sassot, M. Epele, R. J. Hernández-Pinto and M. Stratmann, "Parton-to-pion fragmentation reloaded", Phys. Rev. **D91** 014035 (2015)

[36] **ALICE** Collaboration, "Production of charged pions, kaons and protons at large transverse momenta in pp and Pb-Pb collisions at $\sqrt{s_\mathrm{NN}} = 2.76$ TeV", Phys. Lett. **B736** 196-207 (2014)

[37] **ALICE** Collaboration, "Direct photon production in Pb-Pb collisions at $\sqrt{s_\mathrm{NN}} = 2.76$ TeV", Phys. Lett. **B754** 235-248 (2016), arXiv:1509.07324 [nucl-ex]

[38] **PHENIX** Collaboration, "Enhanced Production of Direct Photons in Au + Au Collisions at $\sqrt{s_\mathrm{NN}} = 200$ GeV and Implications for the Initial Temperature", Phys. Rev. Lett. **104** 132301 (2010), arXiv:0804.4168 [nucl-ex]

[39] **PHENIX** Collaboration, "Centrality dependence of low-momentum direct-photon production in Au + Au collisions at $\sqrt{s_\mathrm{NN}} = 200$ GeV", Phys. Rev. **C91** 064904 (2015), arXiv:1405.3940 [nucl-ex]

[40] L. Evans and P. Bryant, "LHC Machine", JINST **3** S08001 (2008)

[41] "CERN Official site", http://home.cern/

[42] "CERN Official site, The accelerator complex", https://home.cern/about/accelerators

[43] "ALICE experiment official site" http://aliceinfo.cern.ch

[44] **ALICE** Collaboration, "ALICE Technical Design Report of the Inner Tracking System (ITS)", CERN / LHCC 99-12

[45] **ALICE** Collaboration, "The ALICE Experiment at the CERN LHC", JINST **3** S08002 (2008)

[46] **ALICE** Collaboration, "ALICE Technical Design Report of the Photon Spectrometer (PHOS)", CERN / LHCC 99-04

[47] D.V. Aleksandrov *et al.* (**ALICE PHOS-calorimeter** collaboration), "A high resolution electromagnetic calorimeter based on lead-tungstate crystals", Nuclear Instruments and Methods in Phys. Res. **A550** 169-184 (2005)

[48] **ALICE** Collaboration, "ALICE Electromagnetic Calorimeter Technical Design Report", CERN / LHCC 2008-014

[49] **ALICE** Collaboration, "ALICE Technical Design Report of the Inner Tracking System (ITS)" CERN / LHCC 99-12

[50] "The ALICE Time Projection Chamber web page", http://alice-tpc.web.cern.ch/content/alice-time-projection-chamber

[51] **ALICE** Collaboration, "ALICE Technical Design Report on Forward Detectors: FMD, T0 and V0" CERN / LHCC 2004-025

[52] **ALICE** Collaboration, "Performance of the ALICE VZERO system", JINST **8** P10016 (2013)

[53] **ALICE** Collaboration, "ALICE TWiki Home Page", https://twiki.cern.ch/twiki/bin/view/ALICE/WebHome

[54] **ALICE** Collaboration. "Pseudorapidity Density of Charged Particles in $p + $ Pb Collisions at $\sqrt{s_{NN}} = 5.02$ TeV", Phys. Rev. Lett. **110** 032301 (2013)

[55] **ALICE** Collaboration, "Measurement of inelastic, single- and double-diffraction cross sections in proton-proton collisions at the LHC with ALICE", Eur. Phys. J. **C73** 2456 (2013)

[56] **ALICE** Internal Analysis Note No.21, "Data quality assessment for the ALICE PHOS detector", https://aliceinfo.cern.ch/Notes/node/21

[57] **ALICE** Internal Analysis Note No.173, "Analysis of π^0 production in pp collisions at $\sqrt{s} = 900$ GeV and 7 TeV measured with ALICE PHOS", https://aliceinfo.cern.ch/Notes/node/173

[58] **ALICE** Collaboration, "Centrality dependence of charged particle production at large transverse momentum in Pb-Pb collisions at $\sqrt{s_{\mathrm{NN}}} = 2.76$ TeV", Phys. Lett. **B720** 52-62 (2013)

[59] **ALICE** Internal Analysis Note No.467, "Neutral meson measurement with EMCal-EMCal in ALICE in pPb collisions at $\sqrt{s_{\mathrm{NN}}} = 5.023$ TeV", https://aliceinfo.cern.ch/Notes/node/467

[60] **ALICE** Internal Analysis Note No.285, "Neutral meson measurements via photon conversions in p-Pb collisions at $\sqrt{s} = 5.02$ TeV with ALICE at the CERN LHC", http://aliceinfo.cern.ch/Notes/node/285

[61] **ALICE** Internal Analysis Note No.294, "$\pi^0 \to e^+ + e^- + \gamma$ meson measurement with conversions in ALICE in proton-proton collisions at $\sqrt{s} = 7$ and $\sqrt{s} = 2.76$ TeV, and in p-Pb collisions at $\sqrt{s_{\mathrm{NN}}} = 5.02$ TeV at the CERN LHC", http://aliceinfo.cern.ch/Notes/node/294

[62] **ALICE** Collaboration, "Performance of the ALICE experiment at the CERN LHC", Int. J. Mod. Phys. **A29** 1430044 (2014)

[63] **ALICE** Collaboration, "ALICE EMCal Physics Performance Report, volume II", J. Phys. G32 (2006) 1295-2040

[64] T. Matulewicz *et al.* , "Response of BaF2 detectors to photons of 3-50 MeV energy ", Nuclear Instruments and Methods in Phys. Res. **A289** 194-204 (1990)

[65] Norman M. Kroll and Walter Wada, "Internal Pair Production Associated with the Emission of High-Energy Gamma Rays", Phys. Rev. **98** 1355 (1955)

[66] S. Roesler, R. Engel and J. Ranft, "The Monte Carlo Event Generator DPMJET-III", SLAC-PUB-8740

[67] M. Gyulassy and X. N. Wang, "HIJING 1.0: A Monte Carlo program for parton and particle production in high energy hadronic and nuclear collisions", Comput. Phys. Commun. **83** 307 (1994)

[68] **ALICE** Internal Analysis Note No.43, "Inclusive π^0 production in Pb-Pb collisions at $\sqrt{s_{\mathrm{NN}}}$ = 2.76 TeV measured with ALICE PHOS", https://aliceinfo.cern.ch/Notes/node/43

[69] **PHENIX** Collaboration, "High transverse momentum η meson production in $p+p$, $d+$Au, and Au+Au collisions at $\sqrt{s_{\mathrm{NN}}}$ =200 GeV" Phys. Rev. **C75** 024909 (2007)

[70] P. K. Khandai, P. Shukla and V. Singh, "Meson Spectra and m_{T} scaling in $p + p$, $d +$ Au, and Au + Au collisions at $\sqrt{s_{NN}} = 200$ GeV", Phys. Rev. **C84** 054904 (2011)

[71] **ALICE** Collaboration, "Multiplicity dependence of charged pion, kaon, and (anti)proton production at large transverse momentum in p-Pb collisions at $\sqrt{s_{\mathrm{NN}}} = 5.02$ TeV", Phys. Lett. **B760** 720-735 (2016)

[72] B. A. Kniehl, G. Kramer and B. Potter, "Fragmentation Functions for Pions, Kaons, and Protons at Next-to-Leading Order", Nucl. Phys. **B582** 514-536 (2000), arXiv:hep-ph/0010289

[73] S. Albino, B. A. Kniehl and G. Kramer, "AKK Update: Improvements from New Theoretical Input and Experimental Data", Nucl. Phys. **B803** 42-104 (2008), arXiv:0803.2768 [hep-ph]

[74] D. de Florian, R. Sassot and M. Stratmann, "Global analysis of fragmentation functions for pions and kaons and their uncertainties", Phys. Rev. **D75** 114010 (2007), arXiv:hep-ph/0703242

.1 Run list

| Run index	Run number	Run period
0	195344	LHC13b
1	195346	LHC13b
2	195351	LHC13b
3	195389	LHC13b
4	195390	LHC13b
5	195914	LHC13b
6	195478	LHC13b
7	195479	LHC13b
8	195480	LHC13b
9	195481	LHC13b
10	195482	LHC13b
11	195483	LHC13b
12	195529	LHC13c
13	195531	LHC13c
14	195532	LHC13c
15	195566	LHC13c
16	195567	LHC13c
17	195568	LHC13c
18	195592	LHC13c
19	195593	LHC13c
20	195596	LHC13c
21	195633	LHC13c
22	195635	LHC13c
23	195644	LHC13c
24	195673	LHC13c
25	195675	LHC13c
26	195677	LHC13c

.2 Invariant mass distribution
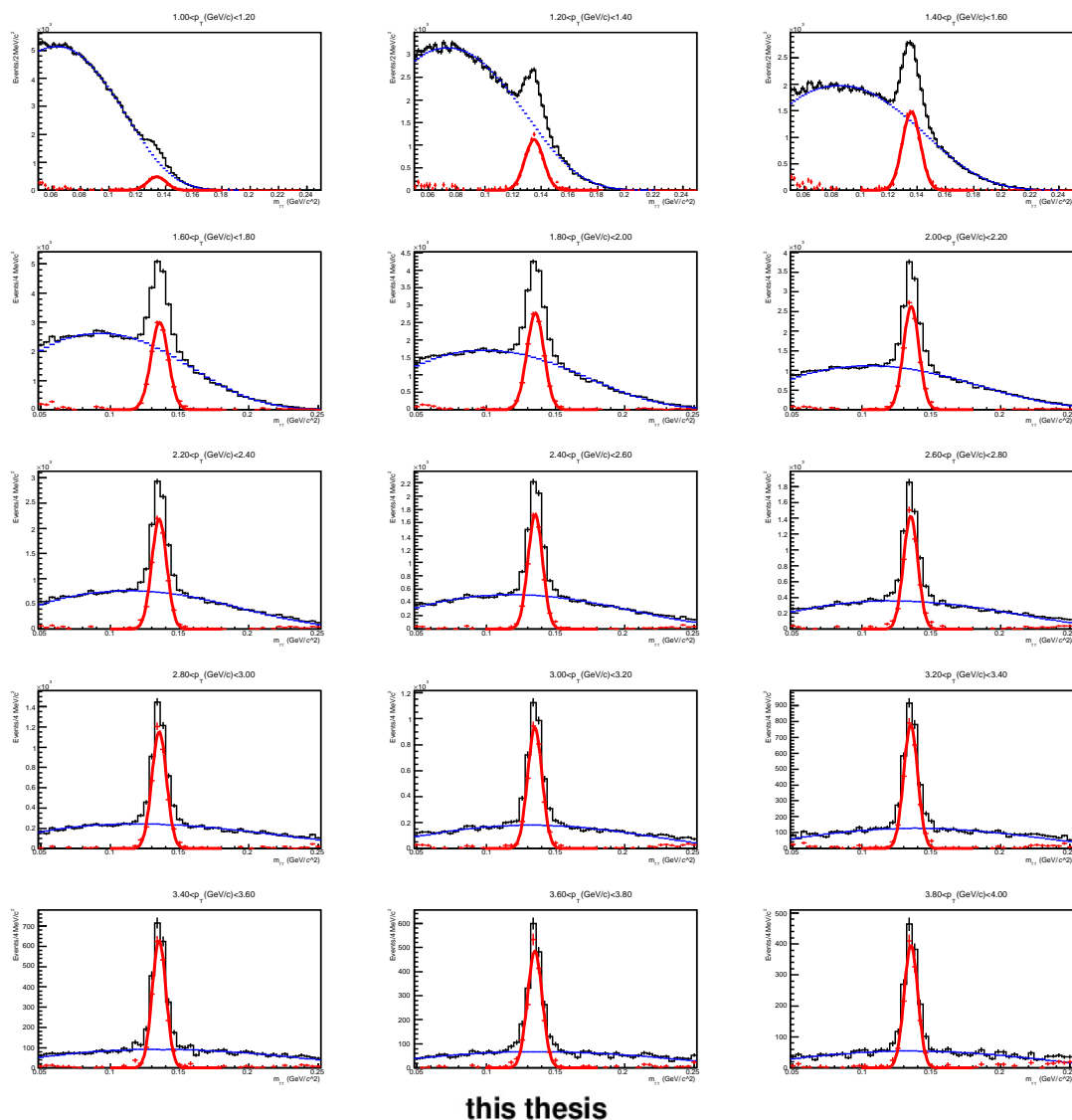
Figure 1: Invariant mass distribution with the Gaussian fit in the real data 1
Signal and background(black line), scaled background estimated by event mixing method(blue),
and signal after background subtraction(red) with the Gaussian fitting in p-Pb collisions at $\sqrt{s_{\mathrm{NN}}}$
= 5.02 TeV
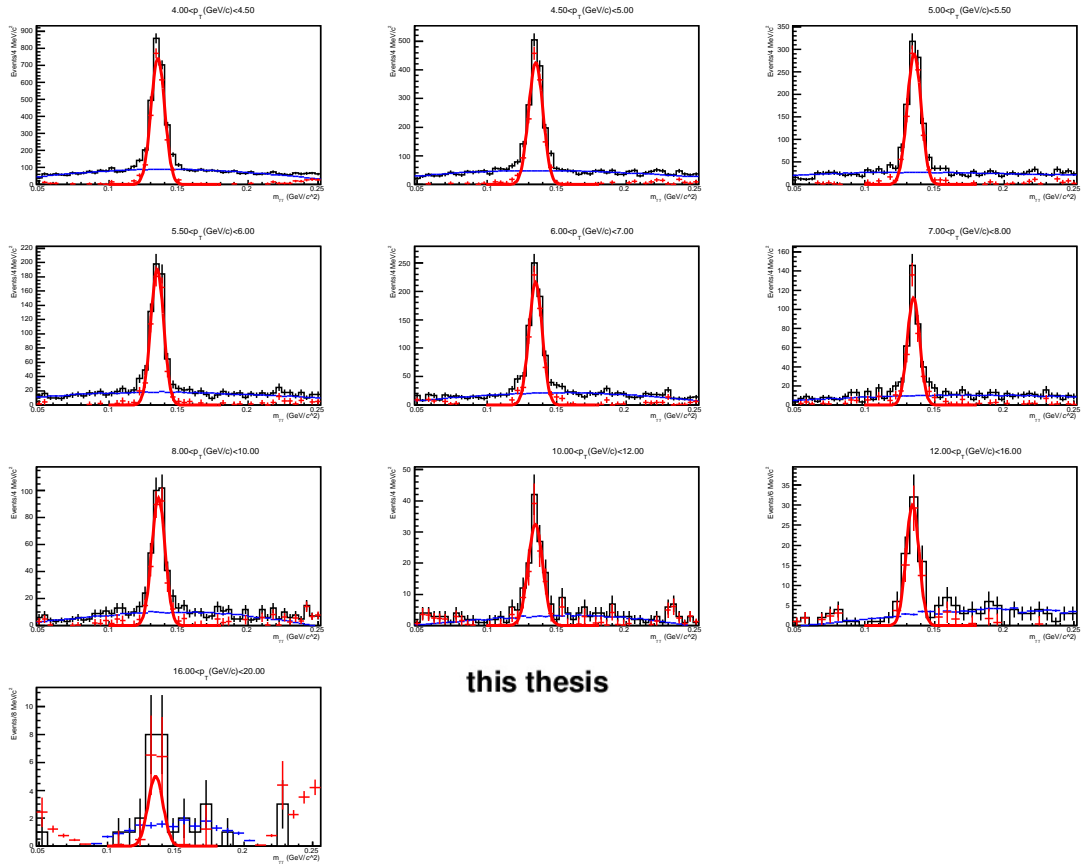
Figure 2: Invariant mass distribution with the Gaussian fit in the real data 2
Signal and background(black line), scaled background estimated by event mixing method(blue),
and signal after background subtraction(red) with the Gaussian fitting in p-Pb collisions at $\sqrt{s_{\mathrm{NN}}}$
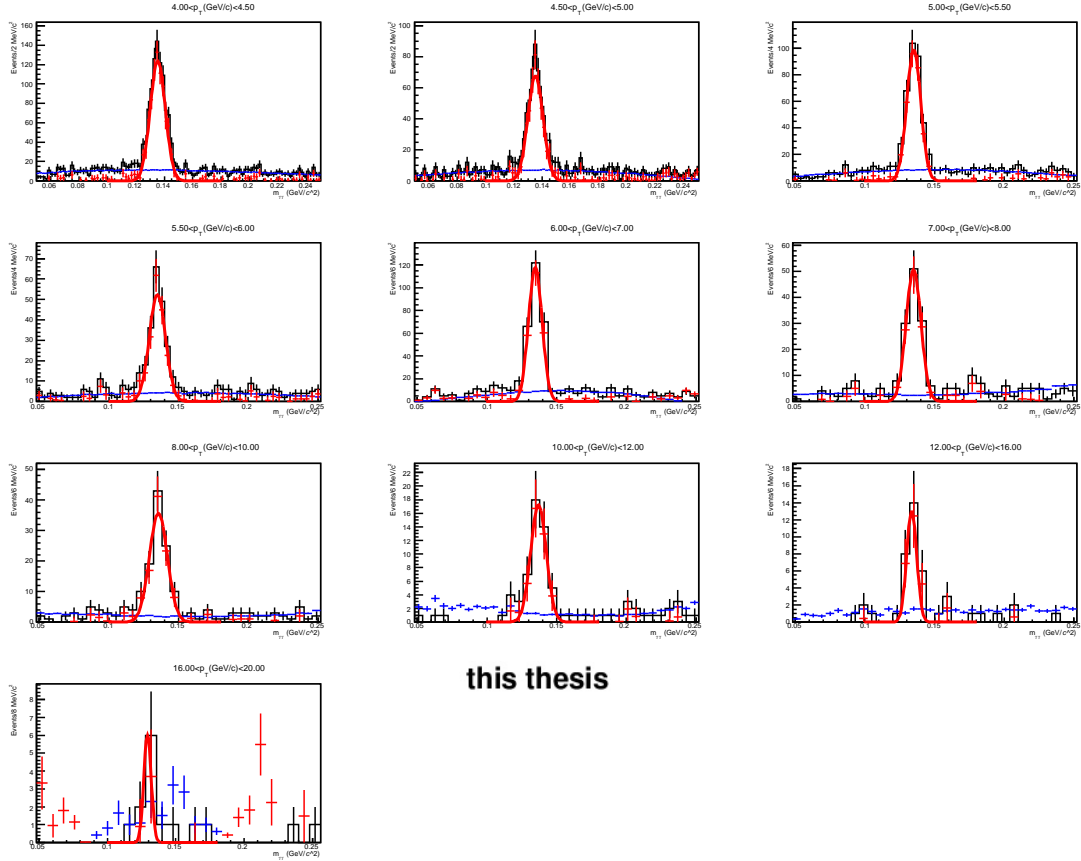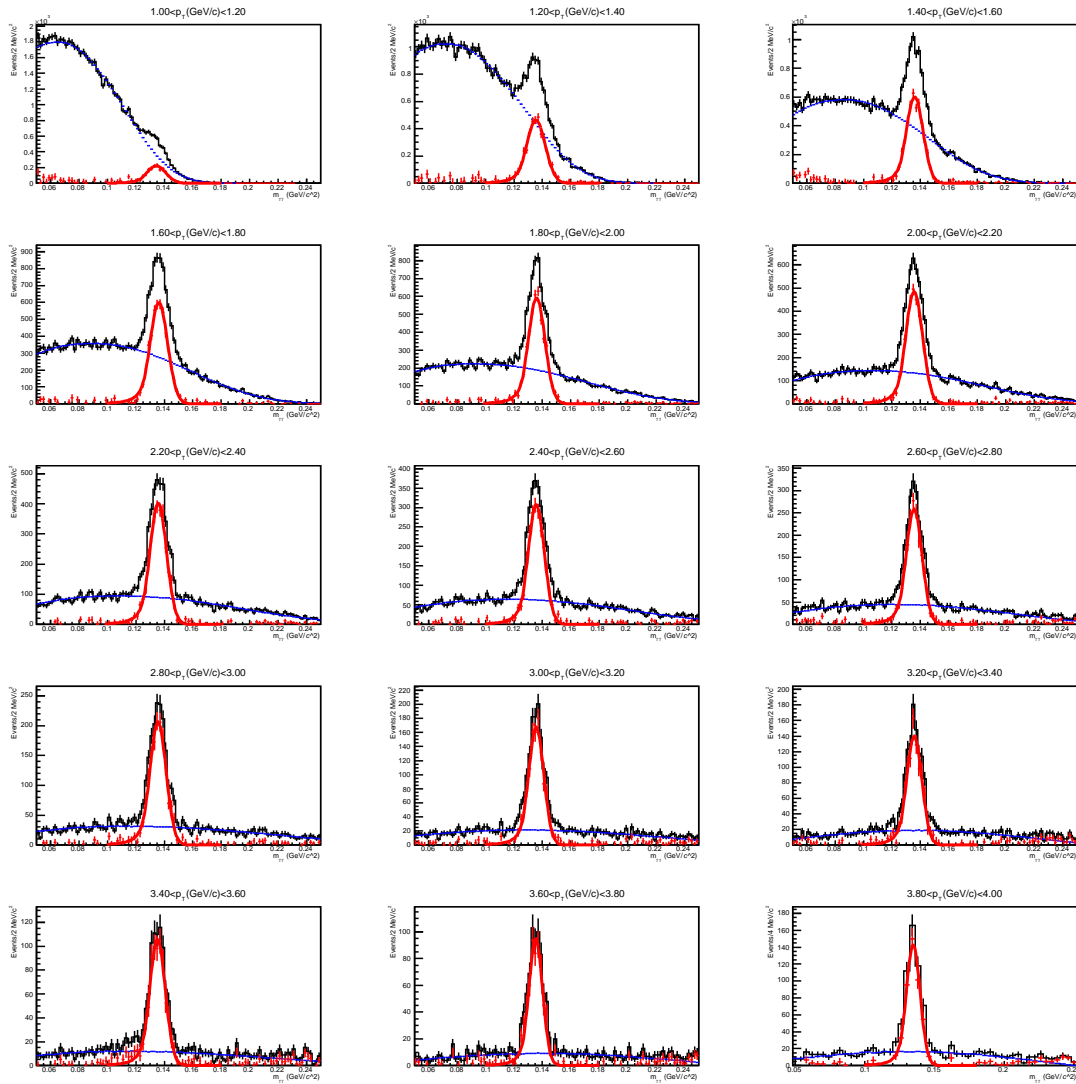= 5.02 TeV
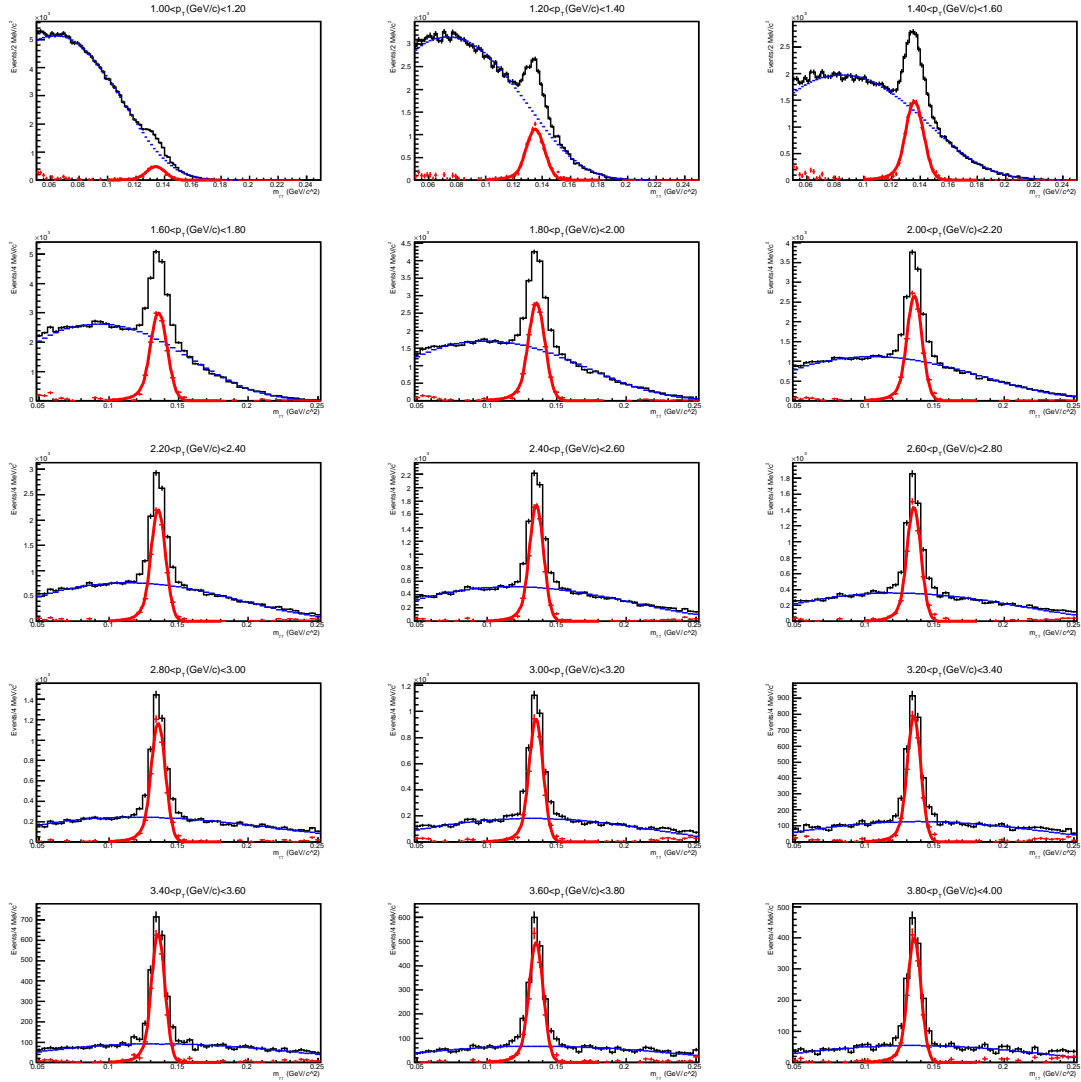
Figure 3: Invariant mass distribution with the Crystal Ball fit in the real data 1
Signal and background(black line), scaled background estimated by event mixing method(blue),
and signal after background subtraction(red) with the Crystal Ball fitting in p-Pb collisions at
$\sqrt{s_{\mathrm{NN}}} = 5.02$ TeV
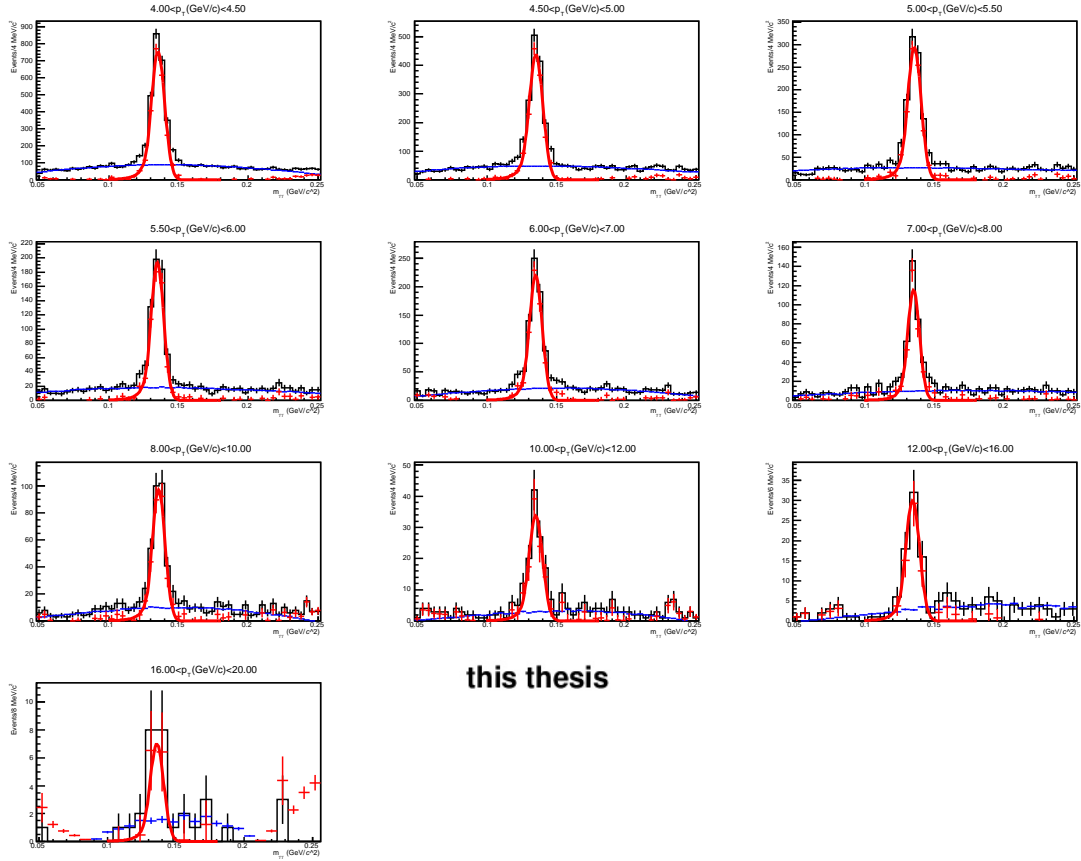
Figure 4: Invariant mass distribution with the Crystal Ball fit in the real data 2
Signal and background(black line), scaled background estimated by event mixing method(blue),
and signal after background subtraction(red) with the Crystal Ball fitting in p-Pb collisions at
$\sqrt{s_{\mathrm{NN}}} = 5.02$ TeV
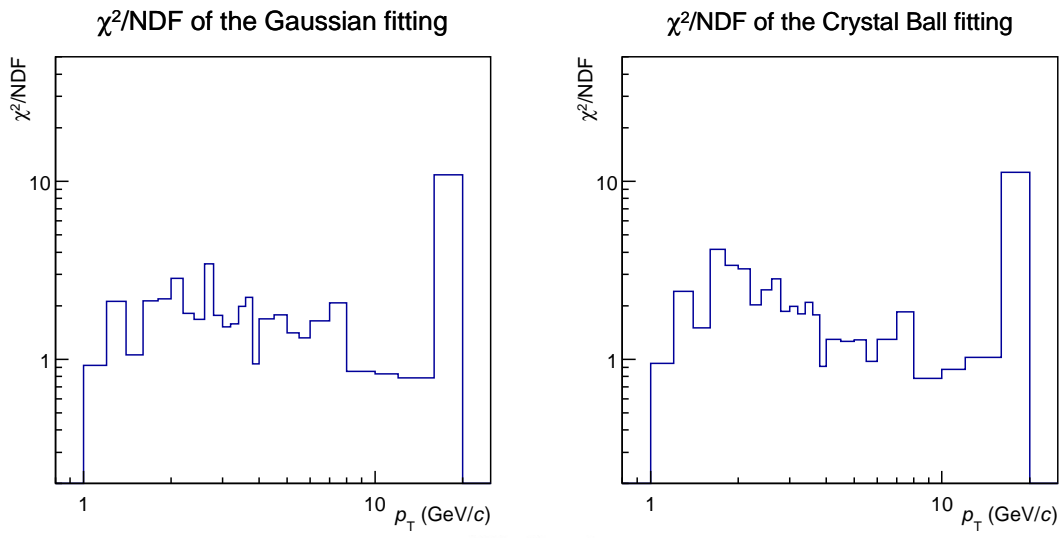
Figure 5: χ^2/NDF of the fitting in the real data
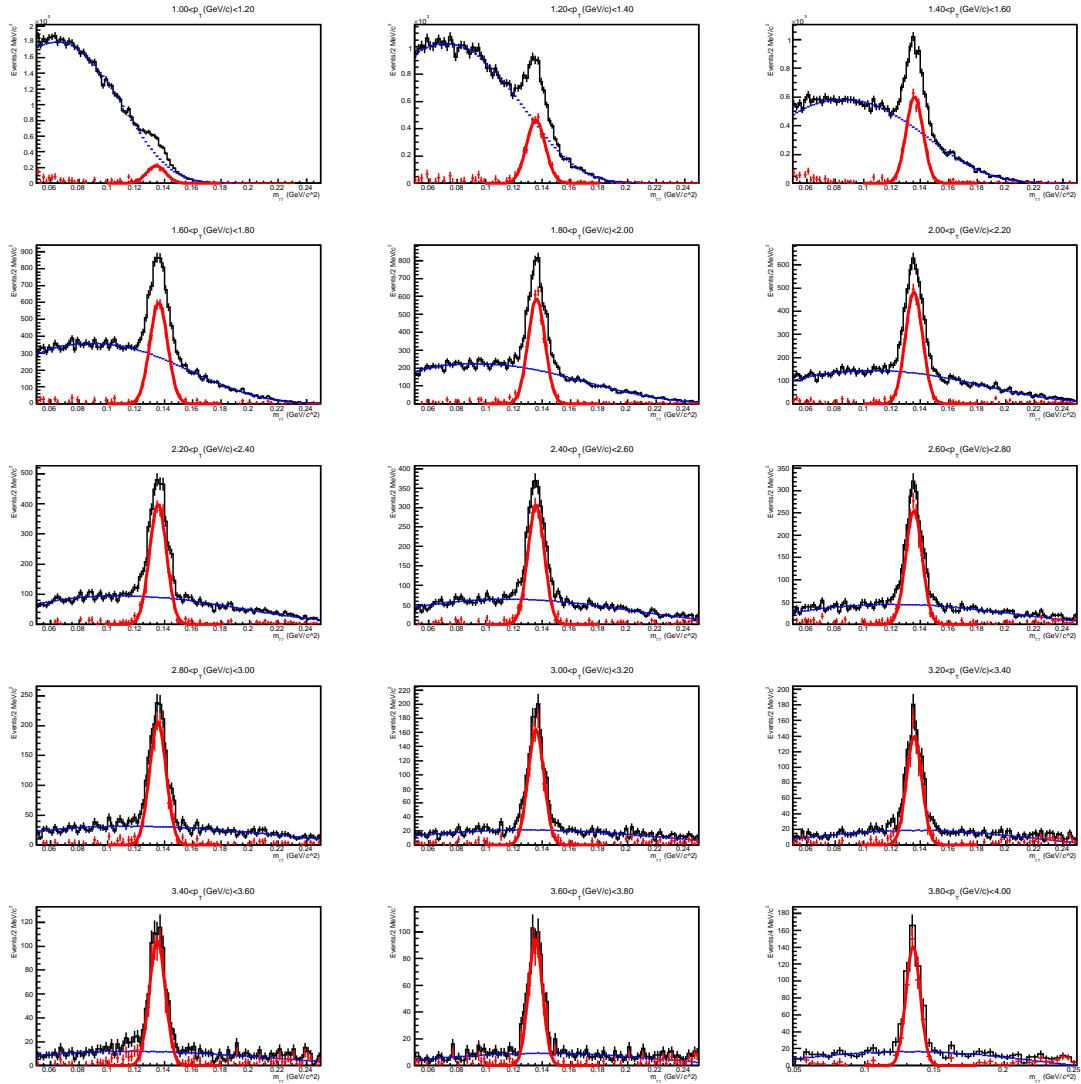
Figure 6: Invariant mass distribution with the Gaussian fit in the DPMJET 1
Signal and background(black line), scaled background estimated by event mixing method(blue),
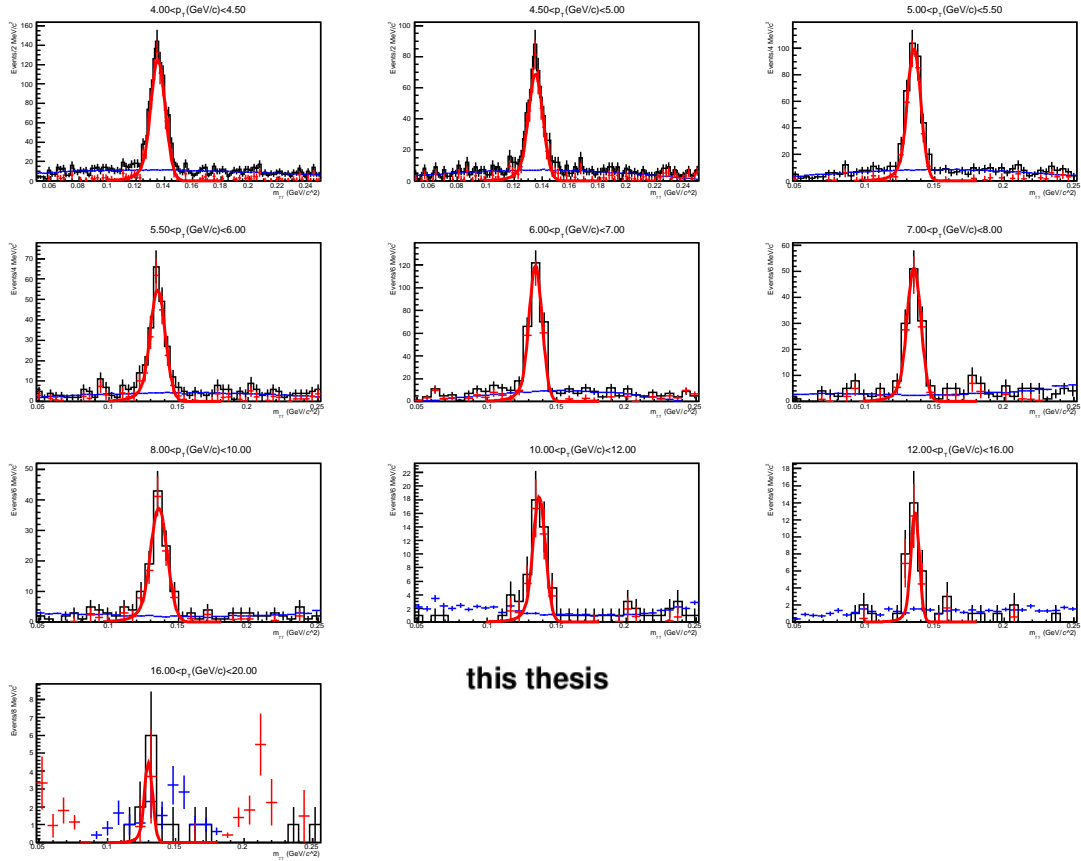and signal after background subtraction(red) with the Gaussian fitting in the DPMJET

108

Figure 7: Invariant mass distribution with the Gaussian fit in the DPMJET 2
Signal and background(black line), scaled background estimated by event mixing method(blue),
and signal after background subtraction(red) with the Gaussian fitting in the DPMJET

Figure 8: Invariant mass distribution with the Crystal Ball fit in the DPMJET 1
Signal and background(black line), scaled background estimated by event mixing method(blue),
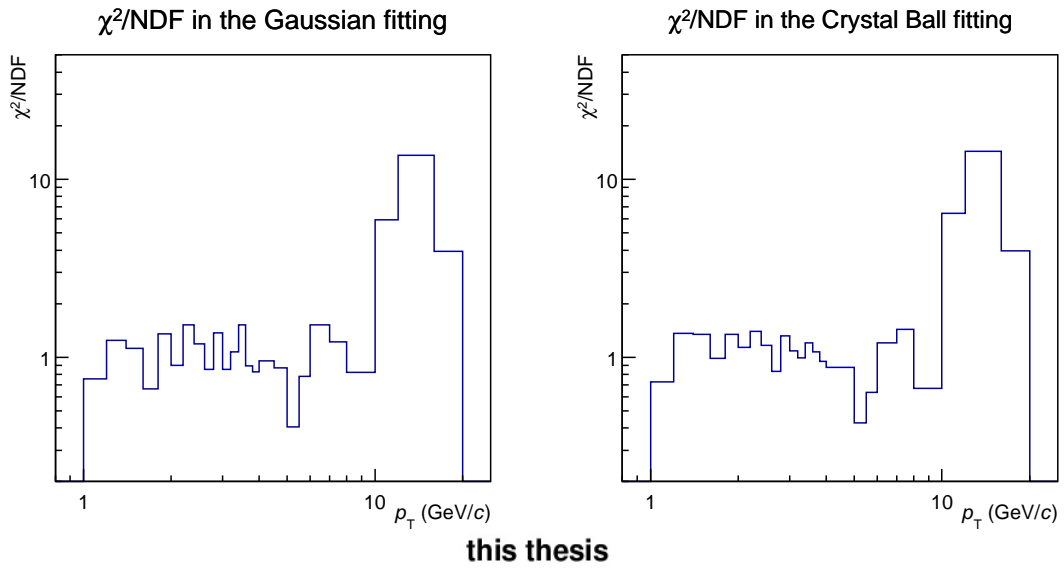and signal after background subtraction(red) with the Crystal Ball fitting in the DPMJET

110

Figure 9: Invariant mass distribution with the Crystal Ball fit in the DPMJET 2
Signal and background(black line), scaled background estimated by event mixing method(blue),
and signal after background subtraction(red) with the Crystal Ball fitting in the DPMJET

Figure 10: χ^2/NDF of the fitting in the DPMJET
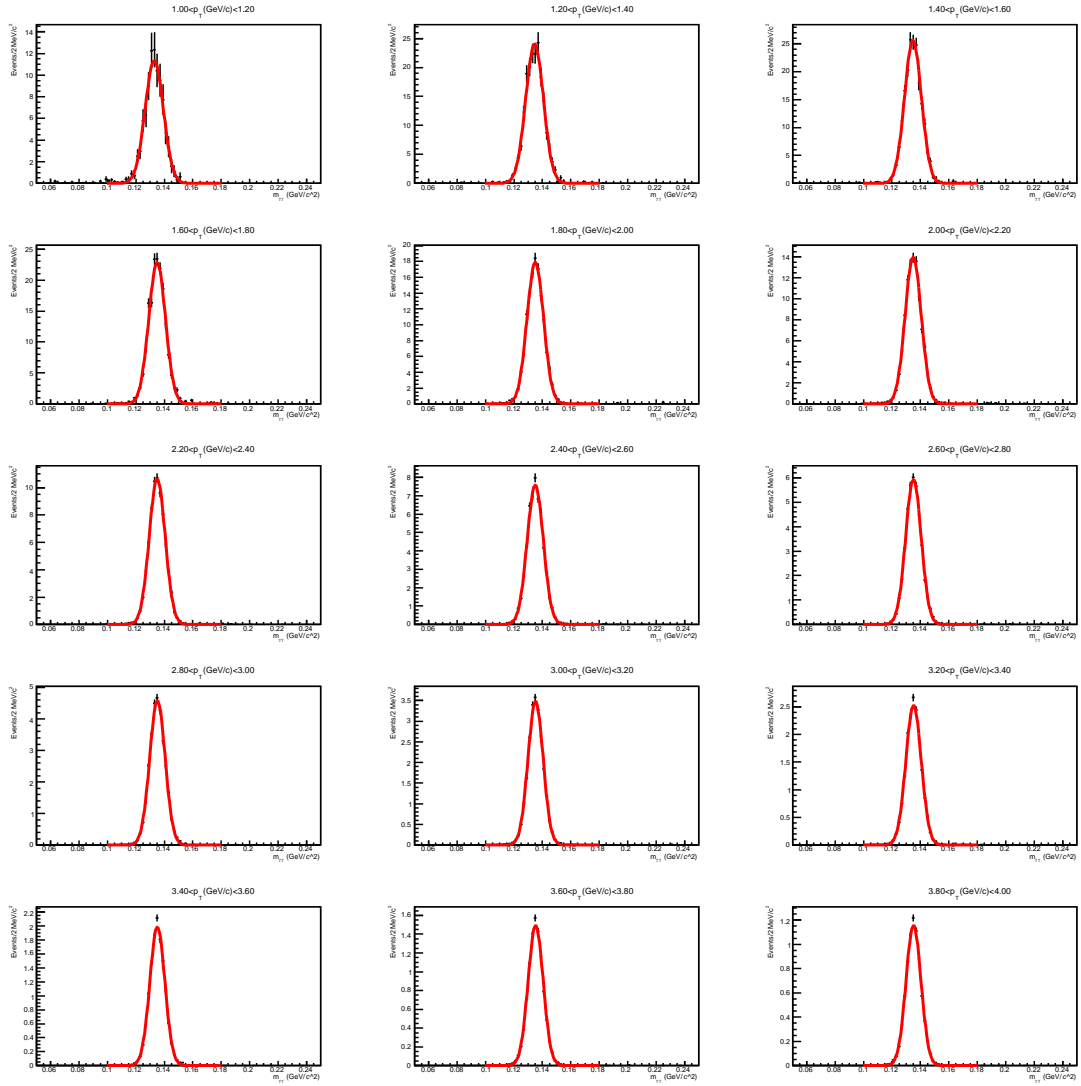
Figure 11: Invariant mass distribution with the Gaussian fit in the added signals 1 Signal(black) with the Gaussian fitting in the added signals
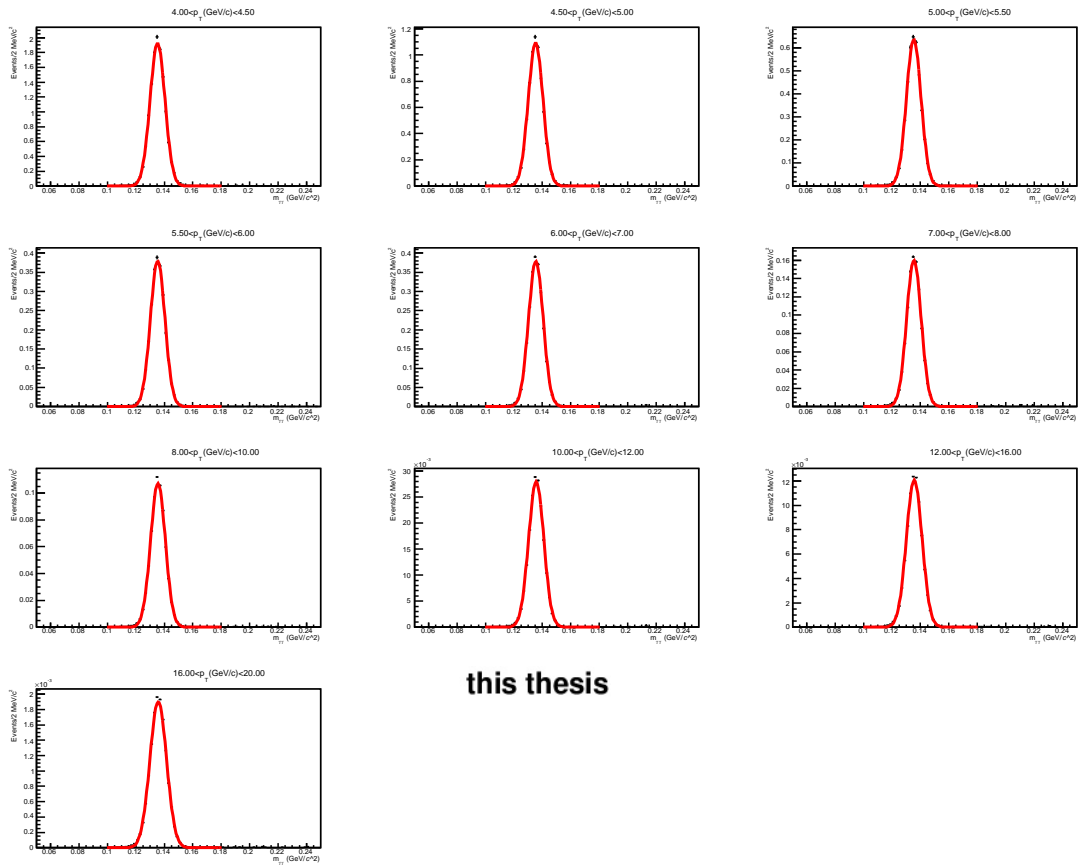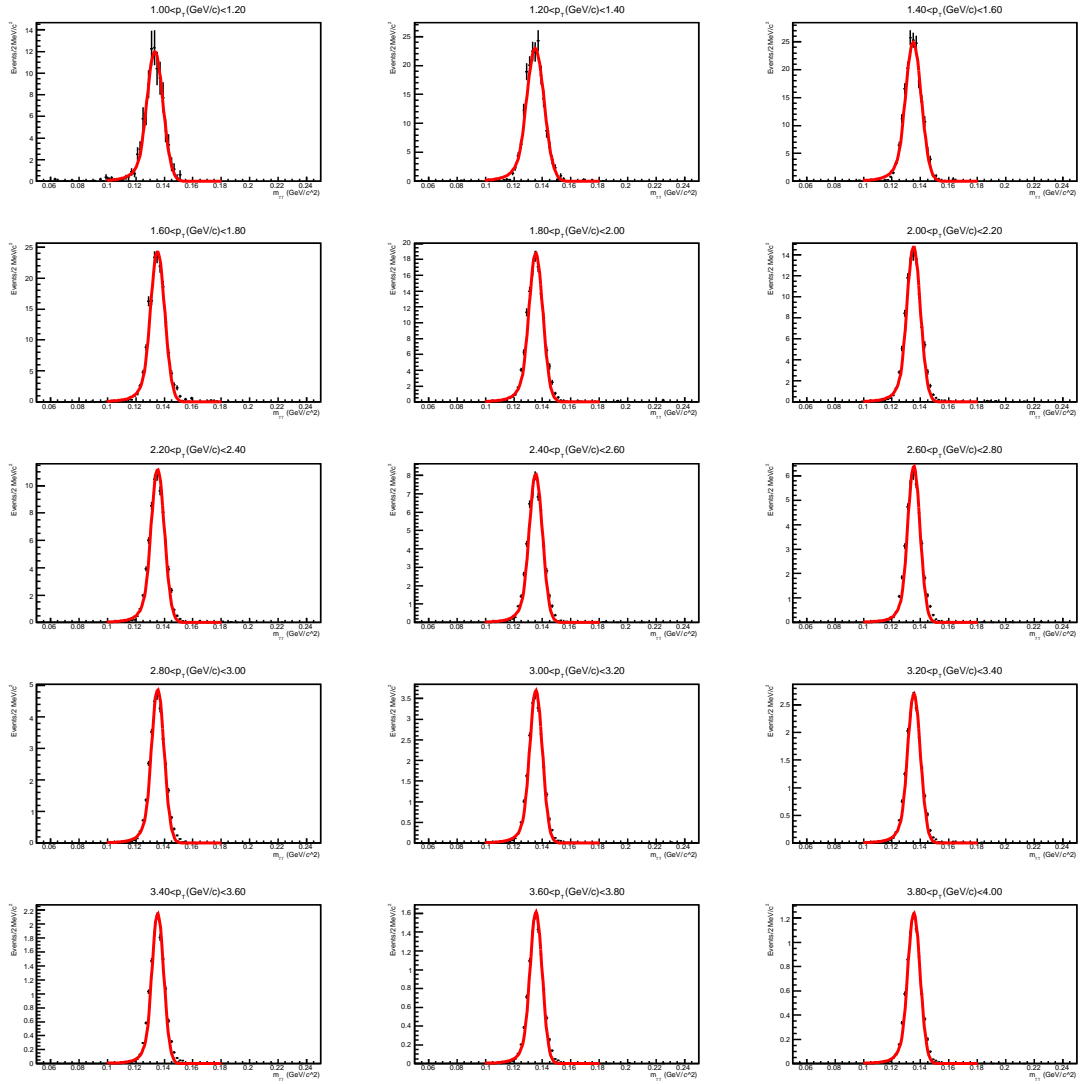
Figure 12: Invariant mass distribution with the Gaussian fit in the added signals 2 Signal(black) with the Gaussian fitting in the added signals

114

Figure 13: Invariant mass distribution with the Crystal Ball fit in the added signals 1 Signal(black) with the Crystal Ball fitting in the added signals
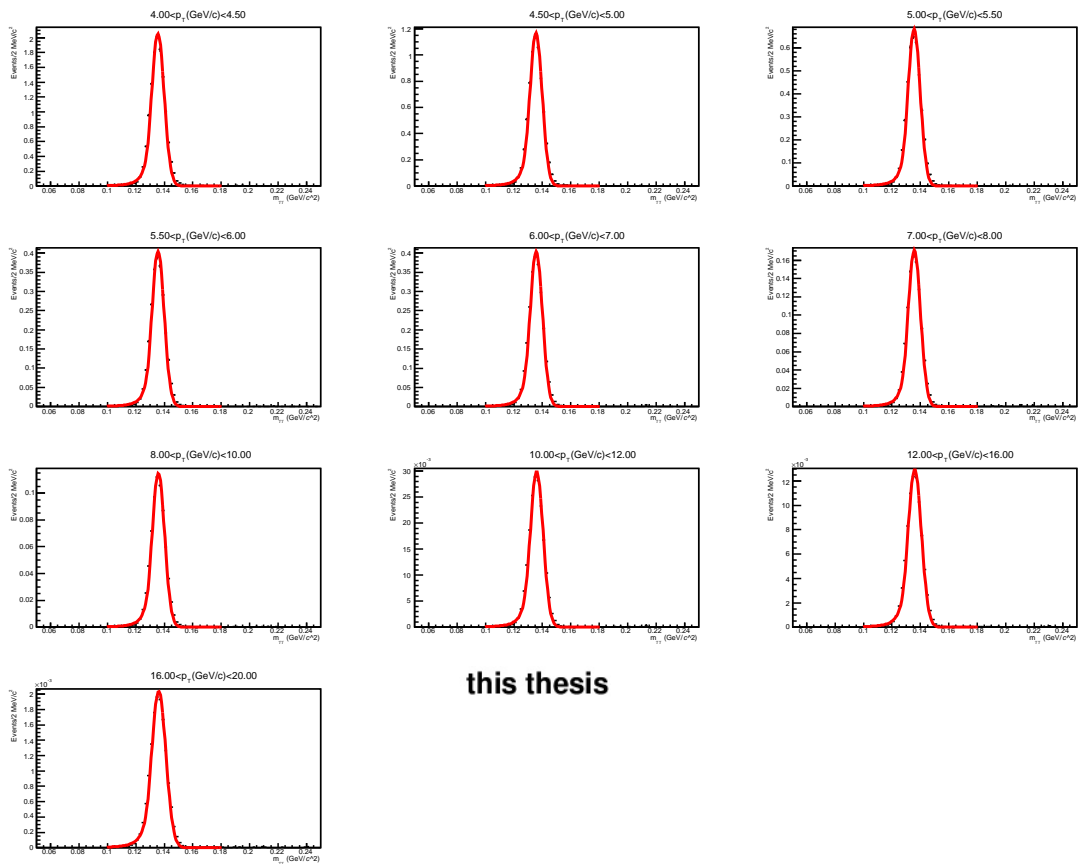
Figure 14: Invariant mass dstribution with the Crystal Ball fit in the added signals 2
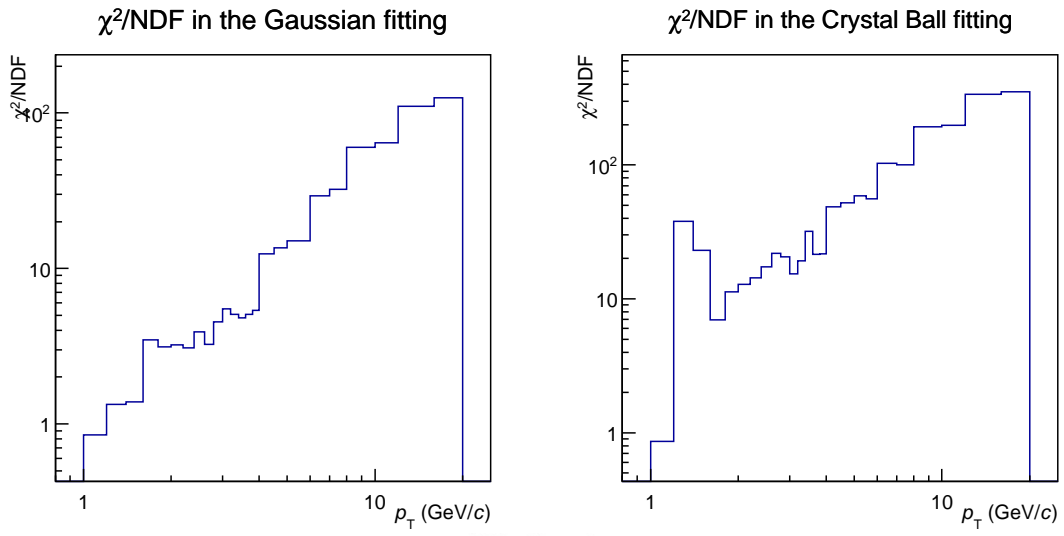Signal(black) with the Crystal Ball fitting in the added signals

Figure 15: χ^2/NDF of the fitting in the added signal

公表論文

(1) Neutral meson production in pp, p-Pb and Pb-Pb collisions with ALICE at the LHC

    Tsubasa Okubo on behalf of the ALICE collaboration

··· Accepted for publication in Nuclear and Particle Physics Proceedings by Elsevier (in press, reviewed)

1/29/17

Certificate for the acceptance of contribution to HP2016 Proceedings

Dear Tsubasa Okubo (Hiroshima University)

We have received and reviewed your manuscript for the proceedings of Hard Probe 2016 international conference: "Neutral meson production in pp, p-Pb and Pb-Pb collisions with ALICE at the LHC". It is accepted for publication in Nuclear and Particle Physics Proceedings by Elsevier.

Sincerely yours,

Xin-Nian Wang
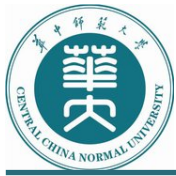
Institute of Particle Physics, Director
Central China Normal University
Wuhan 430079, China
Email: xnwang@mail.ccnu.edu.cn
Tel: +862667867002

参考論文

(1) Direct photon production in Pb-Pb collisions at $\sqrt{s_{\mathrm{NN}}} = 2.76$ TeV

 J. Adam *et al.* ALICE Collaboration

$\cdots$ Physics Letters B 754 (2016) 235-248

(2) Multiplicity dependence of charged pion, kaon, and (anti)proton production at large transverse momentum in p-Pb collisions at $\sqrt{s_{\mathrm{NN}}} = 5.02$ TeV

 J. Adam *et al.* ALICE Collaboration

$\cdots$ Physics Letters B 760 (2016) 720-735